UNIVERSIDADE DE LISBOA
FACULDADE DE CIÊNCIAS
DEPARTAMENTO DE FISICA

Magnetic components and microfluidics optimization on a Lab-on-a-Chip platform

João Ferreira Gil

Mestrado Integrado em Engenharia Biomédica e Biofísica
Perfil em Sinais e Imagens Médicas

Dissertação orientada por:
Dr. Hugo Alexandre Ferreira
Dr. Susana Cardoso de Freitas

2017

Resumo

Desde 1934, quando Moldovan criou o primeiro instrumento que poderia ser descrito como um citómetro de fluxo, este equipamento tornou-se um importante componente em várias especialidades dentro do laboratório clínico para o diagnóstico, prognóstico e monitorização de um número incontável de doenças. Esta tecnologia biofísica suspende entidades biológicas num fluxo de fluido, sinalizando-as usando reconhecimento biomolecular, para depois as detetar através de um aparelho de deteção eletrónica.

Com o crescimento das técnicas de fabricação de semicondutores e microfluídos, foram e continuam a ser feitas muitas tentativas de criar citómetros de fluxo do tipo Lab-on-a-Chip (LOC), o que certamente irá afastar os equipamentos usados hoje me dia nos laboratórios por equipamentos usados *in situ* de custo e tamanho reduzidos, portáteis e sem necessidade de pessoal especializado.

Após uma revisão bibliográfica das técnicas e princípios de funcionamento dos equipamentos já existentes foi possível perceber que a utilização de partículas magnéticas (PM) pode ter várias vantagens quando comparadas com o uso convencional de deteção por fluorescência, removendo assim a necessidade de integrar e alinhar componentes ópticos, permitindo uma medição direta e a construção de um citómetro de fluxo LOC com preparação, separação e deteção de amostras totalmente magnético.

No INESC-MN foi feito um protótipo que permite a deteção de um tipo de PMs em tempo real a velocidades da ordem de cm/s usando sensores magnetoresistivos integrados em canais microfluídicos mas a primeira demonstração desta técnica para aplicações de citómetro foi realizada através da deteção de células Kg1-a marcadas com PMs de 50 nm que passaram, através de um canal microfluídico, sobre 3 sensores magnetoresistivos demonstrando que, para amostras de elevada concentração, pode ter a mesma eficiência que um hemocitómetro, mas com menor erro.

Tendo como ambição um dispositivo LOC capaz de contar várias entidades biológicas na mesma amostra, um módulo de contagem com vários canais paralelos é necessário.

Nesse sentido, foi projetado um novo chip com 4 colunas separadas por 3 mm, cada uma com 7 sensores do tipo válvula de spin (SV) com uma área de deteção de 100x4 μm^2 distanciados 150 μm uns dos outros. Os sensores são abordados individualmente por uma linha de corrente de alumínio de 300 nm e passivados com 300 nm de nitreto de silicio. Alinhados com as colunas de sensores, 4 canais de polydimethylsiloxane (PDMS) com uma secção de 20 μm de altura e 100 μm de largura foram irreversivelmente colados ao chip por ultravioleta-ozono (UVO) criando o canal onde a amostra irá fluir.

Para que as PMs sinalizem a sua passagem é necessário colocá-las sob um campo magnético forte o suficiente para induzir a sua magnetização e para que, consequentemente, as PMs emanem um campo marginal significativo. Aproveitando a insensibilidade das SVs às componentes perpendiculares ao seu plano (xy), aplica-se um campo magnético nesse sentido (z) para magnetizar as partículas.

As PMs ao passarem sobre o sensor geraram um sinal bipolar devido ao campo marginal criado pela sua magnetização perpendicular. Como é apresentado na simulação do sinal, a amplitude do mesmo depende apenas da altura da partícula em relação ao sensor e da magnetização das mesmas, idealmente, uma saturação da magnetização das partículas e o máximo de proximidade aos sensores geraria a maior amplitude possível.

O campo magnético perpendicular foi criado usando um magnete de neodímio posicionado sob a placa de circuito impresso (PCB), onde o chip do citómetro é colado e as ligações entre o chip e a PCB soldadas por ultrassons com fio de alumínio.

Na abordagem usada em Loureiro *et al*., 2011, um magnete de 20 mm x 10 mm x 1 mm foi simplesmente colado sob a PCB, mas devido aos campos magnéticos serem sempre fechados as componentes x e y criam desvios nas curvas de transferência dos sensores deixando apenas 1 ou 2 sensores de uma coluna do chip operacionais. Numa abordagem seguinte foi usado um magnete 20 mm x 20 mm x 3 mm

distanciado 2 cm abaixo da PCB, isto tornou as curvas de transferência dos sensores adequadas para medição, mas fez com que a componente z do campo magnético não fosse grande o suficiente para que as PMs emanassem um campo magnético suficientemente forte.
Percebendo as falhas de cada uma das configurações anteriores, foram feitas simulações do campo magnético que iria influenciar o chip originado por magnetes de vários tamanhos a várias distancias para perceber qual conseguiria fornecer uma maior área em que as componentes x e y fossem menores que 10 Oe e em que a componente z fosse de pelo menos 1 kOe. Através das simulações foi concluído que o magnete de 20 mm x 10 mm x 1 mm o mais próximo possível do chip seria a melhor solução, mas que um alinhamento preciso seria necessário.
Para esse fim, foi fabricado numa fresadora um sistema de alinhamento em PMMA. Para que o alinhamento fosse o correto foram feitos 4 furos de alinhamento no sistema de PMMA e na PCB e para reduzir a distancia ao máximo foi feita uma bolsa na PCB da mesma área que o chip deixando a distancia do magnete aos sensores de 1 mm (0.3 mm de PCB + 0.7 mm de substrato de silício). Com isto, o alinhamento em x foi conseguido, mas para alinhar em y foi criado um trilho no sistema de PMMA onde o magnete pudesse deslizar, controlando-o pela rotação de um parafuso com passo de 0.5 mm.
Para colocar o magnete na posição ideal, foi medida consecutivamente a curva de transferência do 4º sensor de uma das colunas, num campo magnético de -141 Oe a 141 Oe, até que este tivesse um campo de acoplamento efectivo (Hf) de aproximadamente 0 Oe, o que significa que a curva de transferência estaria perfeitamente centrada em zero e criaria um sinal bipolar perfeito.
Após o alinhamento e posicionamento do magnete, todos os sensores foram caracterizados e, nesses resultados, podemos ver perfeitamente o efeito das componentes x e y do magnete. Com o lado longo do magnete paralelo ao lado longo das SVs e alinhado de forma que o Hf fosse o mais próximo de 0 Oe no 4º sensor de uma coluna, percebemos que a componente x (lado longo) do campo magnético criado pelo magnete tem efeitos na sensibilidade dos sensores fazendo com que esta caia à medida que nos afastamos do centro do magnete. Enquanto que a componente y tem efeitos sobre o Hf dos sensores tornando-o mais positivo à medida que medimos a 3ª, 2ª e 1ª linha de sensores e tornando-o mais negativo quando medimos a 5ª, 6ª e 7ª linha.
São também apresentadas simulações dos canais microfluídicos para perceber como a velocidade das partículas afeta o sinal e qual a velocidade máxima permitida para que placa de aquisição eletrónica seja capaz de o detetar.
Com estas conclusões, um novo chip foi desenhado e fabricado. Neste novo chip a distância entre as colunas de SVs foi reduzida para apenas 1 mm, o que obrigou também à alteração dos canais microfluídicos, ao tamanho do chip e da estrutura de PDMS. Também são apresentadas simulações que mostram que se um segundo magnete, alinhado com o primeiro, for colocado sobre os canais microfluídicos poderá melhorar a magnetização e a homogeneidade do campo, o que permitirá que os 4 canais tenham a mesma sensibilidade e um desvio padrão de Hf menor.
Todos os antecedentes teóricos, os métodos de microfabricação e técnicas de caracterização usados são apresentados e descritos.

Palavras-chave: citómetro, lab-on-chip, partículas magnéticas, sensores magnetoresistivos, microfluídica.

Abstract

The diagnosis, prognosis and monitoring of diseases serves for the only purpose of preserving and improving life. Being this the greatest objective of the human kind, since ever that efforts have been made to better our ways to do that.
One of those, a very important component in several specialties within the clinical laboratory is the flow cytometer, a biophysical technology which uses biomolecular recognition to sort and count biological entities by suspending them in a stream of fluid and detecting them through an electronic detection apparatus.
The improvement of the semiconductor and microfluidic fabrication techniques have created the chance to bring the expensive, specialized and bulky equipment out of the laboratories and generate new machines able of having the same efficiency but with smaller price, size, allowing portability and removing the need for specialized personnel. This is the concept behind the next generation of in point-of-care apparatus, the La-on-a-Chip (LOC).
At INESC-MN it is understood the potential that magnetic particles (MP) have in a LOC flow cytometer and as such a real-time detection of single magnetic particles magnetoresistive based cytometer was prototyped. Demonstration of this technique for cytometer applications was accomplished by indicating that for high concentration samples it can have the same efficiency as the hemocytometer method but with lesser error.
This thesis has as objective the optimization of the magnetic and microfluidic components of a LOC to allow the parallelization of measurements and enabling the real-time measurement of different particles at the same time.
For this purpose, a bibliographic review of the theoretical backgrounds, of the fabrication and characterization techniques, of the different detecting principles and of the already existing magnetoresistive counting modules was made to get a deeper understanding of the optimization possibilities.
The present work describes the above-mentioned platform for dynamic detection of magnetic labels with a magnetoresistive based flow cytometer, where a permanent magnet is used to magnetize the labels enabling them to trigger the sensor.
Several simulations of the magnetic fields created by the permanent magnet and the microfluidic channels were done and analyzed in order to characterize the MPs signal, understand which would be the best positioning of these components and which fluid velocities would be in the range of the electronic read-out capabilities.
This study led to the fabrication of a micromachined polymethylmethacrylate (PMMA) alignment system to correctly position the permanent magnet under the cytometer's chip. This made the control over the magnet's positioning more sensible and thus reducing the influence of its unwanted magnetic components on the chip. The approximation of the magnet to the chip enhanced the signal by optimizing the MPs magnetization and consequently the signal amplitude, the precise alignment corrected the sensors response by improving its sensitivity and removing them from saturation states. Through this new setup all the sensors in the chip became operational.
Finally, using the several techniques of microfabrication also describe in this thesis, a new chip was designed and fabricated to improve even more the sensors sensitivity and consequently augment the number of the cytometer's counting channels.

Key-words: cytometer, lab-on-chip, magnetic particles, magnetoresistive sensors, microfluidics.

Index

List of figures

List of tables

List of acronyms

µTAS - Micro Total Analysis System
AC – Alternated Current
ADC – Analog-to-Digital Converter
AFM - Antiferromagnetic
CAD - Computer-Aided Design
CIP – Current-in-Plane
CVD - Chemical Vapor Deposition
DC – Direct Current
DNA – Deoxyribonucleic acid
DWL - Direct-Write Laser
FM - Ferromagnetic
GMR – Giant Magnetoresistance
GPIB - General Purpose Interface Bus
GUI – Graphic User Interface
Hf - Effective Coupling Field
HIV - Human Immunodeficiency Virus
HMDS - Hexamethyldisilane
IBD – Ion Beam Deposition
IC - Integrated Circuit
INESC-ID - Instituto de Engenharia de Sistemas e Computadores – Investigação e Desenvolvimento
INESC-MN - Instituto de Engenharia de Sistemas e Computadores – Micro e Nanotecnologias
INL - Iberian Nanotechnology Laboratory
LOC – Lab-On-a-Chip
MEMS – Microelectromechanical Systems
MP – Magnetic Particles
MR - Magnetoresistance
MRAM – Magnetic random-access memory
MRI – Magnetic Resonance Imaging
NIR – Near-infrared
PCB - Printed Circuit Board
PDMS - Polydimethylsiloxane
PECVD - Plasma-Enhanced Chemical Vapor Deposition
PM – Permanent Magnet
PMMA – Polymethylmethacrylate
POC – Point-of-Care
PR - Photoresist
PVD – Physical Vapor Deposition
Re – Reynolds number
RF – Radio Frequency
RIE - Reactive Ion Etching
SV – Spin-Valve
SVG – Silicon Valley Group
USB – Universal Serial Bus
UVO – Ultraviolet-Ozone
VSM – Vibrating Sample Magnetometer

1 - Introduction

The world is in permanent changing, and the world in which we live now is completely different to the one our previous generations lived in. Every passing year the communications, transportation, healthcare, education and other types of needs are satisfied with increasingly more complex systems and paradoxically become of easier access to the overall population.
With the continuous technological evolution and the social context influenced by it, this trend has been and will continue to be even more accentuated.
The world has faced a technological revolution and with it the time where dreams are thought, designed and built instead of simply dreamed, where everything is possible.
This exponential technology growth has begun with the invention of the transistor in 1947 when William Shockley, John Bardeen and Walter Houser built the first working semiconductor amplifier. This new and revolutionary electronic component came as the replacement of the mechanical relays and thermionic valves with reduced size, power and fabrication costs.
Even though all the possibilities that the transistor brought, only in 1958, when Jack Kilby constructed the first integrated circuit (IC), the scientific community realized the full potential of the transistor and his integration with passive components in small thin films.
Being aware of the evolution of the semiconductor technology and fabrication techniques, in 1965, Gordon Moore predict that the number of transistors in a chip would duplicate every 2 years without increase in the price. Nobody could have guessed that this fact would be a reality until nowadays and that this reality would originate improvements in so many areas of knowledge and participate in the creation of new ones.
The rapid appearance of smaller, more powerful and cheaper transistors and IC made computers and phones an indispensable need to the population of the developed countries. This technology globalization transformed human life and its standards of cleanliness, medical care, transportation and entertainment, making the notion of progress closely related to technological development. This information era created by the computers and the internet allowed the sharing and dissemination of worldwide research and the consequent creation of new knowledge.
Being life the human most precious possession, maintenance of health and illness prevention were also great fields of research and development. The healthcare technologies, not at the same rate but, accompanied the evolution of the semiconductor industries being able of create new techniques and equipment for measuring, characterizing and imaging biological systems.
However, life sciences have also taken advantage of the existing amazing computational power and are trying to understand life from the bottom-up by using and creating new and more complex algorithms to run through gigantic DNA and proteins sequences databases. This necessity for storing and the ability for crossing and comparing large arrays of information is the field of bioinformatics. The characterization of the complete genome of a wide variety of species, the form, structure and sequence of amino acids of more than 500.000 manually annotated protein sequences have been helping researchers to understand the signal transduction and metabolic pathways of life.
The new knowledge created using informatics and biology together showed a great potential, opening way for analog sciences. The cheminformatics is also an informatics aided science that as bioinformatics, stores and cross references between chemical components.
This fast spreading of information and this capability of studying the basic elements of each area of knowledge joined with the transistor induced miniaturization trend created the will and capability to develop new machines with the same and new functions of the already existing ones but reducing their size, response time, user friendliness, pre-analysis steps and fabrication costs. And just like the physicist Richard Feynman predicted in the 1959 lecture, “There’s Plenty of Room at the Bottom”, the time has

come where atomic manipulation is already a reality, the point where biology, chemistry, and physics joint together, the nanotechnology.

One of its many propulsors in the health applied nanotechnology came before nanotechnology even being thought when in the 1953 Leland C. Clark invented the very first biosensor, the Clark electrode [1]. Based on his research he later realized that the electrochemical detection of oxygen could be used for a broad range of bioanalytical tools, by incorporation of immobilized specific enzymes. And with this the first concept of a biosensor as emerged making him the "father of biosensors".

Biosensors are used to detect a specific interaction between two biological entities with affinity to each other, by other words, measure intermolecular forces like Van der Waals forces, salt bridges and hydrogen bonds between two attracted molecular species. This phenomenon is called biomolecular recognition and its detection is the base principle in DNA hybridization, antibody-antigen and ligand-receptor based systems.

These systems are the basis of applications such as genetic disease diagnostic, mutation detection, gene expression quantification, microorganism detection and biological warfare agent detection. Biosensors are composed by a biological-sensing system (bioreceptor), a transducer and an output system. The bioreceptor is a biological probe molecule who as the affinity to the specific target analyte.

Nowadays the field of biosensors has two broad types of equipment, in one side there are the sophisticated, high-throughput laboratory machines capable of rapid, accurate and convenient measurement of complex biological interactions and components and in the other the easy-to-use, portable devices for use by non-specialists for decentralized, in situ or home analysis. While the former may still have better results and well-established measure protocols they are expensive, bulky and their cost restricts the access of the poor population, the latter are being improved and can be mass produced, inexpensive and cut the need for specialized personnel.

The continuous understanding of materials and their physics at the nanoscale, the ability to predict and design the biological binding entity, the fast development of the semiconductor industry and the emerging microfluidic technologies brought the ability to reduce to chip size a series of complex laboratory tasks and to integrate various laboratory processes in a single compact device, the lab on a chip (LOC) devices.

These types of devices are being developed to transform the bulky laboratory machines referred above into the cheaper, portable and easy-to-use ones.

Integrated microsystems offer the potential to significantly improve the throughput, sensitivity, accuracy and affordability of biochemical analysis. The potential to increase the processing power while reducing the economic cost and environmental impact has created a growing interest in the development of miniaturized devices. Furthermore, the reduced size of the LOC components hold several advantages in the diagnostics field due to the consumption of low volumes of fluids, which means less waste, which traduces in less reagents cost and less samples volumes. In addition, the reduced sizes make possible to reduce analysis and response times due to short diffusion distances which also guarantee a better control over the process. All these features allow the production of compact systems with different integrated functionalities that use small fluid volumes and needs less stored energy which make them a safer platform able for mass production at low fabrication costs [2].

So far, it is a standard procedure to collect the samples on site and send them to specialized laboratories for analysis, which is usually costly and time consuming, since the required instrumentation is large and expensive and calls for qualified personnel to carry out and evaluate the outcome of the multiple steps involved in the analysis. From an originally unprocessed specimen, for example a blood sample, these steps typically include separation and amplification as well as chemical modification and detection of the molecules in question. The possibility of performing fast and in situ analysis, together with early stage diagnostic, represents one of the major goals in the medicine.

LOC devices can be integrated with biosensors, offering a much-needed alternative to the still used traditional methods, allowing rapid real-time and multiple analytes detection. This alternative designed to be used at or near the site where the patient is located with no need for specialized personnel or a dedicated space are called point-of-care (POC) tests and are an advantage that can be used for whole blood analysis, glucose testing, HIV testing at a small village medical center and several other analyses like blood gas and electrolyte testing that may be needed in case of an accident to have a preliminary diagnosis at the site. The continuous development of smaller and cheaper POC devices is of the utmost importance for the underdeveloped countries since the budget available to spend on medical diagnostics is limited compared to that of the developed countries. Also, the clinical needs of the developed countries are different from the underdeveloped ones since, the first fights mostly against noncommunicable diseases like cardiovascular diseases, cancer and neuropsychiatric disorders while the second could beneficiate greatly from the diagnosis of infectious diseases as HIV, tuberculosis and malaria since after identified they can be treated and prevented [3].

POC tests based on LOC technologies have the potential for rapid and portable diagnosis and the consequent saving of lives.

The flow cytometer is an equipment with the ability to diagnose all the diseases mentioned above and thus we can understand a fundamental tool in clinical laboratories.

A flow cytometer is an instrument designed to detect and enumerate cellular elements in a suspension. The specific attributes of this technology allow measuring morphologic, biochemical and functional characteristics of microscopic particles suspended in a stream of fluid.

The conventional flow cytometry is made by staining the target analyte with fluorophores and focus a stream of fluid through a narrow path making the particles pass one by one and exciting them with a laser beam or an arc lamp. The excited fluorophores will send photons to the detectors and give them the information needed to characterize and quantify the target particles, depending on their ability to scatter incident laser light as well as by emission of fluorescent light by the fluorophores.

To accomplish this, flow cytometers employ the coordinated use of 3 components: the fluidics, optical, and electronic systems.

The fluidics system generates a pressurized sheath fluid that carries the particles in the sample through the fluidic channel. By hydrodynamic focusing the particles are maintained in a single line and are obliged to pass one by one through the light excitation point in a precise and rapid way. The hydrodynamic focusing is made by introducing the sheath fluid at a higher velocity than the sample focusing it to the central region of the channel. A uniform stream of particles is essential to ensure reproducible illumination of the cells as they intersect the laser beams of the instrument.

For optical excitation, conventional flow cytometers use 1 or 2 lasers at different wavelengths and as the particles flow through the fluidic channel they intersect the laser, scattering the light that will be collected along the laser beam, forward scatter, and at a 90º angle to the beam, side scatter. Each particle scatters the laser beam and the fluorescent chemicals staining it may be excited into emitting light at a longer wavelength than the light source. Before getting to the

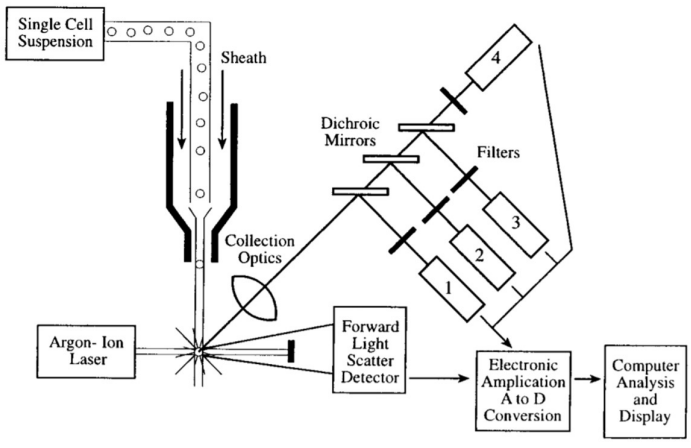

Figure 1.1 - Schematic of a conventional flow cytometer [5].

detectors the scattered light passes through a set of filters and mirrors to define the specific fluorescence wavelength.

After the filters, the forward scattered light is collected by a photodiode and the side scattered one is collected by a photomultiplier tube also in the side scattered direction there are typically 4 or 5 photomultipliers for the fluorescent emissions [4-5]. When the photons are collected by the photomultipliers, they generate an electrical signal that is logarithmically amplified and then sent to the flow cytometer's computer for storage and analysis (figure 1.1).

The intensity of the light emitted is directly proportional to the amount of marker on the surface of the particle [4].

Since 1934, when Moldovan created the first instrument that could be described as a flow cytometer, this equipment has become an important component in several specialties within the clinical laboratory for the diagnosis, prognosis and monitoring of an unfindable number of diseases. The characterization of pathogenic mechanisms of disease continues to enlarge this number which means the continually expanding range of applications. But the still used flow cytometers are bulky and expensive instruments that have high costs and need for specialized personnel [6]. These facts, join with the accessibility of microfabrication technologies, made the need to create smaller, cheaper and POC flow cytometers.

Through the use of microfabrication techniques some POC cytometers have already reached the market, as is the case of the Agilent 2100 Bioanalyzer (Agilent Technologies, Inc., Santa Clara, CA USA), an instrument that can receive different microfluidic chips to perform several routine diagnostics, one of them a flow cytometer chip [7]. Also, the Fishman-R (On-Chip Biotechnologies Co. Ltd., Tokyo, Japan) is a newer equipment that has 4 detection channels, more 2 than the previous one [8].

But the search for further reduction of cost, size and complexity of flow cytometers, and the increasing need for high throughput analysis continues to provide challenges in this field of research and with them new techniques are emerging.

The creation of a micro total analysis system (μTAS) needs the integration of several different modules for it to be used as a POC device. There are already many developed sample preparation microdevices where extraction, purification, concentration and dilution modules have different functioning principles and fabrication techniques. Different sample handling techniques are also available like micromixers, chambers, valves and micropumps that are able of precise manipulation of small sample volumes that are good mechanical alternatives to electroosmotic flow [9]. But before this modules integration with the separation and the counting modules they all should be optimized separately.

Innumerous fluorescent counting microchips have been fabricated and commercialized, but the search for the optimal microflow cytometer continues [9,10].

The characteristics that can be optimized in a microfluidic chip depend on the sensors functioning principle and the analyte to be measured. Accounting with the material that can be used and the designs that can be made, the possibilities are endless. In a fluorescent based counting microchip, we always have one optical component with light sources, photodetectors, lenses, filters, mirrors and beam splitters and a microfluidic component for sample flow focusing. Zhao and You [11] created an optimized microflow cytometer by using binary optical elements to create homogenized well shaped 50x10 μm^2 rectangular quasi-flat-top spots finding a way to have the same intensity of light in all the sample incident light and thus removing any artifacts created by the typical Gaussian laser profile and also added a 3D hydrodynamic focusing made from 5 glass plates where different level microchannel where carved. By using two syringe pumps, one for the sample and other for the sheath fluid, they made one zone of horizontal focusing and ahead a vertical focusing, being able of create a sample flow diameter, 15 μm, in the same order of magnitude of their pixel size, 6.5 μm, having comparable or even better results than the commercially available flow cytometers.

New fluorescence methods have been optimized not only by improving the conventional method but also by augmenting the throughput by doing several parallel channels [12] and time encoded methods

[13]. Also, even though in an early stage, the use of quantum dots embedded in microbeads that can respond differently at the same wavelength just by changing the intensity has been studied for use in micro flow cytometers [14].

In fluorescence methods, the optimization process of an equipment can be done not only by changing the design but also by improving his data processing computation method, like Lin and Lin [15] did by using a UV-Vis-NIR spectrometer and a simple superposition scheme to extract the absorption, fluorescence, and side-scatter information. With this, their computation method proved to be able to discriminate both micro-particles with 4 different fluorescence labels and 2 different stained cells, characterizing their sizes at the same time and all of this within the same microchannel.

Another detection method used in the development of new micro flow cytometer is the impedance method where the intrinsic properties of the particles/cells are used as a label. In this method, the particles flow through the channel that has at least one pair of planar electrodes positioned in the channel walls, these electrodes are then fed with an AC current and as the particles pass between the electrodes the change in the current profile that flows between the electrodes is measured and analyzed to retrieve the information of the size and the dielectric properties of the particle (figure 1.2). As all detection methods, microfluidic impedance flow cytometry has its drawbacks, like the lack of close contact between cells and electrodes when the cells are continuously flushed to flow through the detection area between two electrodes leading to current leakages by travelling through solutions surrounding the cells, also the relative positions of travelling single cells between two facing electrodes can also lead to issues of low detection stability and repeatability [16].

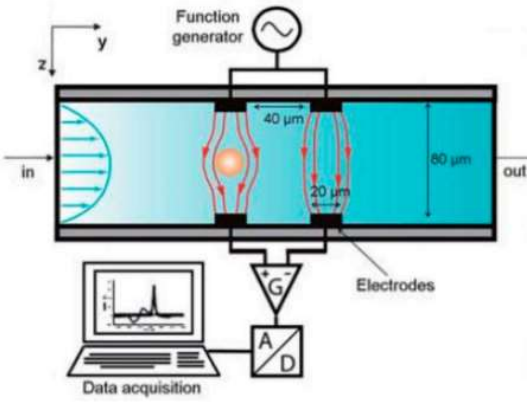

Figure 1.2 - Schematic of an impedance based flow cytometer [16].

But the microflow cytometry had a brand-new way to flourish when the first magnetic bead-based bioassay was suggested by Kriz et al. in 1996 [17], in which an inductive coil was used to measure the change in magnetic permeability of a gel due to specific binding of functionalized beads. In contrast, Baselt et al. [18] suggested in the same year that specific binding of beads could be detected by the deflection of piezoresistive cantilevers in a magnetic field, and by magnetic microsensors in 1998 [19, 20].

Since these proposals, magnetic particles together with magnetic microsensors have become a promising tool for nearly all major LOC applications, from sample capturing, purification, enrichment, transport to detection. The integration of sample preparation modules [21] and sorting modules [22] based on magnetic particles with fluorescence based detection modules has been widely used.

Understanding the advantages in magnetic biosensing several groups started exploring Baselt's idea. One of them is INESC-MN that using the several years of experience and knowledge in solid state technologies, like MRAMS and magnetic read heads, started in 2000 to pursue their POC magnetic detection platform for biosensing, an already commercially available (https://www.magnomics.pt/) technology able to replace a standard benchtop biosensing apparatus and capable of femtomolar limit of detection [23].

Even though the fluorescence flow cytometry is already well established, the lack of need to integrate and align optical components, the possibility of direct electronic readout and the option to perform sample preparation, separation, focusing and detection only by magnetism made INESC-MN start the research to construct a LOC magnetic microflow cytometer.

Contrarily to their first magnetic biosensing platform, where they use a micro array to immobilize the target sample, this new platform uses a dynamic detection method where the magnetic labels linked to the specific target sample are forced to flow inside microchannels that cross over MR sensors signaling their passage. This way there's no need for washing steps, which removes detection errors. Also, as the MR sensors are micro fabricated there is no need for placement and alignment of sensors like in the fluorescence detection.

To be able of performing this dynamic magnetic detection method a static magnetic field is used to magnetize cells labeled with superparamagnetic beads. The magnetic field needs to be applied perpendicularly to the sensor's plane in order not to affect the sensor response which is only sensible to in plane magnetic components (figure 1.3 (left)). By applying a perpendicular magnetic field to the particle or the particles labeling the cell they will originate a magnetic moment that will create a fringe field. This fringe field is the one that will create the in plane magnetic components that will signal the passage of the cell by originating bipolar pulses [24] (figure 1.3 (right)).

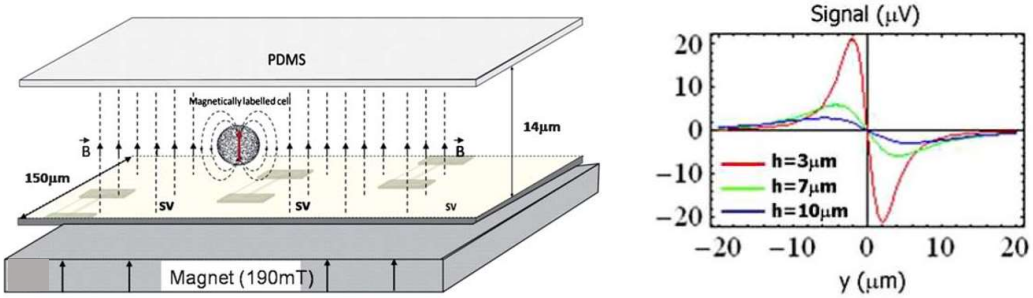

Figure 1.3 - (Left) Magnetic label being perpendicularly magnetized by a magnet in a microfluidic channel passing over SV sensors. (Right) Bipolar signal for particles with vertical moments at different heights. (Bottom) Acquisition board diagram [25].

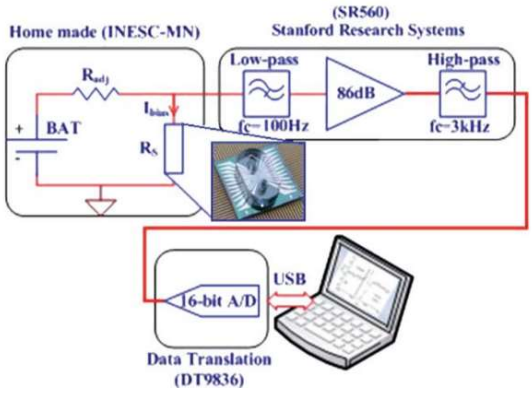

To measure the small signal generated by the fringe field of the magnetic particle the sensors were connected to an amplifier with a gain of 86 dB and filtering circuit with a 100 Hz high pass filter and a 3 kHz low pass filter were implemented. The pre-processed signal is then converted with a 16 bit analog to digital converter and using a MATLAB made scrip for continuous acquisition at a sample of 5 kHz (figure 1.3(bottom)). With this setup, the first demonstration of this technique for cytometer applications was made by detecting Kg1-a cells labeled with CD34 MicroBeads that have an overall diameter of 50 nm. The cells had on average 2800 labels each. The experiments were made in a 150 µm wide and 14 µm high microchannel. The particles passed at a speed of around 1 cm/s over 3 side by side 3x40 μm^2 SV sensors along the width of the channel. As their sample had a high concentration and was uniform they assumed that each sensor detects 27 % of the total number of cells and thus they extrapolated from the cell counts made by the middle sensor. By making the measuring of an equal sample through a hemocytometer they proved that the suggested micro flow cytometer has the same efficiency and less

than half the error for high concentration samples when compared with the hemocytometer [25]. The chip design was later modified for identification and quantification of Streptococcus agalactiae in a complex matrix (milk). In this new design 4 columns of 7 sensing units, the 1st sensing unit was 4 20x3 μm^2 SV's in series, the next 3 were 20x3 μm^2 SV's and the last 3 were 100x3 μm^2 SV's. Aligned with the columns of SV's were 4 100x100 μm^2 section microchannels through where cells labeled with 1600 Nanomag®-D-spio 50 nm beads flowed. The results showed that the quantification is still and output to be improved by a fine tuning in the external magnetic field, microfluidic channel design and flow rate [26].

INESC-MN already made other interesting different designs, using lateral flow microporous membranes [27] and an integrated sorting and detection LOC [28], also different working techniques continue to appear [29,30].

The objective of this thesis is to understand the magnetic, electronic and microfluidic parameters that affect the MPs signaling and constitute a magnetic LOC flow cytometer counting module.

After the comprehension of the background theory, fabrication processes and the integration of the existing prototypes, the final objective is to improve the effects of the external magnetic field in the SVs by choosing and positioning them, and adjust the microfluidic components in a way that the electronic and fluidic characteristics work.

All of this with the ambition of having a flow cytometer counting module able of measuring at least 4 parallel microfluidic channels in real time.

2 - Theoretical Background

2.1 - Principles of Magnetism

This work is in all ways related to magnetism and because of that its basic principles must be taken in account at all time.
The magnetization M of a magnetic material and its B-field (magnetic induction) depends on the applied H-field (magnetic field strength) as the following equations describe:

$$\boldsymbol{M} = \chi_m \boldsymbol{H} \qquad \text{equation 2.1}$$

$$\boldsymbol{B} = \mu_0 (\boldsymbol{H} + \boldsymbol{M}) = \mu_0 (1 + \chi_m) \boldsymbol{H} = \mu_0 \mu_r \boldsymbol{H} \qquad \text{equation 2.2}$$

$$\mu_r = 1 + \chi_m \qquad \text{equation 2.3}$$

where, μ_r and χ_m are the relative permeability and the magnetic susceptibility of the material.

As is seen in equation 2.1 the magnetization depends not only in the applied field but also on the material characteristics.
Different materials have different atom disposition, in different atoms exist different number and orbits of electrons and different electrons have different spin orientations. All this differences within the material will originate different magnetic moments.
The total magnetic moment of a free atom has two contributions from each electron (figure 2.1):

1. The angular momentum as the electron orbits the nucleus (strictly, the momentum of the nucleus relative to the orbiting electron).
2. The spin of the electron itself.

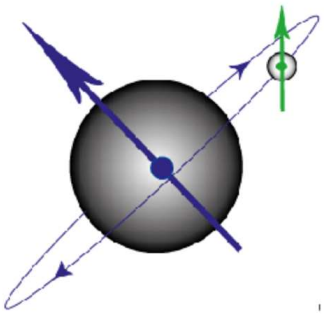

Figure 2.1 - Diagram showing the magnetic moment produced by an electron orbiting the nucleus and that produced by the spin of the electron [31].

In an atom with a single electron, there are just two magnetic fields produced which can interact. The magnetic field from the electron's spin interacts with the magnetic field from its movement around the nucleus, leading to so-called spin-orbit coupling. In an atom with more than one electron, the total magnetic moment of the atom will depend on the spin-orbit (intra-electron), spin-spin (inter-electron) and orbit-orbit (inter-electron) coupling.
The total magnetic moment can be determined by simple vector addition of the fields [31].
Under no magnetic field electrons of an atom typically tend to have the best random trajectory in order to achieve equilibrium and thus canceling each other's magnetic dipole moments resulting in no net magnetic moment and therefore no magnetic effect, however some materials are able to have their magnetic dipole moments permanently align and producing a constant net magnetic moment, the so called permanent magnets.

2.2 - Magnetic Materials

All materials are magnetic materials but according to their characteristics they will have different magnetic responses.

In many substances, the atoms have no permanent magnetic moments, in other words, the electron spins and orbital motions are all exactly balance out, so that any particular atom has no average magnetic moment. But, when applying a magnetic field some extra currents are generated inside the atom by induction and the induced magnetic moments of the atoms are directed opposite to the magnetic field. This is the mechanism of diamagnetism.

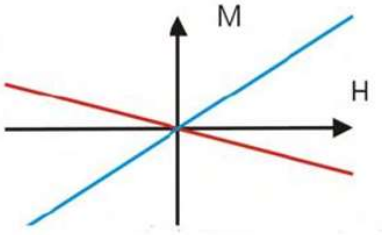

Figure 2.2 - Diamagnetic (red) and paramagnetic material (blue) behavior in the presence of an external magnetic field [32].

Then there are some substances for which the atoms do have a permanent magnetic moment. So, besides the diamagnetic effect (which is always present), there is also the possibility of lining up the individual atomic magnetic moments. In this case, the moments try to line up with the magnetic field, and the induced magnetism tends to enhance the magnetic field. These are the paramagnetic substances. This difference is due to the unpaired electrons on the partially filled shell of the paramagnetic material.

Even though paramagnetic materials have positive magnetic moments they are independent of each other and most of them don't align, but in ferromagnetic materials the magnetic moments interact between them and when under the influence of a sufficiently strong external magnetic field 100 % of them become aligned exhibiting a large permanent magnetization even when the magnetic field is removed.

A volume of a ferromagnetic material in which all the atomic magnetic dipoles are spontaneously aligned to each other is called a magnetic domain. In each domain, all the atomic moments are parallel, but the domains will be magnetized in different directions, to minimize the net free energy of the system. If placed in a magnetic field, the domains aligned with the magnetic field will start growing at the expense of other domains, resulting in an effective magnetic moment of the object.

Antiferromagnetic (AFM) materials are very similar to ferromagnetic materials but the exchange interaction creates an antiparallel alignment of the magnetic moments instead of a parallel one [32] and therefore they have no net magnetic moment.

Analog to the AFM materials the ferrimagnetic materials also have antiparallel alignment but does not lose its magnetic moment even in the absence of an external magnetic field due to their opposing magnetic moments being different in magnitude and thus exist some net magnetic moment.

Ferromagnetic, antiferromagnetic and ferrimagnetic materials change their characteristics depending on

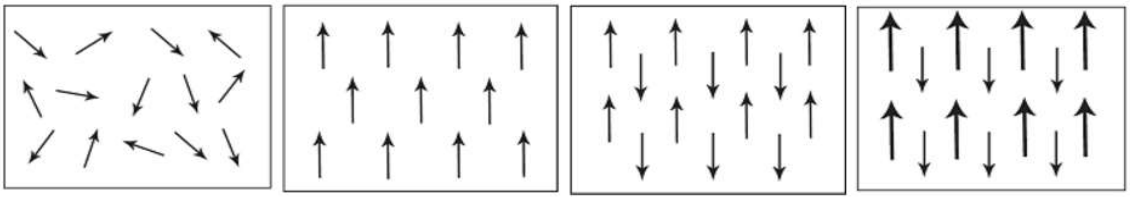

Figure 2.3 - Schematic showing the magnetic dipole moments in paramagnetic, ferromagnetic, antiferromagnetic and ferromagnetic materials, respectively [31].

their temperature. Above the Curie temperature for ferromagnetism and above Néel temperature for antiferromagnetism and ferrimagnetism the materials start responding in a paramagnetic way.

Diamagnetism, paramagnetism, ferromagnetism, antiferromagnetism and ferrimagnetism are responses of materials at the macro and micro scale which means that they respond this way when various domains are present in the material.

When the size of a ferromagnetic or a ferrimagnetic object is reduced, there is a critical size at which it will become so small that it can sustain only one domain. This is because magnetic domains are separated by domain walls (~100 nm width), and domain walls cost energy to sustain, on the other hand, large domains also cost energy to be sustained, therefore the size of the domains is decided both by the energetically optimal configuration of domain walls and the size of domains. As the particle size is reduced, this energy barrier becomes smaller since the particle has only a single domain and hence all the small magnetic moments have to be turned at the same time. If an external magnetic field is applied to a collection of such particles they will tend to align their magnetic moments with the external field and this will give a large magnetic response [32]. This implies sizes around a few nanometers to a couple of tenth of nanometers, depending on the material. The total magnetic moment of the nanoparticle can be regarded as one giant magnetic moment, composed of all the individual magnetic moments of the atoms which form the nanoparticle. This is called the superparamagnetism. Superparamagnetic materials are these ferromagnetic particles surrounded by a dielectric medium. This medium allows each particle to be independently magnetized. Superparamagnetic materials are only magnetized in the presence of a magnetic field and become demagnetized when the field is removed (figure2.4).

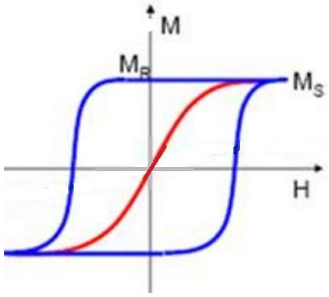

Figure 2.4 - Superparamagnetic (red) and ferromagnetic material (blue) behavior in the presence of an external magnetic field [31].

2.3 - Magnetoresistance

Magnetoresistance (MR) is the dependence of resistivity of a material depending on the strength of an applied external magnetic field.

$$MR(\%) = \frac{R_{max} - R_{min}}{R_{min}} \times 100 \qquad \text{equation 2.4}$$

All conductors display some level of MR, usually with a change in resistivity of less than 1% [33]. However, in the late 70s, the progress of thin films technology generated different perspectives concerning material sciences, as the control and deposition of small thin films with a thickness of only a few angstroms (Å) was made possible. New classes of materials arose, composed of multilayers, exhibiting new properties. The origin of these new properties is related to the characteristic aspects of the multilayer, namely, the thickness of the layers, the roughness of the interfaces, and overall behavior of the multilayer magnetic domains [34].
According to the characteristics of the materials we can have different types of MR namely ordinary MR, anisotropic MR, giant MR, tunneling MR, colossal MR, and ballistic MR [35].

2.3.1 - Giant Magnetoresistance

The giant magnetoresistance (GMR) phenomenon is a quantum-mechanical effect caused by the spin-dependent scattering of spin-polarized conduction electrons in the ferromagnetic layers due to these materials disparities in the number of spin-up and spin-down electrons at the Fermi level and thus displaying spin-polarized electron transport. Electrons with the spin aligned with the majority of spins in the ferromagnetic material will be able to travel without scattering, the other way around, if aligned antiparallel to the majority of spins, scattering will occur and the resistance will be greater.

The GMR effect was first reported by Baibich et al. in 1988 in Fe/Cr superlattices [36], and in 1989 by Binasch et al. [37] in Fe/Cr/Fe trilayers. In these cases, where alternating ferromagnetic and nonmagnetic layers are assembled, the magnetic direction of the ferromagnetic layers aligns in an antiparallel fashion throughout the structure due to exchange coupling.
As the layers align in an antiparallel way the electron scattering becomes more probable, the electron mean free path decreases and therefore increasing the resistance. But when a strong enough external field is applied, the ferromagnetic layers alignment becomes parallel, reducing electron scattering and the resistance decreases. Without the presence of the magnetic field, the layered structure returns to the antiparallel alignment of magnetic layers (figure 2.5).
The number, arrangement, and composition of the layers determines the type of GMR formed, but the common factor is that the thickness of each layer must be on the order of the mean free path of an electron in the material [33].

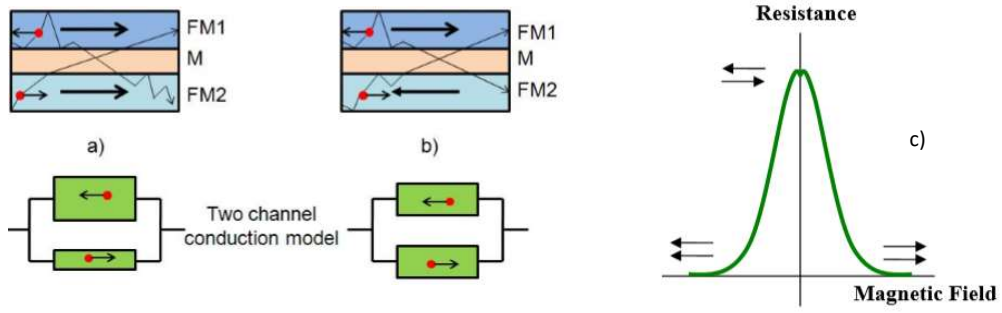

Figure 2.5 - Giant magnetoresistive effect. Two channel conduction model of the GMR effect in FM1/M/FM2 structure when FM1 and FM2 are a) parallel or b) antiparallel. In this model, each spin channel is represented by a resistor. If the spin of the electron has the same orientation than the moment of the layers, the resistance is low. In the opposite case, the resistance is high [34]. c) Magnetoresistive curve of a GMR effect [35].

2.3.2 - Spin Valve Device

The spin valve (SV) structure is a type of GMR material proposed by Dieny et al. [38] in 1991. SVs are composed by 3 main layers with different properties, the free layer composed of FM material, the spacer layer which is a conductive material and the pinned layer that has a FM and an AFM layers coupled together (figure 2.6). In this configuration, the pinned layer has a fixed magnetization through the exchange coupling between the FM and the AFM layers. This exchange bias field must be strong enough to maintain the magnetization direction of the pinned layer in the way that when under the influence of magnetic field to measure only the free layer is affected and thus acting as the sensing layer. The pinned layer can be over of the spacer, being called top pinned SV, or under it, being called bottom pinned SV. Furthermore, the magnetic moment of the pinned layer is defined by the layer's anisotropy, the called easy axis, and the free layer, as the name refers, it free and thus has the same orientation as the pinned layer but depending on the anisotropy direction the SV has different responses. These anisotropy directions are defined during deposition through the application of a magnetic field or patterning by shape anisotropy. If the free layer anisotropy is perpendicular to the pinned one the SV will have a linear response between the maximum and minimum resistance states, but if the anisotropy is established parallel to the pinned layer the SV will have a step like response in the near zero field. In this thesis, the SVs used are top pinned with cross anisotropy configuration. Using the crossed anisotropy configuration, the patterning of the SV and the thickness of the free layer are key factors due to the shape anisotropy of the free layer. The patterning is done in a rectangular shape with the width in the direction of the easy axis and thus the free layer will tend to align its magnetization through the longer dimension

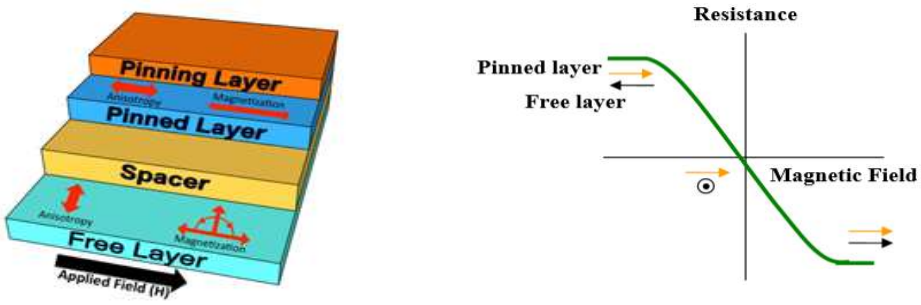

Figure 2.6 - Sketch diagram of a crossed anisotropy top pinned SV [34] and the respective magnetic response [35].

(length) of the SV shape [34]. This way, at zero field the free layer is perpendicular to the easy axis, when under positive fields the magnetization of the free layer will tend to align parallel to the magnetization of the pinned layer conferring lower resistance, for negative fields the free layer will be antiparallel to the pinned layer conferring higher resistance. The sensor only detects magnetic fields in the direction along its width since only fields in this direction will be able to rotate the free layer's magnetization.

In this type of GMR devices a current in-plane (CIP) is used for the biasing of the SV and since the SV behave like a resistor it responds by Ohm's law (V=RI). Also, the spin valve resistance depends on the length (L) and the width (W) of the device, increasing with the increase of length and decreasing with the increasing of width as seen in the equation below.

$$R = R_{sq} \times \frac{L}{W} \qquad \text{equation 2.5}$$

Where the R_{sq} is the square resistance (ρ/t = resistivity/sheet thickness) and its constant for a certain SV structure.

So, when a SV is properly patterned and biased the sensors response is [32]:

$$\Delta V = -\frac{1}{2} \times MR \times I_{bias} \times R_{sq} \times \frac{L}{W} \times < cos(\theta_p - \theta_f) > \qquad \text{equation 2.6}$$

Where MR is the sensor magnetoresistance ratio, I_{bias} is the sensor bias current, θ_p is the angle between the pinned layer magnetization and the longitudinal direction, θ_f is the angle between the free layer magnetization and the longitudinal direction and $< cos(\theta_p - \theta_f) >$is taken over the active area of the sensor.

Other important characteristic of the SV is its field sensitivity, in other words, his capability to transduce the magnetic field to voltage which is traduced by the variation of resistance ΔR along the magnetic field where the SV has a linear response ΔH.

$$S = \frac{\Delta R}{\Delta H} [\Omega/\mathrm{Oe}] \qquad \text{equation 2.7}$$

Although the sensitivity units used in this thesis are presented in a normalized way that is used to compare different sensors.

$$S = \frac{\Delta R}{R_{min} \times \Delta H} = \frac{MR}{\Delta H} [\%/Oe] \qquad \text{equation 2.8}$$

2.4 - Principles of Microfluidics

The principles of microfluidics have been studied since the 19th century but only with the emergence of MEMS in the early 1980s the availability of technologies made possible the practical use of this technology and since the 1990s there has been huge evolution in LOC applications due to it. Microfluidics is the scientific area that studies fluid flow and fluid properties at the microscale, which can be either gases, liquids or plasma states of matter.
At the macroscale, fluid behavior is determined by volume forces such as gravity and other inertial forces, but at the microscale phenomena like diffusion, viscosity, surface tension, hydrophilic or hydrophobic nature of the different molecules and interfaces and other intermolecular forces such as Van der Waals forces, hydrogen bonds, and salt bridges are now the dominant effects [35,40].

2.4.1 - Fluids' Characteristics

Fluids are characterized by several properties including: density, specific weight, pressure, viscosity, and surface tension.
The density represents the mass per volume of the fluid. A fluid that has a constant density is known as an incompressible fluid. Compressible fluids have densities that vary with changes in temperature and pressure. For the purposes of this thesis only incompressible fluids will be considered.
Specific weight is the weight per unit volume of a fluid, in other words, the product of a fluid's density and gravity.
Pressure is the normal force per area of a fluid at rest. The pressure of an incompressible fluid varies linearly with depth since its density does not vary with location or pressure.
The viscosity of a fluid is a measure of its resistance to continuous deformation. When a fluid located within a microfluidic channel of stationary walls (case of study in this thesis) experiences a velocity gradient as a result of deformation due to the fluid's velocity it has the tendency to stick to the boundary of the channel, resulting in what is referred to as a no slip condition, which means that the velocity at the fluid/solid interface is zero. Fluids for which the viscous stress due to his flow, at every point, is linearly related to the local strain rate are designated as Newtonian fluids. Fortunately, most common fluids, both liquids and gases, are Newtonian as is the case of this thesis.
Finally, surface tension is the cohesive force of the fluid on his surface that produce a net attraction towards the interior of the fluid where these attractive forces are equally balanced [41].

2.4.2 - The continuity equation

The continuity equation is the equation of conservation of mass, for fluid dynamics, and the first fundamental equation of fluid dynamics.

$$\frac{\partial \rho}{\partial t} = -\nabla \cdot (\rho v) \qquad \text{equation 2.9}$$

Where, ρ is the mass density and $v(r,t)$ is the velocity vector for the fluid.
As this work uses incompressible fluids we can further reduce this equation.

$$\nabla \cdot v = 0 \qquad \text{equation 2.10}$$

This equation can be used for fluids that have velocities much smaller than the velocity of sound in the fluid as is the case in microfluidics.

2.4.3 - Navier-Stokes equation

The Navier-Stokes equation is Newton's second law derived for fluid dynamics. It is the second fundamental equation of fluid dynamics.

$$\rho(\partial_t v + v \cdot \nabla)v = \nabla \cdot \sigma + \rho g + f \qquad \text{equation 2.11}$$

Where, σ is the stress tensor describing the pressure forces and the viscous forces, g is the gravity acceleration and f corresponds to the remaining forces acting on the fluid. The system described in this thesis is in a stationary regime, which means that all time derivatives are zero, the channel length is perpendicular to the gravity and as such the force from gravity is compensated by the normal force, the incompressible fluid assumption makes the stress tensor to be reduced considerably meaning that tensor calculations can switch to vector calculations. Taking this into account the Navier-Stokes equation becomes:

$$\rho(v \cdot \nabla)v = -\nabla p + \eta\nabla^2 v \qquad \text{equation 2.12}$$

where η is the dynamic viscosity of the fluid and p is the pressure (both coming from the reduced stress tensor). It is seen that there is a linear and a nonlinear part. The nonlinear part $\rho(v \cdot \nabla)v$ represents inertia forces, and the linear part $-\nabla p + \eta\nabla^2 v$ represents the pressure and viscous forces [32].

2.4.4 - Reynolds Number

The Reynolds number is a dimensionless number that relates the effects of inertial forces to those of viscous forces on a fluid and thus it can be used to characterize the flow behavior.

$$Re = \frac{\rho u l}{\eta} \qquad \text{equation 2.13}$$

Where, u is the characteristic velocity scale and l is the characteristic length scale. The characteristic length scale can also be called hydraulic diameter (D_h) and for non-circular channels, as is the case of this thesis, can be calculated by:

$$D_h = \frac{4 \times A}{P} \qquad \text{equation 2.14}$$

Where, A is the cross section and P is the wetted perimeter of the channel.
As the equation describes, if we have a Re > 1 the inertial forces dominate over the viscous forces, opposingly if the Re < 1 the viscous forces overcome the inertial.
Around Re < 2000 the flow is called laminar, between 2000 and 3000 it's called a transitional flow and Re > 3000 there is a turbulent flow.
In a laminar flow, the fluid has well defined streamlines that are parallel to the channel walls and to one another, on the other hand, turbulent flow possesses cross currents that result in eddies and swirls of the fluid making its position in time unpredictable. Transitional flows are the presence of both laminar and turbulent flows.

2.4.5 - Poiseuille Flow

Generally, in the case of microfluidics the Re << 1 and as was shown above the inertia effects play only a minor role and thus the nonlinear part of Navier-Stoke equation is negligible, leaving the linearized Stokes equation:

$$\eta\nabla^2 v = \nabla p \qquad \text{equation 2.15}$$

Now, instead of a highly complex non-linear equation, using the Stokes equation and assuming a pressure-driven steady-state flow of an incompressible Newtonian fluid through a cylindrical tube of length >> radius and a no slip condition we have the Poiseuille equation or the Hagen-Poiseuille equation.

$$v(r) = \frac{\Delta p}{4\eta l}\left(R^2 - r^2\right) \qquad \text{equation 2.16}$$

Where Δp is the pressure difference between the inlet and the outlet, l is the length of the tube, R is the radius of the tube and r is the distance from the center (r=0) to the wall of the tube.
But, the fact is that no analytical solution is known to the Poiseuille flow problem with a rectangular cross-section and the way to go is to calculate a Fourier sum representing the solution. Therefore, the Poiseuille equation for rectangular cross-sectional channels with the above assumptions is:

$$v_x(y,z) = \frac{4W^2}{\eta\pi^3}\left(-\frac{\partial p}{\partial x}\right)\sum_{i=1,3,5,\ldots}^{\infty}(-1)^{(i-1)/2}\left[1 - \frac{cosh(i\pi z/W)}{cosh(i\pi H/2W)}\right]\frac{cosh(i\pi y/W)}{i^3} \qquad \text{equation 2.17}$$

Where W is the width and H is the height of the channel.

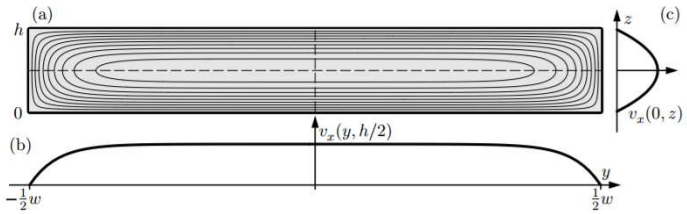

Figure 2.7 - Contour lines for the velocity field v_x for the Poiseuille flow in a rectangular channel (a). A plot of v_x along the long center-line parallel to y (b) and along the short center-line parallel to z (c) [42].

However, in microfluidics the aspect ratio of a rectangular channel can often be so large that the channel is well approximated by an infinite parallel-plate configuration.
Due to the symmetry, the y coordinate drops out and we end with the ordinary differential equation with the solution being a simple parabola [42].

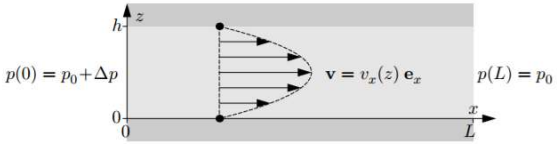

Figure 2.8 - Plot in the xz plane of an infinite, parallel-plate channel of height h. The fluid is flowing in the x direction due to a pressure drop Δp over the section of length l. [42].

$$v_x(z) = \frac{\Delta p}{2\eta l}(H - z)z \qquad \text{equation 2.18}$$

2.5 - Magnetic Beads

Ranging from nanometer to micrometer sized particles, these “Magic Bullets” [43] may be used in diagnostics for MRI contrast agent, bioseparation, cell sorting, immunoassays, purification, enzyme immobilization, sensing and transfection, but also, in therapy for several severe human diseases, like anemic chronic kidney disease and musculoskeletal system associated diseases, localized drug delivery, hyperthermia or MRI mixed radiotherapy.
Ferromagnetic, paramagnetic or superparamagnetic particles have been chosen according to the application, transduction mechanism and assay type. There are already hundreds of functional magnetic microbeads available from companies such as Invitrogen, Micromod and BangsLabs with a plethora of chemical and biological surface coatings including amine, carboxyl, epoxide, hydroxyl, streptavidin, polythymine (for polyadenylated DNA), proteins A or G and a variety of antibodies [20].

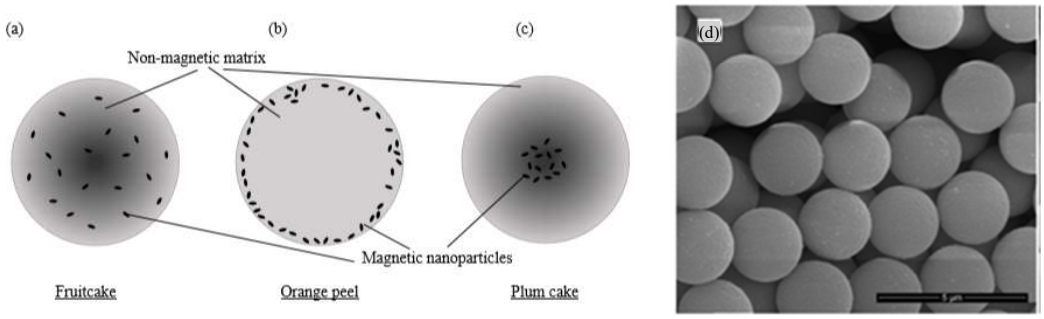

Figure 2.9 - Variations of nanoparticle embedding in a non-magnetic spherical matrix creating superparamagnetic beads. Fruitcake (a), orange peel (b) and plum cake (c) like distribution of magnetic nanoparticles [43]. SEM image of 2.7 μm magnetic beads (d) [44].

Many kinds of magnetic beads have been used for a wide range of applications in the LOC and μTAS devices, as new types of particles or functional surfaces appear also the range of applications of those devices will widen.
The use of magnetic beads has become so desirable due to the extra degree of freedom provided by their ability to be manipulated by external magnetic fields and by the magnetic stray field induced it, independent of the microfluidic or biological process. Furthermore, as biological samples are mostly composed of diamagnetic entities their magnetic background is very small and thus the background noise is low. Their magnetic properties are very stable over time and are generally not affected by reagent chemistry or exposure to light, also they can be easily recovered from a dispersion and reversibly re-dispersed [43].
The magnetic labels used in most biological magnetic devices are superparamagnetic beads, usually formed by particles of iron oxide (magnetite or maghemite) and dispersed in a silica or polymer matrix. Superparamagnetic properties are ideal for sample manipulation since they do not agglomerate after switching off or removing the external magnetic field since no permanent magnetization remains.
When using magnetic beads as labels there are some features that must be considered:

- Size: Depending on the target to be labeled one must first decide the size of the particle. For example, if only one particle will bind to the target, like in small DNA fragments, or if the target should be covered by them, as is the case of bacteria where we can link several particles to its wall.
- Magnetic moment: The magnetic particles should have a magnetic moment adjusted to the type of application. For magnetophoretic applications, if we have different particles to separate their magnetic moments must be different enough to follow different paths but in for detection by

MR sensors the magnetic moment must be as high as possible providing larger fields when exposed to an external field.

- Magnetic behavior: For most application, magnetic labels should not present remnant moment to avoid particle clustering and thus superparamagnetic particles are normally used.
- Biocompatible surface: As is the case of size, biocompatibility depends on the target. The magnetic particles should have an affinity surface for molecular recognition components, such that it should be capable of being functionalized and have a high binding efficiency for the target molecule and a high specificity.

3 - Materials and Methods

The production of micrometer sized sensors, microfluidic channels, their integration, characterization and evaluation required several specialized equipment and techniques.

3.1- Microfabrication

When working in the micrometer size scale and below, a free of dust and other impurities environment is needed in order not to contaminate the samples. As such INESC-MN operates a 250 m^2 clean room (class 100 and class 10 areas) and adjoining 250 m^2 grey area (nominally class 10,000) [45]. The classification of the clean room is done according to the number of particles per cubic meter at a specified particle size. The low levels of environmental pollutants in the clean room are maintained by a regular cleaning and only authorized persons with the respective vestments are allowed inside.

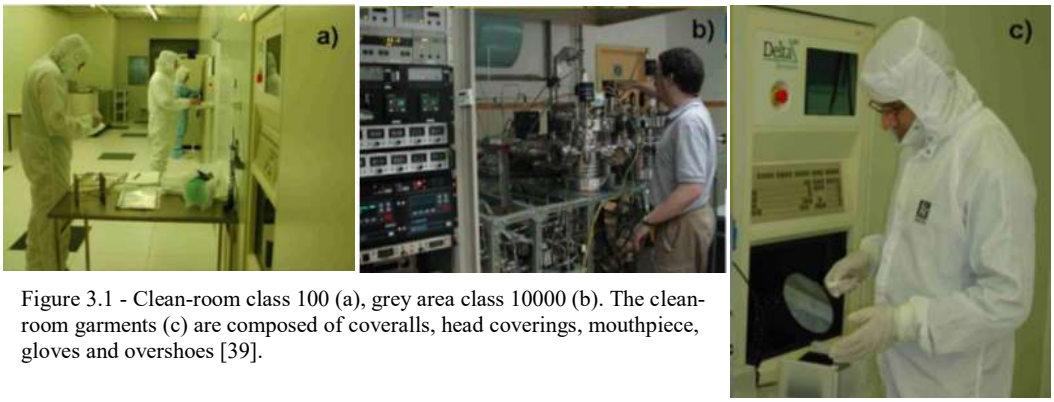

Figure 3.1 - Clean-room class 100 (a), grey area class 10000 (b). The clean-room garments (c) are composed of coveralls, head coverings, mouthpiece, gloves and overshoes [39].

3.1.1 - Thin Films Deposition Systems

Ion Beam Deposition

Ion beam deposition (IBD) is one of the techniques used for thin film deposition. Both IBD machines in INESC-MN (Nordiko 3000 and Nordiko 3600) are composed of a deposition gun, an assist gun, a revolver type target holder and a substrate table. For the deposition of thin films, the deposition gun fires a plasma created ion beam that strikes and sputters a target of material, which then coats the substrate tilted toward the target with the sputtered material. The material hits the substrate due to the electric potential between them. The revolver type target holder allows for individually target selection for deposition making possible an automatic process of deposition of multilayers and without vacuum break [32].

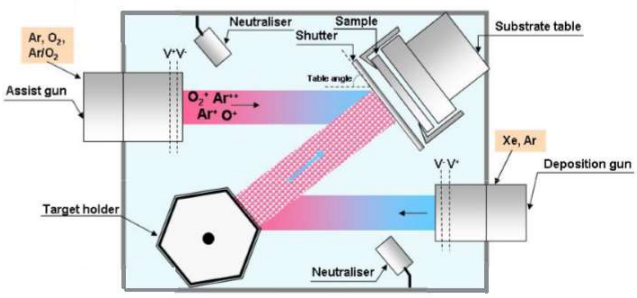

Figure 3.2 - Schematic of an IBD system functioning and main components [32].

The substrate table has a permanent magnet array, producing a magnetic field that defines the easy axis of the films during the deposition. The table at which the substrate is held is continuously being rotated during the deposition in order to achieve a better deposition

uniformity throughout the sample [34]. And the not less important assist gun is also an ion source that delivers noble or reactive ions at the surface of the growing film improving their quality in terms of stability, density and dielectric properties.

Sputtering Deposition

Sputtering deposition is other of the methods available for deposition of thin films at INESC-MN and allows for a higher deposition rate than IBD.
Sputter deposition is a type of physical vapor deposition (PVD).
In the vacuum chamber of the sputtering system, the target is close to a magnetron and by controllably introducing atoms of an inert rare gas and applying voltage to the target the ions in the gas will be accelerated towards the target. Along the way, by scattering events, these ions will ionize neutral atoms and all the resulting ions will towards the target and ionize even more atoms that will eventually result in plasma ignition. At this time, most of the atoms in the vicinity of the target are ionized and the magnetron placed near the target will confine the ions and electrons trajectories along the magnetic field lines. In this plasma cloud some ions will contribute to the continuous plasma ionization, but the ones with a larger energy than the binding energy of the atoms of the target may collide and result in the emission of several atoms from the target since these are neutral they are unaffected by the electric or the magnetic field and thus free to travel across the vacuum chamber onto the substrate to form the deposited film.
At INESC-MN there is a Nordiko 7000 for Deposition of thin films of AlSiCu alloy and TiW(N).

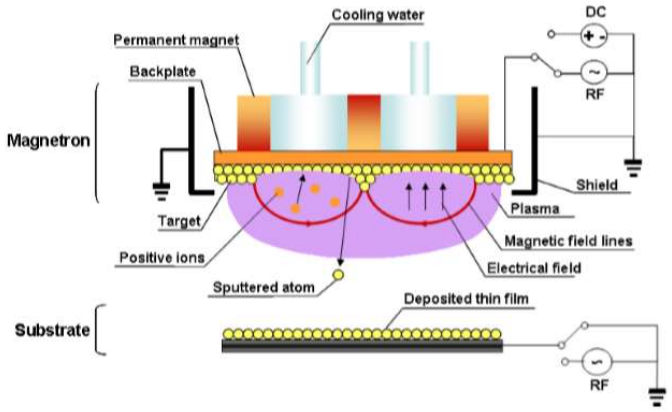

Figure 3.3- Schematic of a sputter deposition system functioning and main components [32].

Chemical Vapor Deposition

Other deposition technique processed at INESC-MN is chemical vapor deposition (CVD). In its simplest form, CVD involves flowing a precursor gas or gases into a chamber containing one or more heated objects to be coated. Chemical reactions occur on and near the hot surfaces, resulting in the deposition of a thin film on the surface.
The existing machine at INESC-MN is a Electrotech Delta Chemical Vapor Deposition System that uses the plasma-enhanced Chemical Vapor Deposition (PECVD) method. This technique uses a radio-frequency power source in order cause a plasma discharge strong enough to generate the activation energy necessary to induce the dissociation of the silane gas (SiH4), often diluted with other precursors. The main difference between the original chemical vapor deposition is that the thin film growth is done by electron impact rather than by thermal energy.
The schematic of the PECVD is similar to the PVD but in this case the target is an inflowing gas [47].
In INESC-MN the Electrotech Delta Chemical Vapor Deposition System is used for deposition of thin films of silicon dioxide and silicon nitride [46].

3.1.2 - Patterning Techniques

The definition of micro and nanometer size structures is made by designing the desired structures into a mask in a CAD software. The patterning techniques will transfer these structures to the thin films in a way that the surplus material can be removed.

Photolithography Process

As the name suggests the photolithography technique is a process that "writes" on "rock" through light. The "rock" is a light sensitive material called photoresist (PR) that being irradiated will undergo structural and chemical modifications. If a negative PR is employed the exposer to light will make structural modifications that will make the PR insoluble, on the contrary, if a positive PR is used the exposed areas will be weakened and soluble.
Being a light sensitive process, all the steps of a photolithography process should be done under a light that doesn't emit the wavelengths which the PR is sensitive. For that purpose, inside the class 10 clean room there is a so called yellow room where all the equipment necessary for the photolithography is.
To transfer the mask with the desired shape into the sample through photolithography are necessary three main steps (figure 3.4):
• Coating – The coating step is done by deploying PR over the sample and use a spinner to make it rotate at high speed in order to achieve the best sheet uniformity. The PR viscosity/rotation speed relation will define the height of the PR sheet. After the spin-coating, the PR is soft-backed to remove solvents and stress while promoting adhesion.
• Exposure – In this step, the CAD designed mask will be transferred to the PR by emitting the wavelength in which the PR is sensitive although different PR exhibit different sensitivities to different wavelengths. Depending on the positive or negative nature of the PR the light should be directed to the inside or outside of the structures.
• Development – The developing step is the removal of the light weakened PR areas by immersing the sample in a liquid solvent. The remaining structures will provide a defined shape of the desired mask [39].

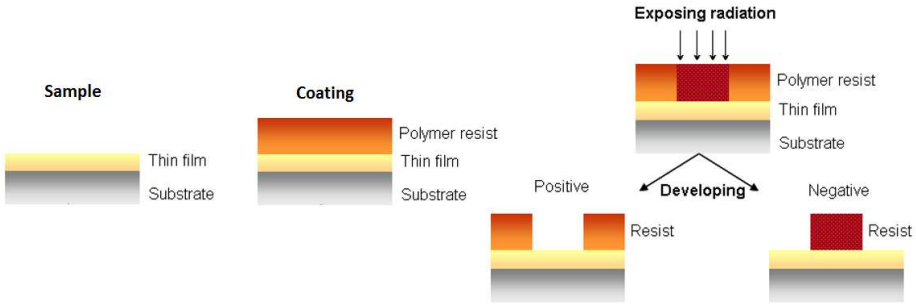

Figure 3.4 - Schematic of the photolithography main steps [32].

In INESC-MN this process is used not only for the definition of the thin films but also for the microfluidic channels mold.
In the case of the thin films definition, a positive PR (PFR7790G27cP - JSR Electronics) is employed and due to its positive nature, the sample suffer a pretreatment in order to promote the PR adhesion. This pretreatment is made in the Vapor Prime machine and consist in a dehydration step, the deposition of an organic compound (HMDS, Hexamethyldisilane, C6H18Si2) under high temperature and in vacuum. The coating and development steps are accomplished in an automated system, the Silicon Valley Group Track (SVG). The coating track has a PR dispersion, a spinning and a soft bake station. Following to

the exposure step, a Direct-Write Laser (DWL 2.0, Heidelberg Instruments) is used, where the laser sweeps the sample according to the designed mask which is aligned with high precision. The CAD

Figure 3.5 - Silicon Valley Group Track for the coating and development steps (left). Direct-Write Laser 2.0 from Heidelberg Instruments (right). As it can be seen by the light they are localized in the yellow room area.

design mask is converted into a laser machine language. The DWL exposes the CAD mask inside the structure when is defined as inverted, if is defined as non-inverted the DWL exposes outside de structures. Then, back at the SVG track, the sample is baked to stop uncompleted PR reactions, is left to cool and passes to the station where a suitable developer (JSR Micro PTH70EG) is used to remove the exposed PR (positive PR). After the development, the sample goes to the last station where it is washed with deionized water and dried by high speed spinning [32].

For the microfluidic channels, the photolithography process explained before is used to make a physical mask in a glass substrate covered by aluminum except in the channels structures. This is called a hard mask and is opaque outside the channels structures and transparent inside them.

Using a spinner, a negative PR (SU-8) will coat a silicon substrate and after a soft bake, the hard mask is mounted over the PR coated silicon substrate and irradiated by an iron doped metal halide UV lamp. After development, only the structures transparent in the hard mask will stay on the substrate and that way becoming the channels mold.

The first photolithography technique is called optical lithography and the second is contact lithography. They allow the manipulation for the selective removal or deposition of material in the substrate, which is achieved either from etching or by lift-off techniques.

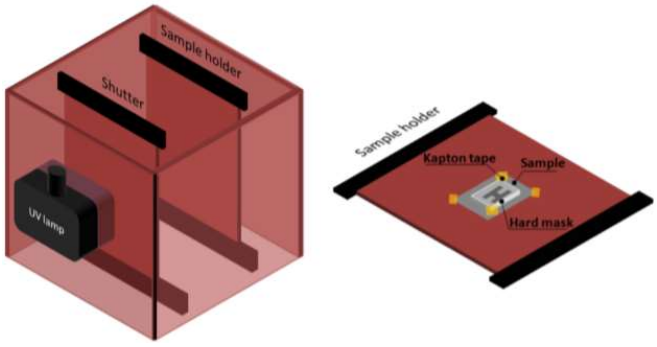

Figure 3.6 - Scheme of the UV system designed for the contact photolithography. General overview of the geometry of the exposure system and how the sample and hard mask are mounted [32].

3.1.3 - Etching

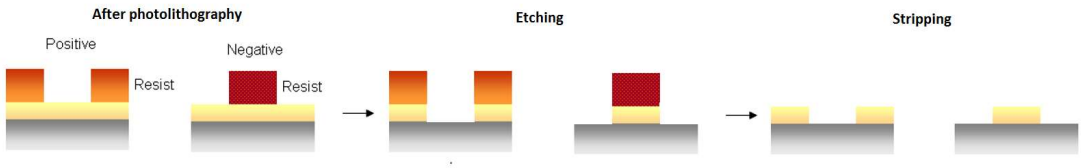

Figure 3.7 - Schematic of the etching main steps.

Once the PR mask is transferred onto the thin film by photolithography the sample is ready for the etching step. Etching is the name of the process in which the non-protected areas of the thin film are removed.
There are several etching techniques that are characterized by the material removing principle.
The physical etching is a type of dry etching in which the thin film is removed by the acceleration of ions of inert gases directed to the material surface and due to the momentum transfer the surface atoms are knocked off. The ion milling is a physical etching technique performed in an IBD equipment. In etching mode, only the assist gun is used to bombard the inert gas ions to the substrate, the angle of incidence will determine the lateral profile of the thin film structures.
Sputter etch is also a physical etching technique that is performed in a sputtering system, but in etching mode the substrate, instead of the target, is connected to an RF power supply making it to attract ions from the plasma turning the substrate in a target itself and by the same principle removing the surface atoms.
The chemical etching can either be a dry or a wet process but in the case of this thesis only wet processes were used. In the chemical etch used, the processes are purely chemical and when the sample is submersed in an etching solution the exposed material will react and will be dissolved.
In this thesis, the chemical etching used were for the removal of aluminum in which is used an etch solution with acetic acid 3.3%, nitric acid 3.1%, phosphoric acid 3%, pure, at room temperature and for the removal of PR in which is used Microstrip 2001 in a 65 ºC ultrasound bath.
Other of the etching processes used is the reactive ion etching (RIE). The RIE is a combination of physical and chemical etching. By physical etching the surface of the material becomes more reactive and when the reactive gas phase is employed they can react more readily augmenting the etch rate. The RIE equipment used at INESC-MN is a LAM Rainbow 4400 system and was employed in the etching of Si_3N_4.

3.1.4 - Lift-Off

Lift-off is also a technique used to transfer the desired mask to the thin film but contrarily to the etch process the thin film will stay in the places where no PR is deposited. In the lift off technique, the PR is deposited before the thin film and in the photolithography step, the positive PR is radiated inside the desired structures. After development, the PR will remain outside the structures. By depositing the thin film over the PR and finally removing the PR, the so-called lift-off, only the desired thin film structures will remain. As was explain before the PR is removed by chemical etching using the Microstrip 2001.

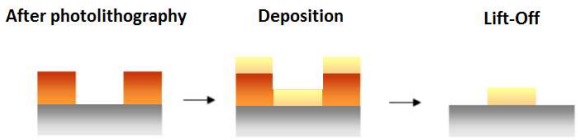

Figure 3.8 - Schematic of the lift-off main steps.

3.1.5 - Magnetic Thermal Annealing

Annealing is a method where a material is heated until a high temperature, maintaining it and then slowly letting it drop. This technique allows the material to reduce its structural imperfections and this way releasing internal stress and homogenizing its structure.

In a FM or AFM material, after maintaining the high temperature above the blocking temperature, if the cooling down step is done under a magnetic field, not only the homogenization of the structure will improve but also, we can define the orientation of the easy axis. This is called magnetic thermal annealing.
At INESC-MN the setup of magnetic thermal annealing consists in a quartz vacuum chamber with two positions, the first with a programmable heating system and a second where the sample cools under the field of a 1 T permanent magnet.

Figure 3.9 - Magnetic thermal annealing setup.

3.1.6 - Wafer Dicing

The fabrication of the chips is done in silicon wafers and in one wafer it's possible to have a vast number of chips, depending on their size, and as such its indispensable to have precise cutting machine. To make this job INESC-MN is equipped with a Disco DAD312 automatic dicing saw equipped with a microscope to align the wafer with the 50 µm saw. Normally this procedure requires a coating of PR over the sample to prevent damage that the resulting dust may create.

3.2 - Micromachining system (Milling Machine)

The milling machine is a micromachining system used in INESC-MN to drill and mill through poly-methyl-methacrylate (PMMA) to produce support, alignment or structural accessories to the chips or setups. This machine can sculpt a 3-dimensional shape with a micrometer resolution in the desired bulk material, it uses 3 step motors positioned in the x, y and z axis. The x and y motors move only in their plane with the piece locked and the z motor only in the up-down direction holding the high frequency motor that spins the tool. With these degrees of freedom its only possible to drill in the top view of the material.
This way the CAD design is a 2D drawing of the desired shape that in the DXF format can be converted by the DesKAM 2000 software where we introduce the depth of the drilling, pocketing or contouring. As the name reveals, drilling is the drill of a hole with the diameter of the tool used, pocketing it's an inside to the outside thinning of the chosen area and contouring is the milling in the perimeter of a structure. DesKAM 2000 using the drawings and the configuration of the tools computes the trajectories that each motor has to make to complete the task and as output results a G-code file in the DNC format. With this done its used the Mach2Mill software to control the motors in the trajectories calculated by DesKAM 2000. To control the speed rotation of the tool its used a spindle controller that its manually set for each tool. There are 2 kinds of tools, the drills and the mills, the first ones are to drill and

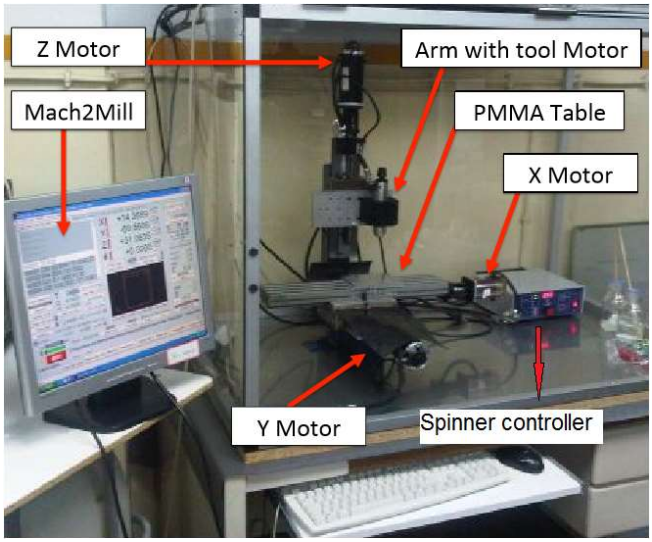

Figure 3.10 - Milling machine setup [34].

the second ones are for pocketing and contouring, as for their diameters, at INESC-MN they can range from 100 µm to 3 mm.
To ensure that the tools don't break its custom to apply water to the zone where the tool is working to reduce the heat, as the rotation creates friction that if not reduced will make the PMMA to melt and glue to the tool that in that case normally breaks.
The milling machine used is a TAIG Micro Mill from Super Tech & Associates.

3.3 - Microfluidics fabrication (Microchannels)

Microfluidics fabrication has seen different kinds of materials to create structures. In the beginning, silicon and glass were the chosen since the techniques for fabrication were well established, then, came poly-dimethyl-siloxane (PDMS) since the micro molding technique was straightforward, it was cheaper and its chemical and physical properties allow devices with different useful functionalities. Now with the industry requirements, more reproducible techniques are needed and as such the use of thermos-plastics by injection molding has been the chosen technique for mass production. But, as the investigation world is always in change and modifications in designs are frequent, PDMS casting was the used in this thesis as it is a cheap and versatile process. [32]

3.3.1 - SU-8 mold

The SU-8 mold is the "negative" of the microchannels as it is the elevation in the base of the mold that will create the channels. SU-8 is a kind of negative PR used to coat a silicon substrate with the mold size. The thickness of the microfluidic channels will vary according to the rotation speed in the spinner (figure 3.11). The viscosity of the SU-8 is the main factor for the spreading of the PR over the substrate. The SU-8 2000 PR can origin film thicknesses from 0.5 to 40 µm with just one coating.

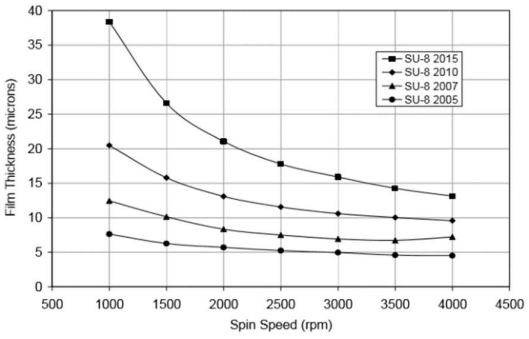

Figure 3.11 - Film thickness vs spinner rotation speed of 4 different viscosities SU-8 2000 PR [48].

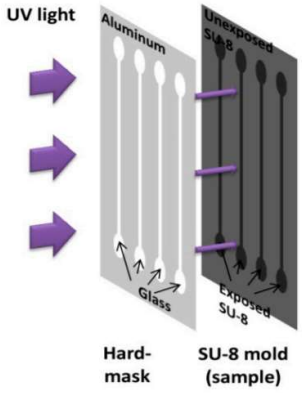

Figure 3.12 - Schematics of hard mask placement and contact lithography [34].

After the coating and cooking of the SU8 a hard mask is needed.
A hard mask is a silicon substrate coated with a thin layer of aluminum and after lithography, wet etched to remove the aluminum from inside the structures. This will create an opaque glass with windows in the positions where the channels should be.
Then by contact lithography and using the hard mask to define the structures, the sample is baked again and developed. Leaving only the unexposed SU-8 and therefore the mold (figure 3.12).

3.3.2 - PDMS mold

The PDMS mold is made through the milling of 3 PMMA plates micromachined in the milling machine.

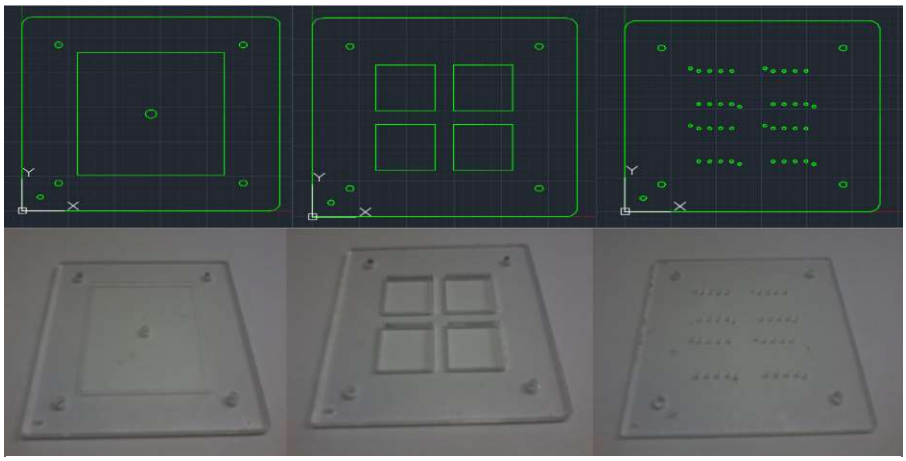

Figure 3.13 - AutoCAD design of the PDMS mold (up) and the PMMA plates that constitute it (down), the bottom, middle and top plates from left to right.

The bottom PMMA plate is constructed to be the support where the SU-8 mold will fit, the middle PMMA plate is the one that define the thickness of the PMDS and the top one has small holes for the connection of the end of the channels to the outside. In these holes small metallic rods are fit until they touch the SU-8 mold to create the outlets and inlets, even more there are extra holes for the PDMS injection. The 4 outside holes serve for the alignment of the PMMA plates and consequently the SU-8 and the metallic rods, this alignment is done by introducing 4 screws in these micromachined holes.
As the figure describes the mold was designed to produces 4 PDMS structures.

3.3.3 - PDMS casting

For the PDMS casting, the mold is assembled with the SU-8 mold mounted in the bottom plate and the metallic rods in the respective holes, the 4 alignment screws are put in the respective holes and to ensure more strength between the plates 4 office springs are placed in each side.
To prepare the PDMS for injection in the mold, the prepolymer of dimethyl-siloxane is mixed with a curing agent in a weight ratio of 10:1. To remove the gas bubbles created by the mixing of the prepolymer with the curing agent the recipient is putted in a desiccator for degassing for 1 hour. The desiccator is simply a vacuum chamber and thus removes the gas out of the solution (figure 3.14).

Figure 3.14 - Desiccator used to degas PDMS.

After the degassing, the PDMS is sucked to a syringe and injected inside the mold through a blunt needle. The PDMS is injected until no air bubbles exist inside the mold.
Finally, the mold is leaved to cure for 1 hour in a 70 ºC oven.

3.4 - Permanent Bonding

This technique allows to permanently bind 2 surfaces by covalent bonds which are strong enough to support high pressures inside de microfluidic channels. Since when the PDMS is removed from the mold the channels don't have a bottom side, by applying this technique to the top side of the chip and the bottom of the PDMS we will be not also concluding the microfluidic channels but with right aligning between the channels and the sensors we are integrating microelectronic with microfluidics.

At INESC-MN, the technique used for integration between chip and PDMS is a UVO cleaning in the Jelight UVO cleaner (figure 3.15) which is a machine that creates a plasma of ozone and radiates UV light over the surfaces, this way removing surface contaminants and exposing reactive chemical groups. The oxidation of both surfaces originates high concentration of hydroxyl groups that when put in contact leads to the formation of strong intermolecular bonds. Both surfaces are pre-cleaned with ethanol and rinsed with deionized water only then are placed in the UVO cleaner with the faces to bond turned up. After the process, they are placed in a tin of water to keep the hydrophilicity of the surfaces until de surfaces are aligned for permanent bonding.

Figure 3.15 - UVO cleaner, Jelight.

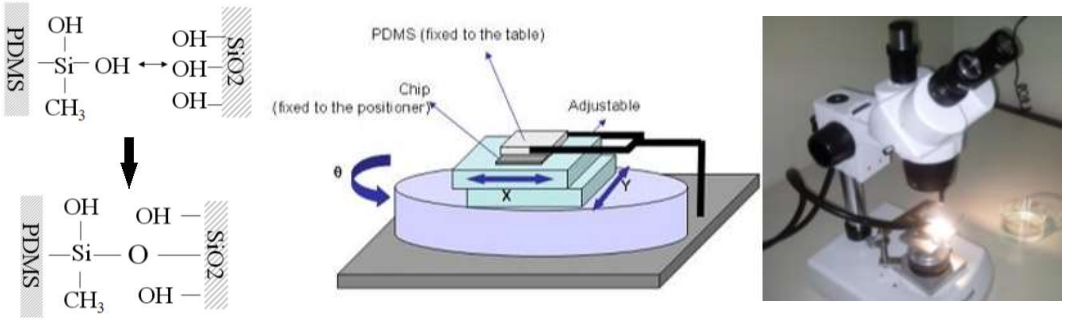

Figure 3.16 - Chemical reaction between the exposed hydroxyl groups that lead to the permanent bonding of PDMS with the chips passivation layer (left). Schematics and photograph of the micro alignment system used to align the PDMS microchannels with the SV sensors of the chip (right) [32].

The alignment is done under a magnifying glass with 160x amplification where a micro alignment system is placed. The chip is fixed in the translational table while the PDMS is fixed by a tweezers over it. Between the 2 surfaces there is water in order to keep the surfaces activation and allowing them to slip relatively to each other. By moving the translational table in the x, y and θ and using the microscope to assure the right alignment the surfaces are then left in contact and left in place to complete the reaction for 8 hours.

3.5 - Wirebonding

Wirebonding is a technique that welds thin wires to metal contacts by ultrasonic vibrations.
The wirebonding system has a fixture table where the contacts to be made will be, in this case a PCB where the PDMS bonded chip is glued.

To have a good welding the wirebonding system needs to have the right calibration and for that the ultrasound power, the time that the needle applies that power and the force with which it is applied are configurated manually.
After the right calibration is found for the right materials to weld, the mouse is used to move the fixture table under the microscope and by clicking to make the welding.
In this thesis, the wirebonding was made to connect the pads corresponding to each of the sensors in the chip to their designated copper lines in the PCB using 2.5 µm aluminum wires. For protection against breaking or corrosion of these wires, the wirebonding is carefully covered by a silicone gel and left to harden.

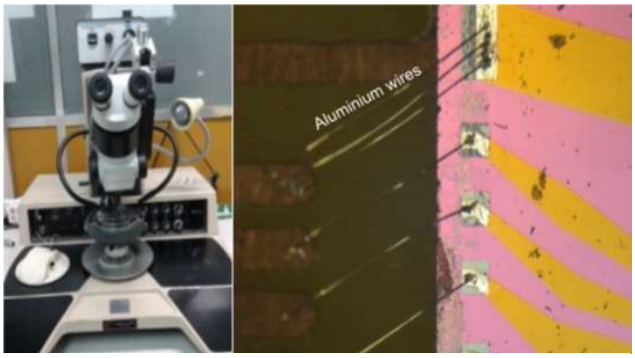

Figure 3.17 - Wirebonding system and connection of aluminum wires between PCB and chip.

3.6 - Characterization Methods

The characterization of the materials and their response under magnetic and electric fields is of the outmost importance for the complete understanding and well-functioning of the integrated parts.

3.6.1 - Vibrating Sample Magnetometer

Vibrating sample magnetometer (VSM) is the basic instrument for characterizing magnetic materials. As the name suggests, in a VSM the sample vibrates in the vertical direction while being affected by a DC magnetizing field, this originates a changing magnetic flux that is captured by the detection coils. The voltage measured across the detection coils is expressed as the product of four contributing sources:

$$V = MAFS \qquad \text{equation 3.1}$$

where M is the magnetic moment of the sample, A is the amplitude of vibration, F is the frequency of vibration and S is the sensitivity function of the detection coils.
The output measurement displays the magnetic moment, M, as a function of the applied field [49].
At INECS-MN the VSM measurements are performed in a DSM 880 VSM system, the DC magnetizing field is applied by 2 electromagnets able to generate fields up to 13 kOe, the sample holder is a quartz

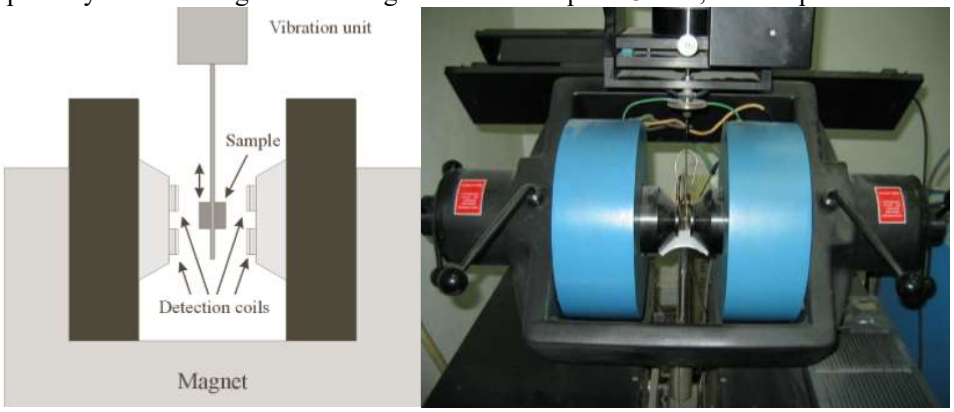

Figure 3.18 - Schematic of a VSM [49] and photograph of the DSM 880 VSM.

rod that is connected to a piezoelectric crystal which provides 200 Hz vibrations.
The VSM is used to measure the magnetic moment of bulk unpatterned SV samples and magnetic particles.

3.6.2 - Electrical Transport Characterization

The electrical transport characterization describes the sensor's response. To do this characterization, INESC-MN developed a setup that applies a DC magnetic field, varying step by step between -140 and 140 Oe, measuring the sensor's response in each step and delivering its transfer curve.
The sensor's response is acquired by connecting 2 tungsten probe needles controlled by micro positioners to the sensor's pads. With the sensor's hard axis parallel to the field, the correct needle positioning is then assured using a magnifying glass and a lamp. Through these needles the sensor is biased by a 1 mA current delivered by a Keithley 220 current source that is linked in parallel to a Keithley 182 voltmeter for the voltage reading. Another current source is used to control the magnetic field of a set of Helmholtz coils. The current sources and the voltmeter are linked to a PC by a GPIB connection for the control of the field, biasing of SVs and output reading. This is done by a INESC-MN developed software.

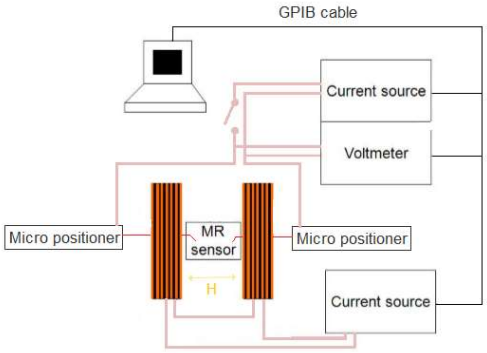

Figure 3.19 - Electrical characterization setup.

The software has as inputs the range of the magnetic field and the field steps used for the measurements and as output the values in MR, voltage or resistance versus the magnetic field. It also delivers some calculated values: the effective coupling field (Hf), the deviation that the sensor transfer curve suffers from the zero field; the coercive field (Hc), the intensity of the magnetic field required to annul the magnetization in zero field after a saturation state and the sensor's sensitivity.

3.6.3 - Profilometer

The profilometer is the most important characterization device in the fabrication of microfluidic channels. The profilometer is a machine that measures the surface profile of the SU-8 mold and as such it verifies if the SU-8 has the right heights and inclinations and thus assuring the microchannels specifications.
At INESC-MN a Dektak 3030 ST profilometer is used. This profilometer has a stage where the sample is placed and then with the help of the monitor and a zoom camera the sample is oriented and placed beneath a diamond-tipped stylus. The stylus will travel in a line over the sample and vary vertically according to the sample's profile, this will generate an electrical signal that is translated to distance units and create a graph that is displayed in the monitor or thermally printed.

4 - Biochip platform designs

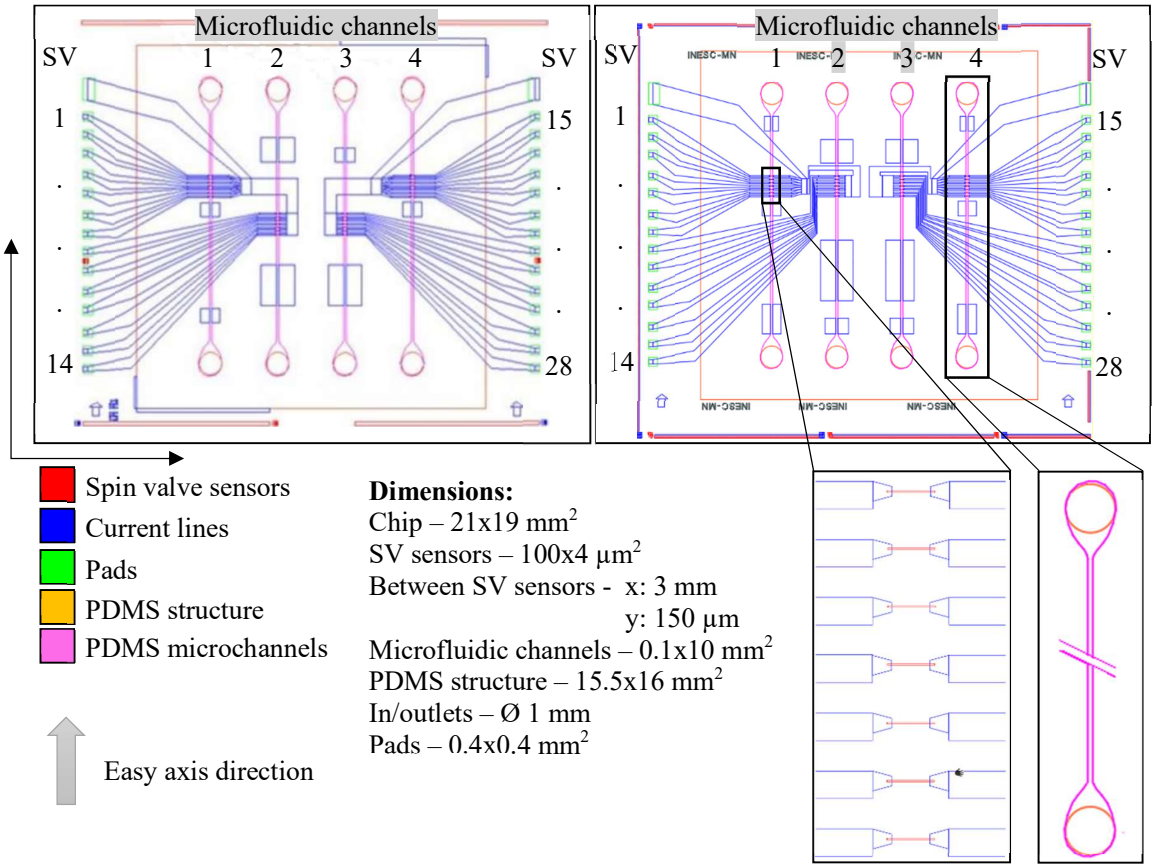

Figure 4.1 - Biochip platform AutoCad draw of the first (left) [56] and second (right) designs for MP counting and dimensions of the second one.

The first design seen in figure 4.1 was created during the development of Carla Duarte's doctoral thesis [56]. In this biochip, there are 4 columns of 7 SV sensors of 100x3 µm² size. In each column, the sensors are separated by 150 µm from each other, the first and forth column are at the same height and the second and third are 1655 µm bellow. The columns are at 3 mm distance from each other.
Aligned with the SV columns are 4 quadrangular microfluidic channels with 10 mm length, 100x100 µm² cross-sectional area and an in/outlet diameter of 1 mm. In Carla's thesis, a 20 mm x 10 mm x 1 mm neodymium PM was glued to the underside of the PCB in a way that at least one sensor was operational.

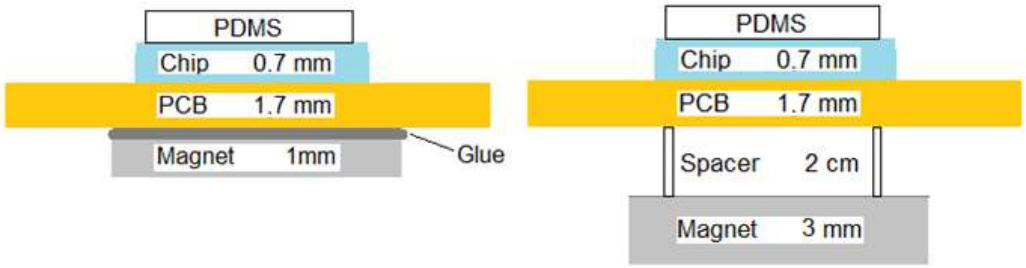

Figure 4.2 - Schematics of the integrated platform in the first (left) and second (right) designs presenting the thickness of each component.

Continuing her work, Rita Soares [57] developed the second design. In this new design, the SV sensors were changed to a 100x4 μm^2 size and all the columns were placed side by side. Also, in this design the PM was changed to a 20 mm x 20 mm x 3 mm and a structure was created to hold the magnet 2 cm below the PCB.

5 - Simulations

5.1 - Signal created by a magnetic particle

For the simulation of the signal created by the magnetic particle (MP) we firstly need to know its moment, then the field created by inducing that moment to the MPs and finally, the change in voltage that the field generates in the sensor.

After assuring the calibration of the VSM a sample with a known volume of MP is placed and the measurement is done.

The VSM measurement gives the variation of the magnetic moment of all beads contained in the solution and as such a normalization is needed to compare and know the moment of each particle.

Making use of datasheets and supplier information [51,52] to know how many particles per volume the solution has, the VSM values are divided by it and the result is the variation of the magnetic moment of each particle with the applied field. Knowing the magnetic field strength that the MP experiences we calculate its magnetic moment.

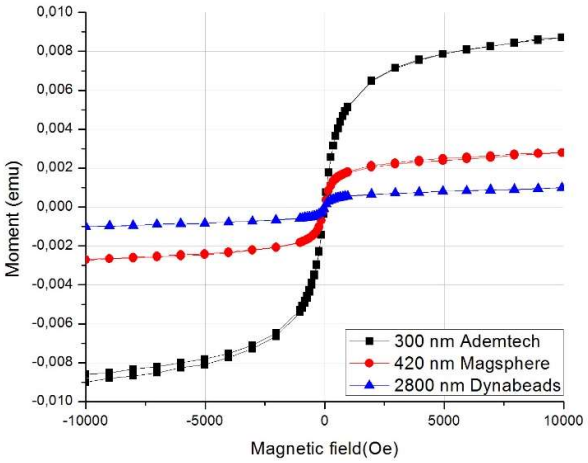

Figure 5.1- VSM measurements of the magnetic moment of a 10µL solution of 300 nm, 420 nm and 2800 nm MP.

Table 5.1 - MP saturation magnetic moment.

Magnetic particle	Diameter (nm)	Magnetic moment (emu)
Ademtech	300	$1.140*10^{-16}$
Magsphere	420	$1.761*10^{-16}$
Dynabeads	2800	$1.512*10^{-16}$

Then, to simulate the magnetic field created by the MP it is assumed that they behave as a magnetic dipole and as such it must be assumed that the MP is spherical and the dipole center is at the geometrical center of the MP.

The magnetic field created by a dipole is expressed by:

$$\vec{H}_{MP}(\vec{r}) = \left[\frac{3\vec{r}(\vec{r}\cdot\vec{m})}{|\vec{r}|^5} - \frac{\vec{m}}{|\vec{r}|^3}\right] \qquad \text{equation 5.1}$$

Where, $\vec{r} = (x - x_{mp})\hat{x} + (y - y_{mp})\hat{y} + (z - z_{mp})\hat{z}$ and $\vec{m}$ is the magnetic moment vector.

As the SV sensors are only sensitive in the direction of the easy axis, only the transverse in-plane component of the MP's fringe field affects it.
Therefore, to know the variation of the magnetic field in the sensor it must be calculated the average fringe field over the SV's free layer.
For this it is used the following equation:

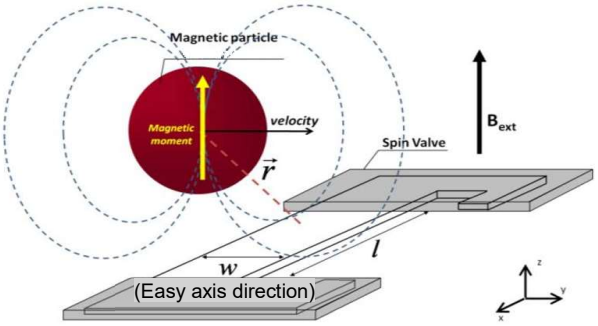

Figure 5.2 - Schematic of the MP fringe field related to the SV position [32].

$$\langle H_{sensor} \rangle = \frac{1}{lwt} \int_{\frac{-l}{2}}^{\frac{l}{2}} \int_{\frac{-w}{2}}^{\frac{w}{2}} \int_{\frac{-t}{2}}^{\frac{t}{2}} \left[\frac{3\vec{r}(\vec{r}\cdot\vec{m})}{|\vec{r}|^5} - \frac{\vec{m}}{|\vec{r}|^3} \right] dxdydz \qquad \text{equation 5.2}$$

Where, l is the length, w the width and t the thickness of the SV's free layer.
Knowing that the t dimension is much smaller than the l and w dimensions, Li and Wang [53] developed an equation for the calculation of the y component of the fringe field in the free layer ideal for computational simulations since it becomes less heavy and more exact than the numerical solution. The equation is:

$$\langle H_{sensor_y} \rangle = \frac{m_y}{lw} \left[\frac{y_b}{q_2^2} \left(\frac{x_r}{r_2} - \frac{x_l}{r_1} \right) + \frac{y_t}{q_4^2} \left(\frac{x_l}{r_4} - \frac{x_r}{r_3} \right) \right] + \frac{m_x}{lw} \left(\frac{1}{r_1} - \frac{1}{r_2} + \frac{1}{r_3} - \frac{1}{r_4} \right) + \frac{m_z}{lw} \left[\frac{z_{mp}}{q_2^2} \left(\frac{x_l}{r_1} - \frac{x_r}{r_2} \right) + \frac{z_{mp}}{q_4^2} \left(\frac{x_r}{r_3} - \frac{x_l}{r_4} \right) \right] \qquad \text{equation 5.3}$$

Where, m_x, m_y, m_z are the components of the MP magnetic moment and $x_l = -l/2 - x_{mp}, x_r = l/2 - x_{mp}$, $y_b = -w/2 - y_{mp}$, $y_t = w/2 - y_{mp}$, $r_1 = \sqrt{x_l^2 + y_b^2 + z_{mp}^2}$, $r_2 = \sqrt{x_r^2 + y_b^2 + z_{mp}^2}$, $r_3 = \sqrt{x_r^2 + y_t^2 + z_{mp}^2}$, $r_4 = \sqrt{x_l^2 + y_t^2 + z_{mp}^2}$, $q_1 = \sqrt{x_l^2 + z_{mp}^2}$, $q_2 = \sqrt{y_b^2 + z_{mp}^2}$, $q_3 = \sqrt{x_r^2 + z_{mp}^2}$, $q_4 = \sqrt{y_t^2 + z_{mp}^2}$.

Since the SV is only sensitive to the transverse in-plane component, it is not sensitive in the x direction and thus $m_x = 0$. This eliminates one of the parcels of equation 5.3, leaving us with the m_y and m_z component but as the technique that is being used the magnetization is done perpendicular to the SV's plane the m_y is also equal to 0 and consequently only the m_z parcel is used.
The perpendicular magnetization was chosen since it's the direction in which the SV is not sensitive and this way the sensors wouldn't be affected. Also, it's easier to apply and the sensors won't saturate.
Using Matlab, a script with these equations and the values of the MP moment was made to calculate the magnetic field that affects a SV sensor of 4x100 μm^2 size.

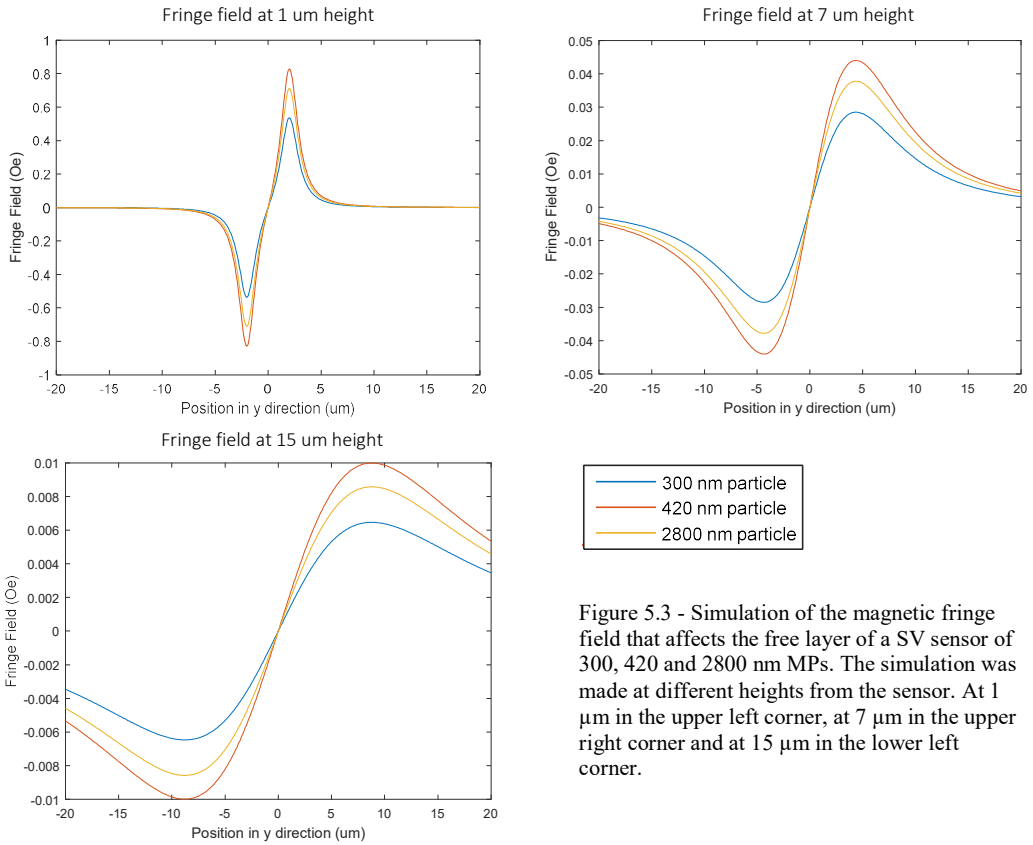

Figure 5.3 - Simulation of the magnetic fringe field that affects the free layer of a SV sensor of 300, 420 and 2800 nm MPs. The simulation was made at different heights from the sensor. At 1 µm in the upper left corner, at 7 µm in the upper right corner and at 15 µm in the lower left corner.

As it is possible to assess from these results, when the MP magnetization is constant, the amplitude of the field is dependent only on the height of the MP while the time span is dependent also on the height but varies with the velocity of the flow in the microfluidic channel.

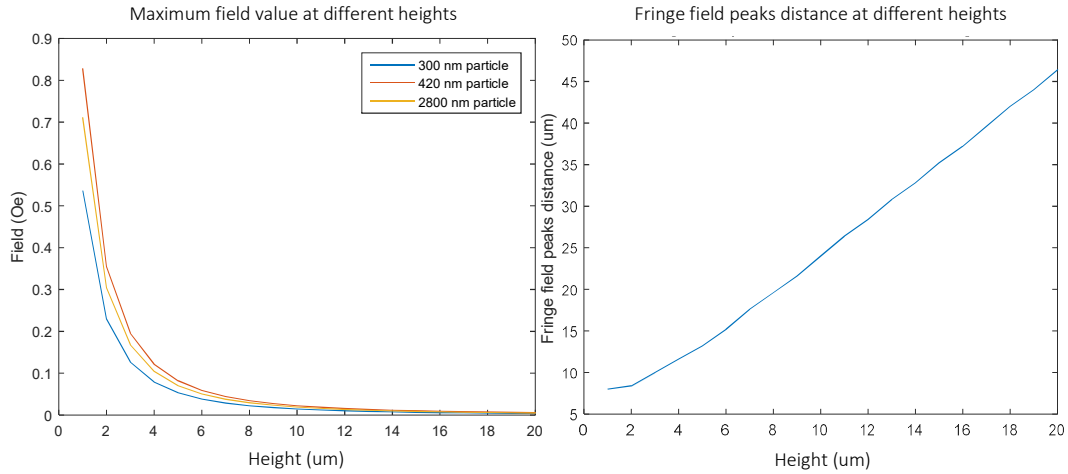

Figure 5.4 - Fringe field maximum value of the different MP in respect to the height of the particle to the sensor (left) and the field width between peaks at different heights (right).

From the above graphs, we can conclude that the fringe field created by the MP is higher when its closest to the sensor and that as they grow apart the field will decrease exponentially. The width of the fringe field on the contrary is smaller when close to the sensor and as the distance increases the width grows

proportionally. The fringe field width is related to the signal frequency but such values can't be directly calculated due to the different velocities of the flow inside the channel.
At last, to simulate the output of the sensors, the transduction of magnetic field to voltage is done by the following equation:

$$V = R_{sq} \times S \times I_{bias} \times \langle H_{sensor_y} \rangle \qquad \text{equation 5.4}$$

Where, V is the voltage, R_{sq} is the sensor's square resistance, S is the sensor's sensitivity and I_{bias} is the bias current passing through the sensor [32].

Table 5.2 - Simulated peak values of the output of the SV sensors with the MP at different heights.

	Maximum signal voltage (mV)		
Height	**300 nm**	**420 nm**	**2800 nm**
1	58.20	89.91	77.19
2	24.90	38.46	33.02
3	13.71	21.18	18.18
4	8.53	13.18	11.31
5	5.76	8.89	7.63
6	4.12	6.37	5.47
7	3.09	4.77	4.10
8	2.39	3.70	3.18
9	1.91	2.95	2.53
10	1.55	2.40	2.06
11	1.29	1.99	1.71
12	1.09	1.68	1.44
13	0.93	1.43	1.23
14	0.80	1.24	1.06
15	0.70	1.08	0.93
16	0.61	0.95	0.81
17	0.54	0.84	0.72
18	0.48	0.75	0.64
19	0.43	0.67	0.57
20	0.39	0.60	0.52

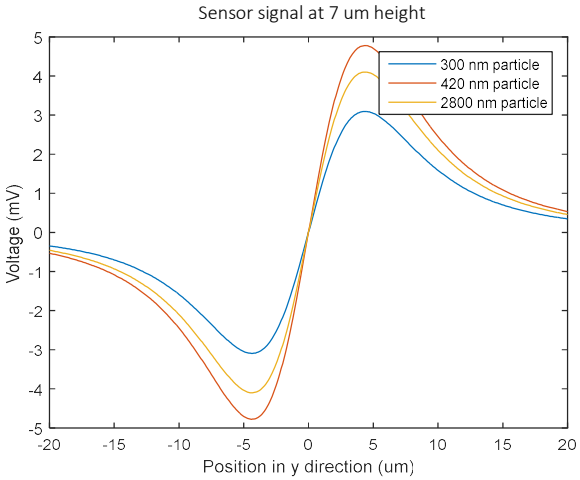

Figure 5.5 - Simulated output voltage of the SV response to the passage of a MP at 7 µm height.

By analyzing the results, we can see that the peak voltage of the output of a SV sensor signaling the passage of a MP can go from a few tenths of millivolts to a few decimals in only 20 µm. This way it's straightforward that the positioning of the MP inside the channel is of the outmost importance since from the bottom to the top of the channel the output voltage varies in 2 orders of magnitude.

5.2 - Simulation of the magnetic field created by neodymium permanent magnets.

The magnetic field created by the neodymium permanent magnet (PM) is the base for the signaling of the MP since it's the one that magnetizes the MP and induces the fringe field.
The PM must generate a field large enough to saturate the MP since it's at that point that the signal it's larger and consequentially easily detected.
Nonetheless, as is general knowledge, the magnetic field lines of a PM are closed and due to that the magnetic field is distributed in the x, y and z directions. This generates a problem since the SV sensors are affected by the x and y components which alters the sensor's transfer curve or may even saturate and turning them unusable.

To overcome this problem the PM field needs to be characterized. For that several simulations of PMs with varied sizes were made to find the more suitable one.

COMSOL was the software used for the PM simulation. Using the "Magnetic Fields, No Currents" module, creating a new material with a relative permeability (μ_r) of 1.05 [54] and from the PM datasheet [55], the initial values of remanent flux density (B_r) of 1.37 T the PM was simulated. Although, to calculate the magnetic field an air structure must be added surrounding the PM geometry (figure 5.6).

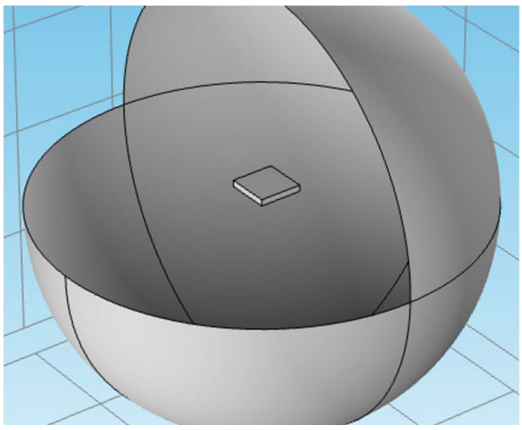

Figure 5.6 - Geometries used for the PM simulations.

The first simulations where made for the calculation of the magnetic field at 2 cm height of a neodymium PM with dimensions of 20 mm x 20 mm x 3 mm since it was the configuration used then.

The simulation was performed and slices for the x, y and z components with the magnetic field values at 2 cm height were exported to .txt files.

To process the data a Matlab scrip was designed to plot only the data in the vicinity of the magnet since the file has data in all the length of the air sphere. Then to know the area of interest, where the x and y components have less influence, a segmentation function was created to present only the values where the components have a value less than 10 Oe. At this point, each tetrahedral structure of the mesh with a value less than 10 Oe was attributed the value 1 and 0 to the rest. By applying the AND logical function between the x and y component the area of interest of the PM is presented (figure 5.7 (left)).

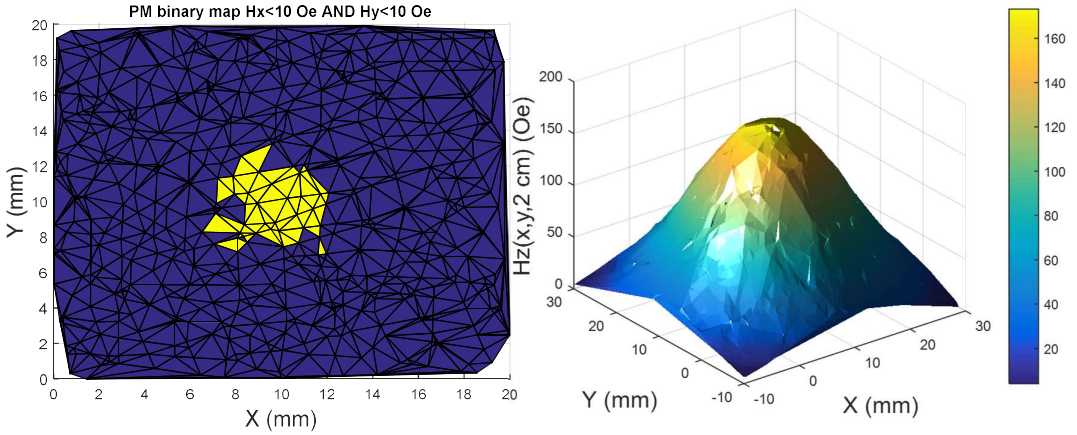

Figure 5.7 - PM magnetic field area of interest (left) and plot of the H_z magnetic field (right) both at 2 cm height of the 20 mm x 20 mm x 3 mm PM.

As is possible to understand from the above results there is an area (in yellow) where the effect of the x and y component is acceptable but the H_z, the one that will magnetize the particles, is very small since the field necessary to fully magnetize the MP is at least 1 kOe. In figure 5.1, it is seen that past the 1 kOe field all the MPs have reached the saturation state.

After analyzing these results, it was instinctive that the way to have a strong enough Hz field is to have the PM as close as possible to the microfluidic channels where the MP will pass. That case was simulated by following the same process but the slice from where the data is processed was altered to 2.4 mm height which is the sum of the 1.7 mm PCB with the 0.7 mm silicon substrate between the PM and the

surface of the chip. But, as its perceptible in figure 5.8, the acceptable area of the PM is extremely reduced even though the Hz strengthens.
In the search for new options, the simulation of magnets with different widths, lengths and thicknesses was performed. These simulations demonstrate that the thickness dimension is the one that influences both features in a trade-off manner.

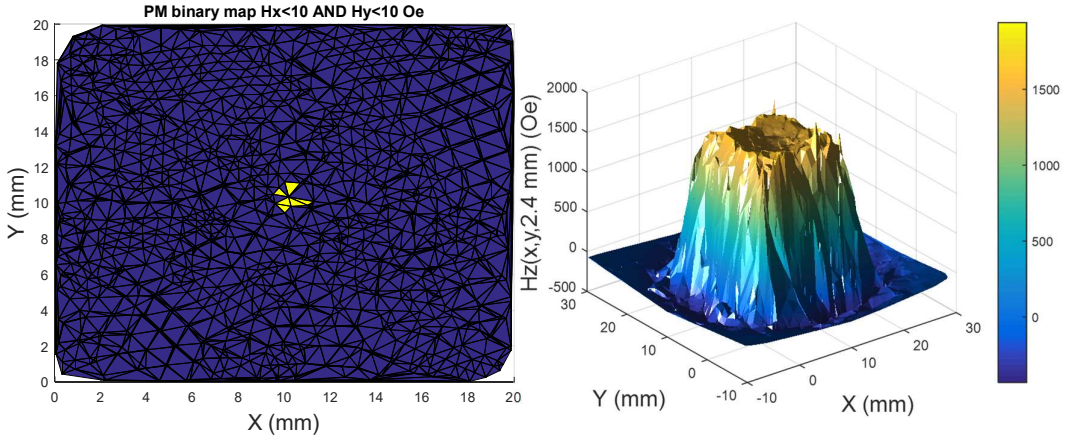

Figure 5.8 - PM magnetic field area of interest (left) and plot of the Hz magnetic field (right) both at 2.4 mm height of the 20 mm x 20 mm x 3 mm PM.

Table 5.3 - PM magnetic field acceptable area and Hz maximum magnetic field at 2.4 mm height of 3 different

PM dimensions (mm^3)	Acceptable area, Hx and Hy <10 Oe (mm^2)	Maximum Hz field
20x20x3	0.12	1939
20x20x2	1.75	1239
20x20x1	17.57	674

As table 5.3 shows, the reduction of thickness increases the acceptable area at a rate higher than decreases the maximum Hz field. Since there was a 20 mm x 10 mm x 1 mm PM available at INESC-MN the same was simulated. The results showed an acceptable area similar to the 20 mm x 20 mm x 1 mm PM and a maximum value of Hz field of 765 Oe which is an extremely good result since the magnet size is reduced, the acceptable area is maintained and the maximum Hz field is increased but is still under the desired 1 kOe field.

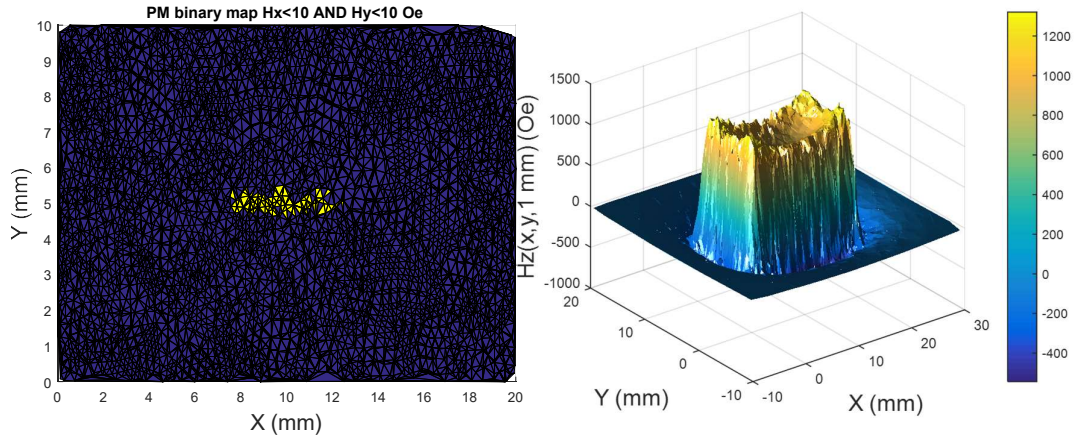

Figure 5.9 - PM magnetic field area of interest (left) and plot of the Hz magnetic field (right) both at 1 mm height of the 20 mm x 10 mm x 1 mm PM.

This created the need to reduce even more the distance between the PM and the chip surface and for that the milling machine was used to make a pocket in the PCB reducing the distance to 1 mm which is the 0.7 mm of the silicon substrate and the 0.3 mm of the pocketed PCB.
With this approach, the acceptable area increases almost to the double, to 32.1 mm, and the maximum Hz field becomes 1320 Oe. These results defined the PM position in this thesis.

5.3 - Simulation of the microfluidic channels

The simulation of the microfluidic channels fluid velocity was made to evaluate the frequency of the MP signal. As was perceived before the signal is already well defined in space but, depending on the flow entering the microfluidic channel, the velocity of the fluid will be different and as such the MP will also have different velocities due to the parabolic velocity profile of these microfluidic channels. This will make the signal duration vary and with it the signal frequency.
For this simulation COMSOL was also used but this time using the "Laminar Flow" module. The geometry was created to simulate the microchannels being used at that moment which had 10 mm length, 100 µm width and 20 µm height. Also, a pair of 3 mm height and 1 mm diameter cylinders were applied to simulate the in/outlets. The fluid passing in the microfluidic channels was simulated as water. All the assumptions explained before were applied and as such it's a Newtonian and incompressible fluid and the walls have the no slip condition.

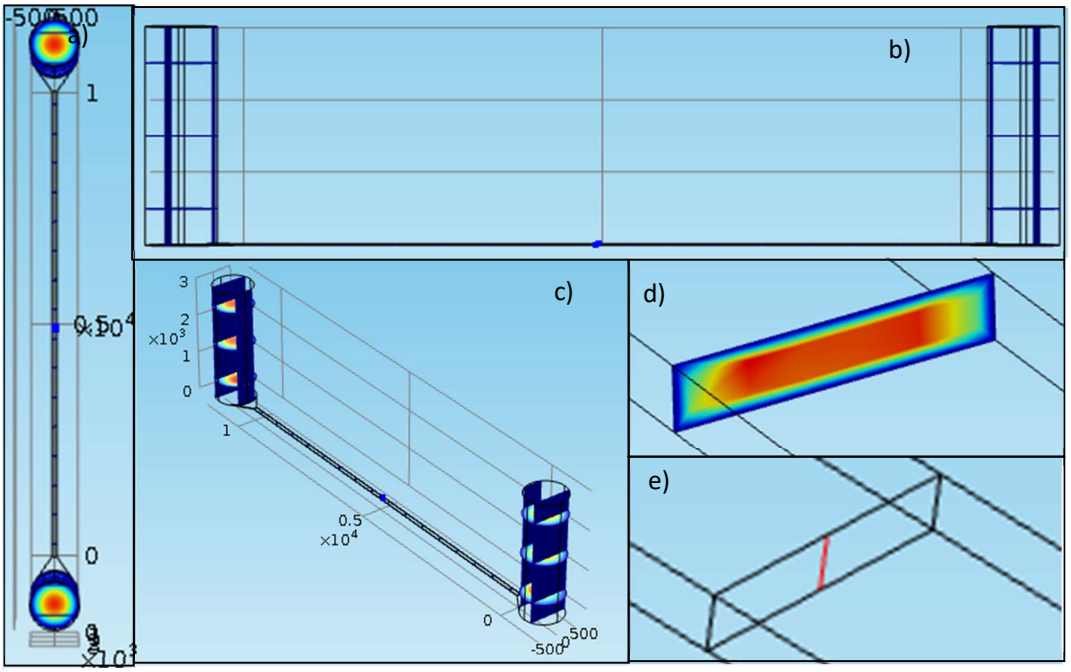

Figure 5.10 - Geometry used for the simulation of the microfluidic channels. Upper view (a), lateral view, (b) and perspective view (c). Color profile of the velocity of the fluid inside the microchannel (d) and the line from which the velocity 2D graph was achieved (e).

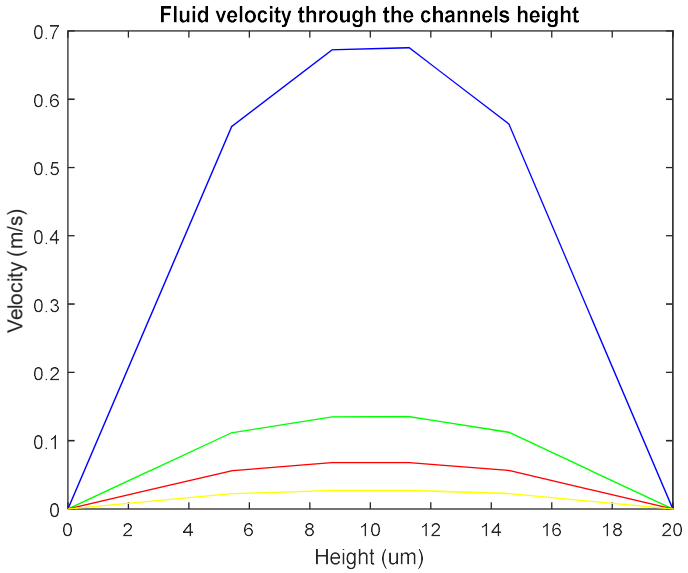

Figure 5.11 - Graph of the velocity along z in the middle of the channel's length and width for 4 different inlet flows.

During the evolution of this technique for different research purposes, the cross section of the microfluidic channels was changed and with each change the alteration of the signal's frequency. This created the need to calculate the velocity for a wide range of inlet flow rates to know which one fits the setup specifications to the used cross section (100x20 μm^2).

The simulation was made to calculate the velocity profile used 4 different inlet flow rates, 50, 10, 5 and 2 µL/min and an outlet pressure of 0 Pa to see the fluid velocity and consequently know the frequency range of each signal.

To know the frequency of the signal in correspondence to the MP velocity the following equation is used:

$$f_{signal} = \frac{1}{w_{sensor}/v_{MP}} \quad \text{equation 5.5}$$

Where, f_{signal} is the signal's frequency, w_{sensor} is the width of the SV sensor and v_{MP} is the velocity of the MP.

Table 5.4 - Simulated inlet flow rates and the corresponding velocity of the MP and maximum signal frequency.

Flow rate (µL/min)	Maximum velocity (cm/s)	Maximum frequency (kHz)
50	67.5	168.750
10	13.5	33.750
5	6.8	16.750
2	2.7	6.750

The signal acquisition setup used is established to acquire at a 50 kHz sampling frequency which means that according to the Nyquist theorem to avoid aliasing the maximum signal frequency must be 25 kHz. With this said its straightforward that the 50 and 10 µL/min inlet flow create a signal that needs a higher sampling frequency than the available one.

Since with this setup the signal's maximum frequency can't get higher than 25 kHz the maximum velocity can't also be higher than 10 cm/s which corresponds to a maximum flow rate of 7.4 µL/min. These results are under the assumption than the MP have the same velocity as the fluid.

6 - Optimization of the magnetic components affecting the SV sensors

The biochip module design still needs some improvement since as was seen, Carla's positioning of the PM was derived from Joana Loureiro's thesis [32]. Joana's thesis was the one that proved that this technique is indeed able of performing the dynamic counting of the MP but at the time only 2 SV sensors were in optimal conditions. In the second version of the biochip module the PM was separated from the PCB at a 2 cm distance which indeed made all the SV sensors in the chip to have a good transfer curve but makes the field that will affect the MP much lower than needed and as such, a step back was the way to go.

The first thing to do was to see the transfer curve of all the SV sensors in the chip without the influence of the PM. Using the electrical transport setup, the characterization of the whole 28 SV sensors in the chip was made which traduced in the mean values of:

MR – 5.98 ± 0.18 %;

Hf – 10.85 ± 0.87 Oe;

Hc – 0.36 ± 0.16 Oe;

Sensitivity – 0.217 ± 0.04 %/Oe;

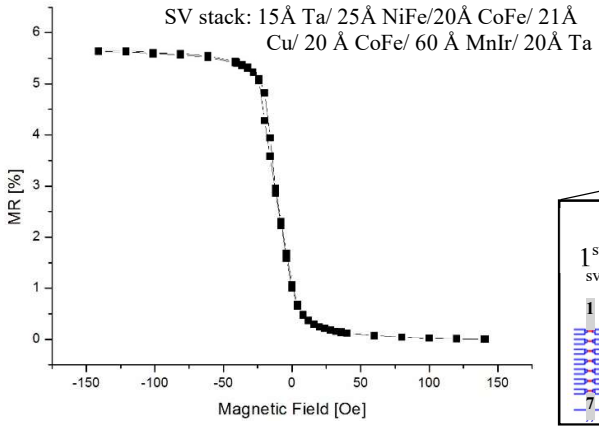

Figure 6.1 - Normal SV sensor transfer curve without any PM influence.

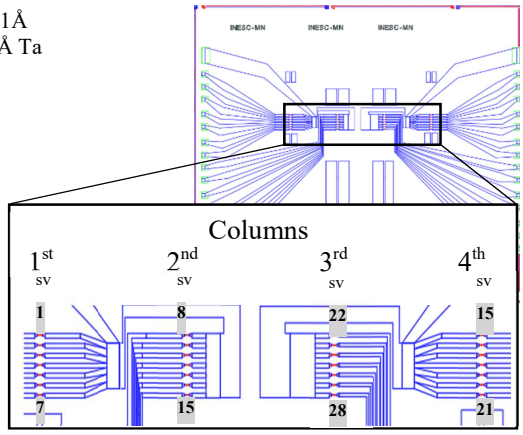

Figure 6.2 - Design of the chip used in the measurements and numeration of the SV sensors.

On a first approach, it was tried to replicate Joana's results with the manually positioned 20 mm x 10 mm x 1 mm neodymium PM but instead of using adhesive paste it was used double-sided tape what would right way reduce the PM to chip distance by at least 0.5 mm. Also, to assist in the positioning several lines, separated by 1 mm in the x direction and 2 separated by the size of the PM in the y direction, were drawn in the back side of the PCB. The expected results were achieved but as described in Joana's thesis, only a few sensors had a centered transfer curve (Hf ≈ 0 Oe) with acceptable sensitivity (S > 0.1 %/Oe). It was a work that took hours since each time the PM is moved the measurements need to be recommenced in search for the operational sensors.

In the hope to find a PM positioning that would augment the number of sensors that meet the needed conditions, it was tried the positioning of the 20 mm x 20 mm x 3 mm PM under the PCB, one 20 mm x 10 mm x 1 mm PM under the PCB and one over the PMDS and the combination of a 20 mm x 20 mm x 3 mm under the PCB and a 20 mm x 10 mm x 1 mm over the PDMS.

Table 6.1 - Schematic of the different PM positioning and the transfer curves of a sensor of the 1st and 2nd columns since the others should have the same result due to the chip's symmetry.

1st column SV transfer curve	2nd column SV transfer curve	PM positioning
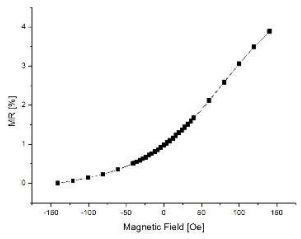	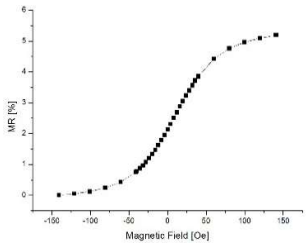	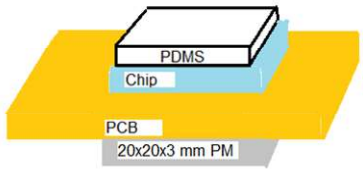
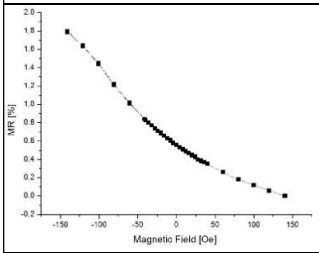	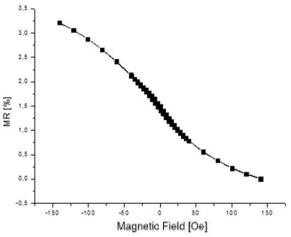	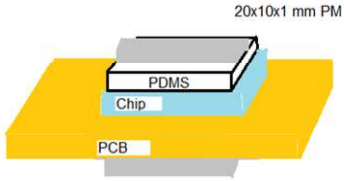
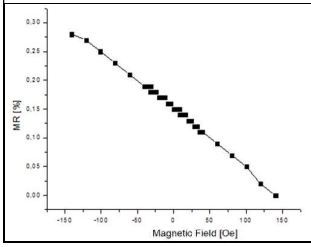	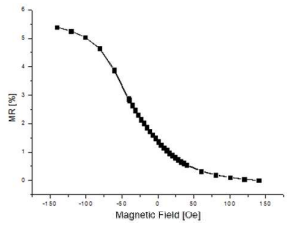	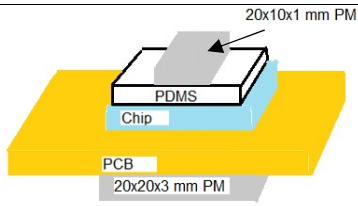

Several other positions were tried but the results were uncomprehensive and worse than the ones showed in table 6.1. As table 6.1 shows, beside the alteration in MR created by the PM, the sensitivity and the Hf values were outside the desired values. The manual positioning of the PM made the results to be very unpredictable and due to that the next step was to draw in the PCB the chip position and to drill a hole in the place where the middle of the PM coincides with the middle of the of the SV sensors matrix.

Looking at the results with this new magnet positioning, it's acceptable to assume that the proximity of the PM and the careful positioning of the PM are the way to optimize this technique. With this positioning, we can see that the middle columns (2nd and 3rd) have an appropriate sensitivity, unfortunately the outer ones have lower sensitivity values.

In respect to the Hf values, we can see that they have a pattern and that the curves are shifting in the same way in all columns in respect to their SV positioning in the chip (figure 6.3).

Although these sensitivity values may work, there is still the need to have the sensors linear response centered in zero field. As figure 6.3 depicts there are some SV's that the saturation zones are in the zero field which will make the sensor unresponsive to the MP passing. Even though these results aren't the perfect ones from here we can have similar and coherent curves along a column or a line which is a breakthrough from the previous designs.

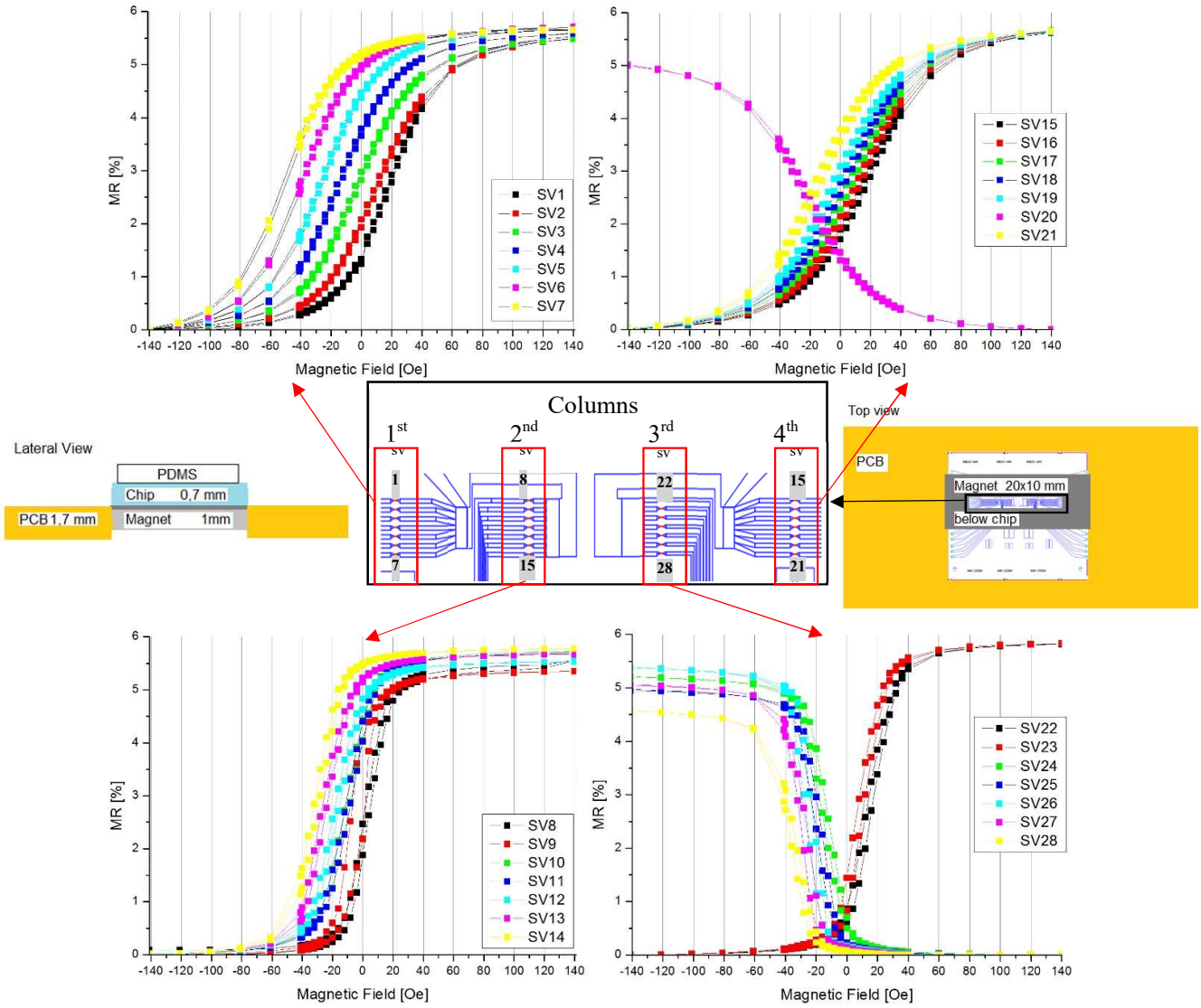

Figure 6.3 - Whole chip transfer curve characterization with 20 mm x 10 mm x 1 mm neodymium PM positioned below the chip in the micromachined hole drilled in the PCB where the center of the PM meets the center of the SV sensors matrix.

Also from these results we can prove of the theory described in Joana's thesis where she says that a transverse field (relative to the SV plane) will shift the transfer curve (left or right) and on the other hand, a longitudinal field will change the slope of the transfer curve making the sensitivity of the SV smaller [32]. Here it's shown that the transverse fields in the positive direction of the y axis will shift the curve to the right (positive Hf values) while fields in the opposite direction will shift them to the left (negative Hf values) and that the longitudinal fields, in the x axis, will decrease the sensitivity in the same way regardless of the field's negative or positive direction.

Despite this improvement, there are still differences in the curves of the 1st and 4th columns and in the 2nd and 3rd which since the chip is symmetric shouldn't occur. This problem must be, again, in the positioning and since the PM is placed in a micromachined hole the problem is due to the manual gluing of the chip in the PCB. Other problem to solve is the Hf shift from zero field, since the PM is placed

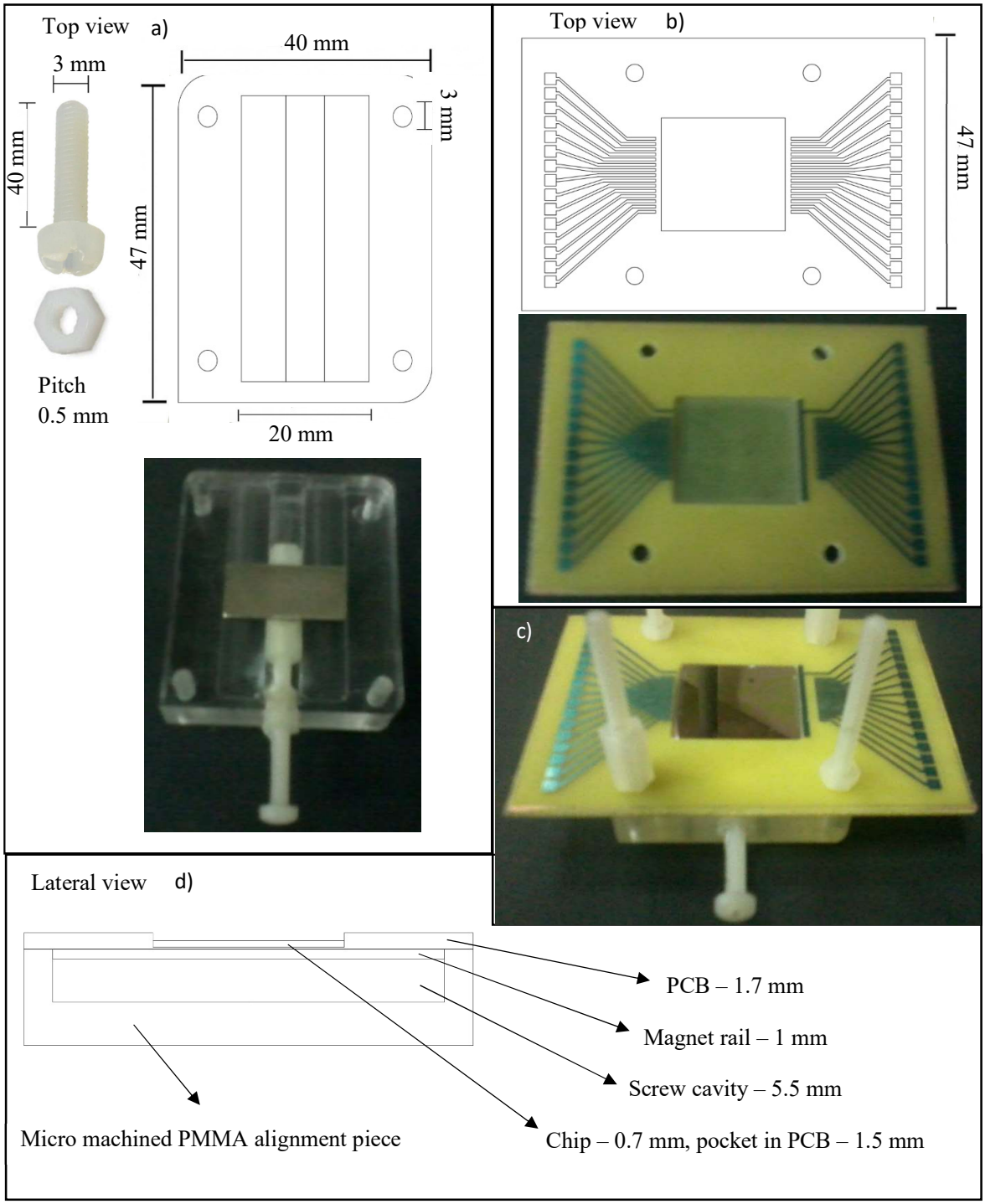

Figure 6.4 - PM – Chip Alignment system (c). Bottom piece constituted by a PMMA micromachined plate, a screw and a set of nuts (a) and top piece constituted by the pocketed PCB and 4 alignment holes (b). Lateral view of the PM – Chip alignment system (d).

right in the middle of the SV sensors matrix the deviance must come from the intrinsic Hf of the SV and as such a calibration system must exist to allow the use of SV's with distinctive characteristics.
To achieve these goals an PM/chip alignment system was designed (figure 6.4 (c)).
This alignment system is constituted of 2 parts, the bottom one (figure 6.4 (a)) which will align the PM and allow its movement to control the Hf shifting and a the top one (figure 6.4 (b)) which will align the chip. These 2 parts are aligned by 4 micromachined alignment holes.
The bottom part was fabricated in the milling machine from a plate of PMMA with a thickness of 1 cm, firstly it was made a pocket with the thickness and width of the nut (5.5x5.5 mm^2) where the magnet is hankered, secondly another pocket with the thickness and length of the magnet (1x20 mm^2) along 40 mm to do the rail in the y axis, thirdly the 4 alignment holes with 3 mm diameter and at last the contour with the a length the same size as the width of the PCB and the necessary width for these components (47x40 mm^2) extruding the piece from the rest of the PMMA plate. To finish this part and control the PM movement a 3 mm diameter hole was made in the top of the screw rail to fit the screw that was fixed in place by gluing 2 nuts to it and that way making it rotate always in the same place making the nut where the PM is hankered the only moving piece.
The top part it's just a 1.5 mm deep pocket in the PCB with the size of the chip (21x19 mm^2) and the 4 alignment holes also performed in the milling machine. These 4 alignment holes will make the chip positioning perfectly aligned with the rail where the PM will slide and the 1.5 mm pocket will minimize the distance between the PM and the SV sensors, also assuring the alignment.

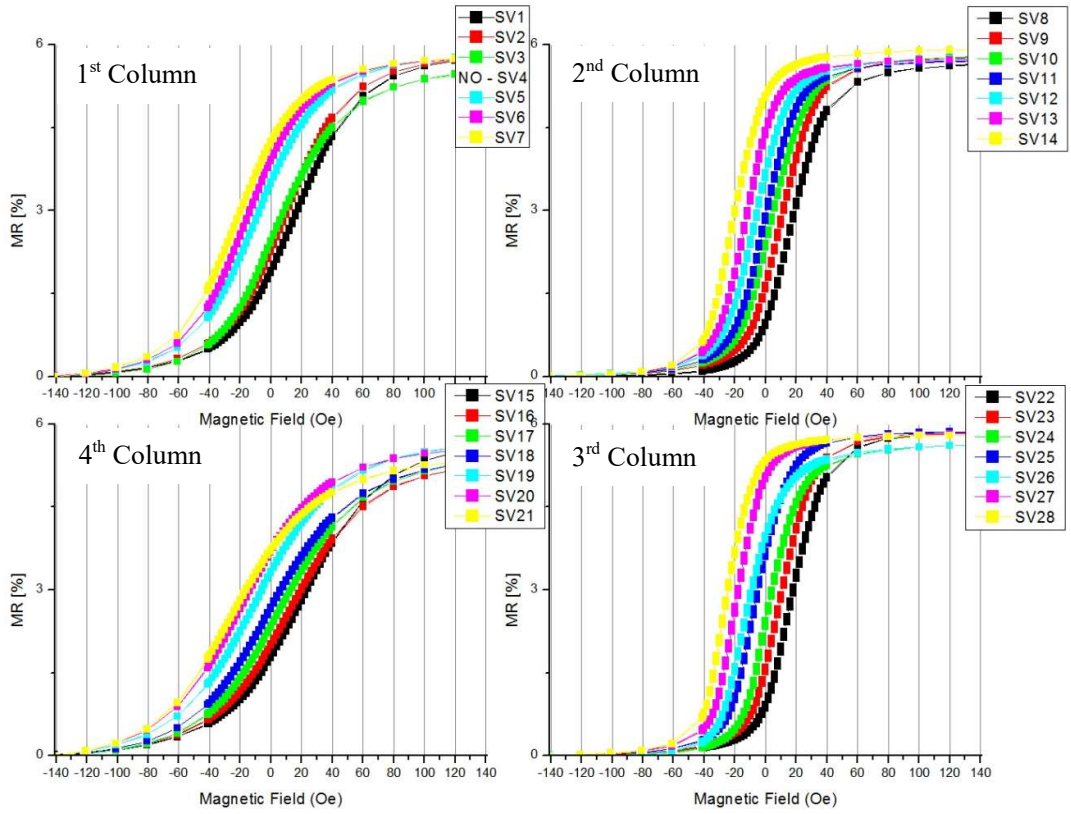

Figure 6.5 - Whole chip transfer curve characterization using the PM/chip alignment system with a 20 mm x 10 mm x 1 mm neodymium PM.

Table 6.2 - Hf values of the SV sensors in the chip without the PM influence.

Chip Columns							
1st		2nd		3rd		4th	
SV nº	Hf [Oe]	SV nº	Hf [Oe]	SV nº	Hf [Oe]	SV nº	Hf [Oe]
1	10.56	8	8.30	22	10.83	15	10.83
2	7.73	9	7.92	23	10.12	16	10.67
3	8.35	10	7.37	24	13.79	17	9.74
4	OF*	11	8.64	25	8.92	18	8.90
5	10.63	12	8.46	26	9.46	19	10.52
6	7.32	13	8.51	27	10.90	20	9.75
7	7.06	14	7.25	28	10.26	21	8.95

*Overflow (malfunctioning SV sensor)

Table 6.3 - Hf values of the SV sensors in the chip with the PM influence.

Chip Columns							
1st		2nd		3rd		4th	
SV nº	Hf [Oe]	SV nº	Hf [Oe]	SV nº	Hf [Oe]	SV nº	Hf [Oe]
1	15.46	8	17.49	22	17.44	15	19.38
2	9.08	9	10.72	23	10.50	16	12.31
3	5.22	10	4.42	24	3.15	17	6.29
4	OF*	11	-0.03	25	-5.51	18	0.10
5	-9.01	12	-6.35	26	-10.49	19	-9.39
6	-15.29	13	-12.60	27	-18.14	20	-17.70
7	-21.32	14	-20.19	28	-25.10	21	-22.44
Mean	-2.64		-0.93		4.02		-1.63
SD	14.67		13.17		15.33		15.56
	Sensor from which the magnet was aligned						

*Overflow (malfunctioning SV sensor)

Table 6.4 - Sensitivity values of the SV sensors in the chip without the PM influence.

Chip Columns							
1st		2nd		3rd		4th	
SV nº	S [%/Oe]	SV nº	S [%/Oe]	SV nº	S [%/Oe]	SV nº	S [%/Oe]
1	0.262	8	0.241	22	0.172	15	0.185
2	0.292	9	0.233	23	0.183	16	0.168
3	0.211	10	0.231	24	0.196	17	0.221
4	OF*	11	0.221	25	0.220	18	0.292
5	0.251	12	0.198	26	0.216	19	0.188
6	0.298	13	0.227	27	0.234	20	0.260
7	0.245	14	0.278	28	0.258	21	0.275
Mean	0.260		0.233		0.211		0.227

*Overflow (malfunctioning SV sensor)

Table 6.5 - Sensitivity values of the SV sensors in the chip with the PM influence.

Chip Columns							
1st		2nd		3rd		4th	
SV nº	S [%/Oe]	SV nº	S [%/Oe]	SV nº	S [%/Oe]	SV nº	S [%/Oe]
1	0.068	8	0.124	22	0.139	15	0.098
2	0.070	9	0.126	23	0.138	16	0.072
3	0.066	10	0.122	24	0.143	17	0.077
4	OF*	11	0.130	25	0.147	18	0.067
5	0.070	12	0.126	26	0.134	19	0.057
6	0.074	13	0.147	27	0.167	20	0.057
7	0.074	14	0.147	28	0.170	21	0.053
Mean	0.070		0.132		0.148		0.69

*Overflow (malfunctioning SV sensor)

This new design was assembled and evaluated by taking the measurement of all the SV sensors in the chip in the electrical transport characterization setup. But before starting the measurement of all the SV sensors, it was made a few measurements of the SV sensor that is in the middle of one of the middle columns, in this case the SV 11, by rotating the screw and consequently adjusting the PM position, until having the Hf value closest to 0. After having a Hf value less than 0.1 Oe the PM position was locked and the whole chip characterization was done (figure 6.5).
As it's shown in figure 6.5 the problems identified in the previous design were corrected. The symmetry in the chip is now seen by the results as the 1st and 4th columns and the 2nd and 3rd have similar curves and the Hf values are centered with the zero-magnetic field.
These results show the best alignment possible between the chip and the PM.
With this chip design, these are the best results possible, here we can see that this PM positioning makes the sensitivity values decrease by approximately half the original values in the 2nd and 3rd columns and nearly one fourth in the 1st and 4th columns (table 6.5), as explained before, due to the PM longitudinal fields.
As for the Hf values, the correction of the intrinsic SV sensor's Hf values was performed and the best alignment to the zero field was achieved by the calibration option offered by the sliding PM (table 6.3).
Even though this design may work, the increase in sensitivity and a decrease of the standard deviation of the Hf values are objectives that are easy to improve and can considerably improve the uniformity and the amplitude of the signal.
Both these features are improved by the decreasing in the magnetic gradient in the x direction for the sensitivity and in the y direction for the Hf. With this said there are 2 ways of doing that without adding any more components, the first is to approximate the sensors from each other, the second is to use a larger PM (same thickness), never forgetting the Hz field necessary to fully magnetize the MP.

Spin Valve sensors evaluation

As was discussed before the size of the SV sensors will define their characteristics and as such a study of the varied sizes was made.
The fabrication of a chip with a matrix of SV sensors ranging from 10 to 200 µm length and from 1 to 5 µm width was fabricated by Alexandre Chicharo a PhD student from INL in collaboration with INESC-MN.

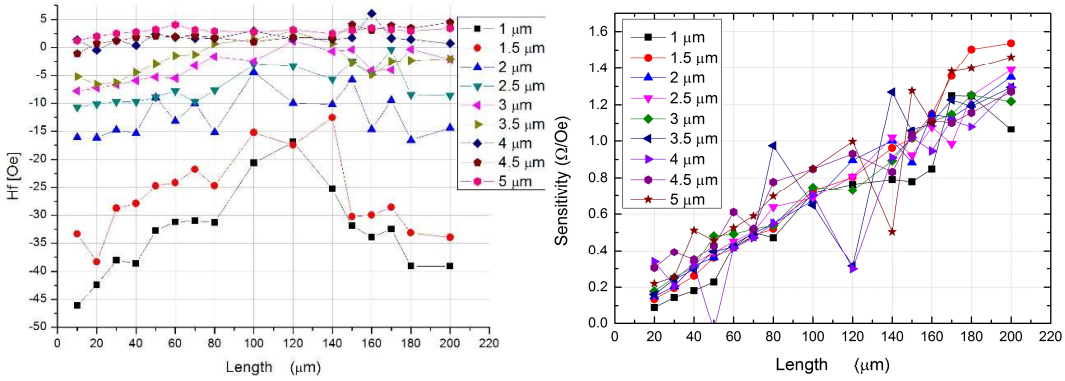

Figure 6.6 - Graphs of the Hf (left) and the sensitivity (right) values corresponding to the SV sensors varied sizes. Where the x axis is the SV length and the legend the SV width.

Using this chip, the measurement in the electrical transport setup and the data processing was made in order to see the changes in MR, sensitivity, Hf and Hc with bias currents from -3 to 3 mA in increments of 1 mA.

Since the objective of this thesis is to improve the number of operational sensors for the already establish setup only the results of the characteristics affected by the magnet's field with 1 mA of bias current are presented.
The smaller the width of the SV the more negative it's Hf values are and that the length of the SV only have significant effects for width values smaller than 3.5 µm since as we can see the 4, 4.5 and 5 µm width values have their values restricted between the Hf values of 0 and 5 Oe as the others can vary tens of Oe.
As for the sensitivity, its straightforward that the length dimension of the SV is the predominant factor for its increase, as the length goes up the sensitivity follows the tendency.
Since we were already using 100x4 μm^2 sized sensors and as we saw these ones have an Hf close to 0 and a good enough sensitivity, the sensor size was maintained.

7 - Acquisition setup

There were several acquisition setups for the previous versions of the cytometer module but with separated filtering and amplification modules and reading of one sensor at a time [32]. In 2014, Tiago Costa from INESC-ID design a multi-channel PCB for his PhD thesis [58]. This new acquisition board was designed for the parallel reading of the signals of 15 channels, applying them an amplification of 5000x and filtering them with a 300 Hz high-pass filter and a 10 kHz low-pass filter. Also, the bias current for each channel was designed programable to be able to deliver from 0.25 mA to 2 mA [59]. The board is powered by 8 1.5 V batteries.

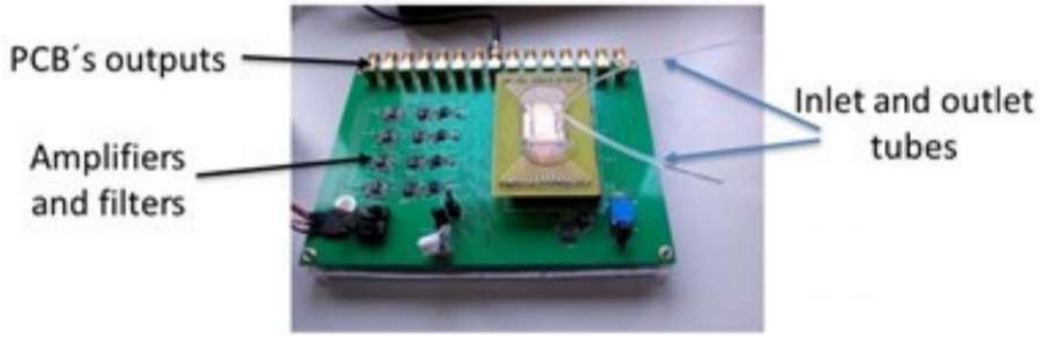

Figure 7.1 - Multi-channel acquisition board with cytometer module plugged [56].

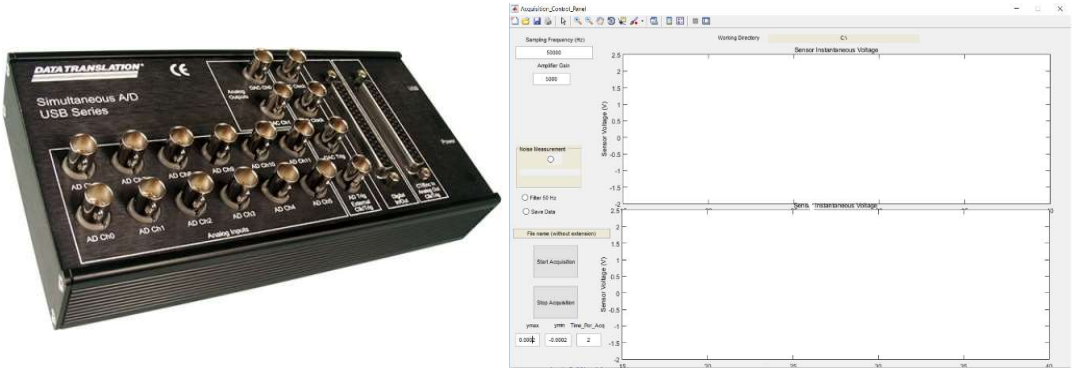

Figure 7.2 - Data Translation DT9836-12-2-BNC board (left) and graphic user interface (GUI) of the acquisition software designed in MatLab (right).

The acquisition setup is complete when the cytometer module is inserted in the acquisition board which will be connected to the 16 bit analog-to-digital converter (ADC) by a coaxial cable and then plugged by USB to a PC which will receive the data by a software designed in MatLab.
The ADC used is a Data Translation DT9836-12-2-BNC board with 12 input channels and an acquisition rate up to 225 kHz [60].
The acquisition software is designed in MatLab and was set to have an acquisition rate of 50 kHz and to divide the acquired signal by the gain (5000x) to present the real sensed values.
As its seen in figure 7.2 (right) the software has a graphic user interface (GUI) in which it's possible to change the sampling frequency, adjust the gain divided to the sensed values, noise measurement, 50 Hz filter and save option tick boxes, file name space, start and stop buttons and graph axis limits setting.
The software has implemented an optional 50 Hz notch filter and as output it gives 2 columns in which the first is filtered by a 10 kHz low-pass filter and to the second a 4 kHz low-pass filter is applied with the objective of real time noise characterization. Both graphs are presented in the GUI in real time. The software creates a .txt file in the defined directory for further analysis.

Figure 7.3 - New Era NE-1000 Series programmable syringe pump used for the flow regulation.

For a measurement to be done the last equipment needed in the setup is the syringe pump which together with a 2 ml syringe will regulate the flow rate entering the microfluidic channel. To use the pump is necessary to define the internal diameter of the syringe and the flow rate. Then a tube is connected from the syringe to the inlet and other from the outlet to a reservoir. Press start in the pump and in the software and the measurement has begun.
Unfortunately, the acquisition board was inoperative. After several testing measurements, the attempts to find the problem were ineffective. For a short period of time a colleague from INESC-ID made the board operational but without any hardware filtering. The only particle measurements that could be done were during this time.

8 - New chip cytometer

As demonstrated, the most effective design until now for the cytometer counting module is the one described in chapter 6. With that design, the proximity of the PM to the SV sensors and consequently to the microfluidic channels and MPs is sufficiently small to have a Hz field strong enough to magnetize the MPs. Also, the micromachined holes made in the PCB and in the PMMA alignment system allow for the perfect PM-chip alignment. This together with the adjustment of the y positioning of the PM performed by the rotation of the screw and consequent sliding of the PM make this design the one with more operational sensors and with symmetrical and centered transfer curves.
Even though these results are better, there are still SV sensors that aren't in the best performance possible since the first and last sensor of each column have high module of Hf field and the 1st and 4th columns have low sensitivities.
In hope of improving these results a new chip design was made (figure 8.1).

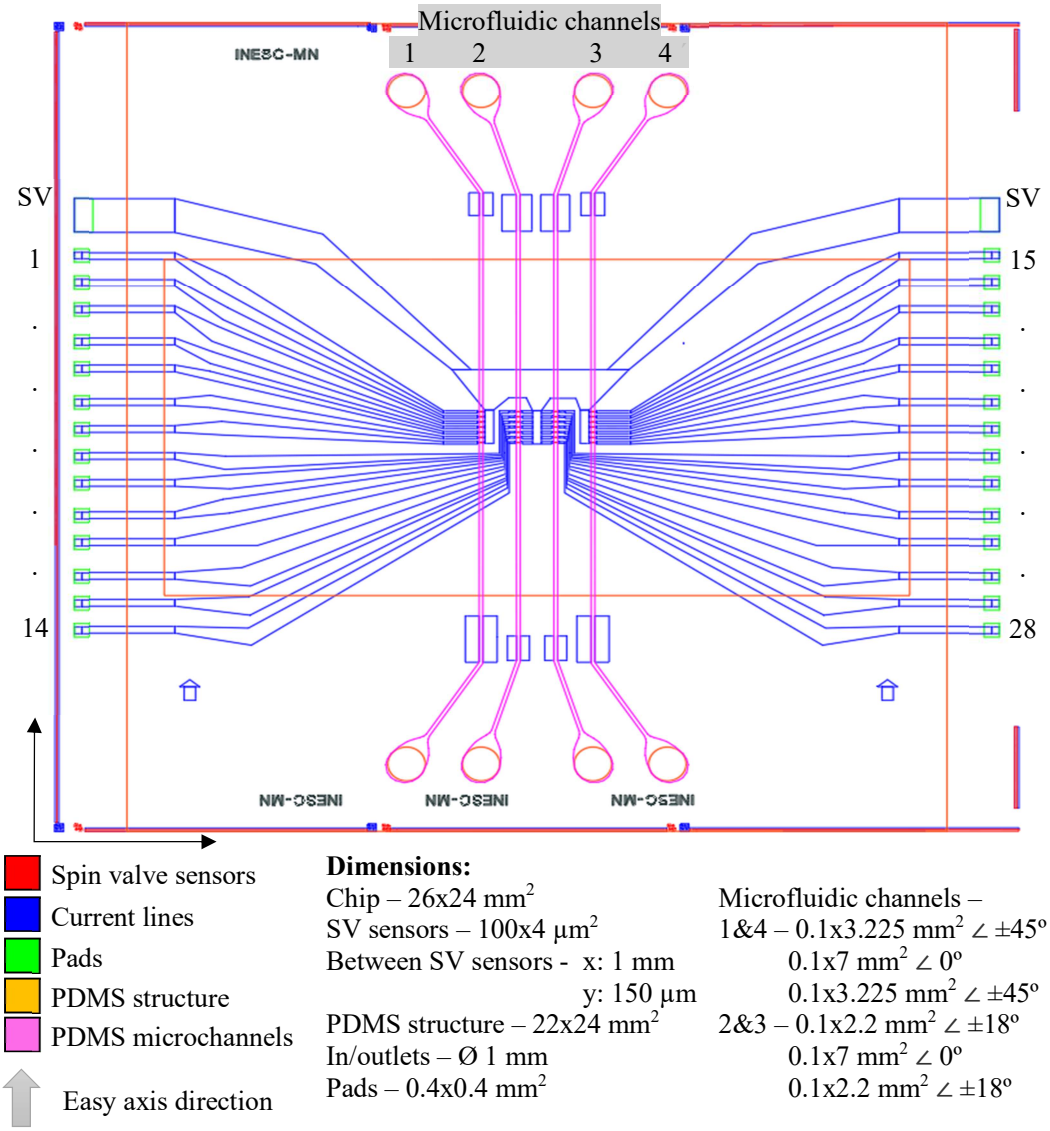

Figure 8.1 - AutoCad draw of the new design of the biochip for the counting module of the cytometer and respective dimensions.

The first and more intuitive change is to reduce the distance between channels by approximating them towards the center of the chip either in the x and the y axis. By reducing their distance to the center in the x axis the influence of the PM's longitudinal fields is reduced and with it the increase of the sensors sensitivity. By reducing the channels distance from 3 mm, in the previous design, to 1 mm, the 1st and 4th columns will have the same sensitivity as the 2nd and the 3rd in the previous design which means an even better sensitivity in these same columns in this new design. The y axis centering of the SV matrix was made to have the SV sensors and the PM at the same distance either from the inlets and the outlets. As was described before, the reduction of distance between columns only improves the sensors sensitivity, which means that to have all the sensors operational some changes need to be done to improve the Hf field of the SV's in the top and bottom of the column.

In a first approach, it was though that the placement of current carrying wires parallel to the sensors length could generate a field strong enough to correct the transversal fields of the PM. The simplest way was to draw the same PCB but adding 2 current lines in the bottom face, both parallel to the length of the SVs but one close to the top sensor and one close to the bottom sensor with the current passing in opposite directions to create the field against each other to cancel the outwards fields of the PM.

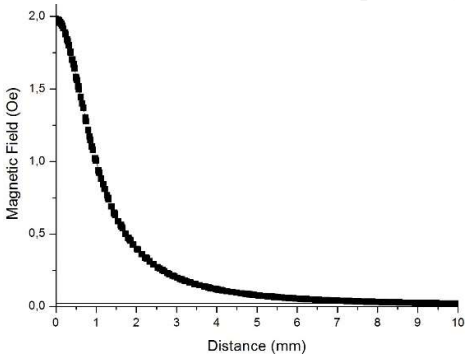

Figure 8.2 - Magnetic field created from the middle of a wire of 75x17 µm^2 cross section with a 1 A current.

Using COMSOL "Magnetic Fields" module a rectangular wire was simulated. According to Ampere's law the field gradient is proportional to the current density and as such proportionally inverse to the wire cross section. With this in mind, the first simulation was a wire with 20 mm length, 17 µm thickness and 75 µm width which are the minimum dimensions of cross section that the supplier can produce. Defining the geometry as a "Single-Turn Coil" and a current of 1 A the results showed (figure 8.2) a maximum field of 2 Oe which is one order of magnitude bellow the needed value. Since the cross section of the simulated wire is very small the 1 A current becomes a high current that may create high temperatures and damage the setup. With these conditions, the minimum current needed was a 10 A current. This means that the current carrying wires in the PCB aren't a good solution.

The second idea to correct the Hf field was to add a secondary PM above the PDMS which should, due to the attraction forces, make the field lines between the PM more perpendicular to their planes and thus

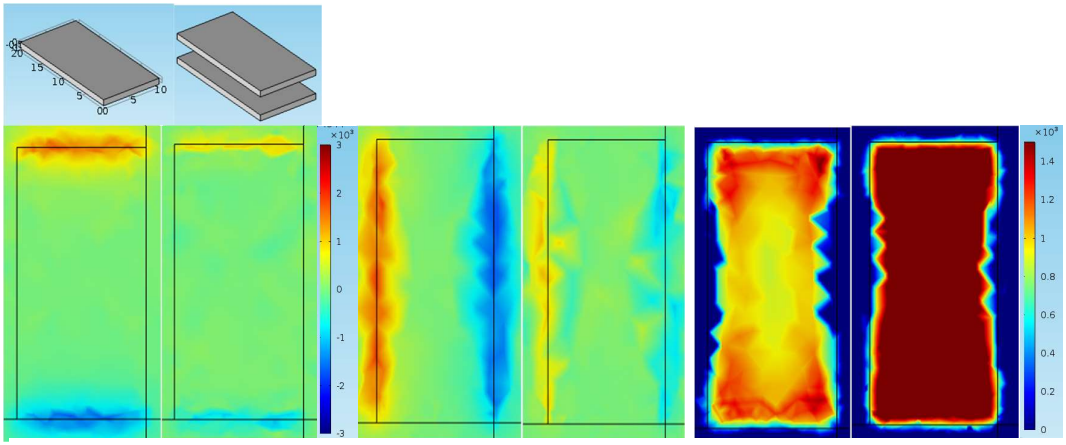

Figure 8.3 - Simulation results of the Hx (left), Hy (middle) and Hz (right) components of the magnetic field created by 1 PM at 1 mm high (left in each component) versus the magnetic field created by 1 PM at 1 mm high and an equal PM 3 mm above (right in each component). In the Hx and Hy components the color range is from -3 kOe to 3 kOe and the Hz is from 0 to 1.5 kOe.

reduce the Hx and Hy gradient. To confirm this idea other COMSOL simulation was made. Using the same conditions and parameters as in the simulation of a single PM (chapter 5) it was added a second and equal PM above to see the effect in the field sensed by the SVs.
The results shown in figure 8.3 correspond to the 3 components of the magnetic field sensed at 1 mm (PCB and silicon substrate) from the bottom PM and 3 mm (PDMS) from the top PM which means that this field is the one sensed in the SVs plane.
This confirms the expectations that the 2 PM setup can reduce the Hx and Hy components while the Hz component is amplified.
From these results, we can have certainty that the 2 PM setup will assure the full magnetization of the MPs since as the figure 8.3 (right) shows, while the 1 PM setup has the center of the PM with a ≈1 kOe field, the 2 PM setup presents almost the full area of the PM with a field of 1.5 kOe or greater since the color range limit is set.
When comparing the Hx and Hy components of the 1 PM setup versus the 2 PM setup we can instantly see that the borders of the PM in each component measurement have their intensity reduced. Still, when looking closer it is possible to see that even though the border spots have less intensity some spots of blue (negative field) and orange (positive field) appear closer to the middle of the PM. This may be due to the difference of distance between the bottom and top PM from the plane where the measurement was taken or due to lack of magnetic homogeneity of the PMs.
But, if this hypothesis is to be discredited one needs to try to build such setup.
Starting from the setup that works, the 1 PM setup, one may just define in the PDMS the place where the middle of the PDMS meets the middle of the SV matrix and create a cavity to lock the top PM above that location and then just measure the SVs and adjusting the PM bellow, by rotating the screw, until the expected result appears. This was the idea at the time of the new chip design and that's why the orange rectangle appears over the SVs (figure 8.1) being a cavity of 1 mm (PM thickness) in the top part of the PDMS between the inlets and outlets.
As this was not possible to prove due to setbacks some doubts arouse.
Firstly, the intrinsic Hf field of the SV may be a problem since the top magnet is aligned by the position of the SVs and even the movement of the bottom PM may not correct this positioning and secondly, the difference in distance from the bottom and top PM to the SV's plane may be a setback since in theory the plane where the magnetic field is more perpendicular is the one right in the middle of both PMs.
Also in the new design, changes in the microfluidic channels needed to be made. The moving of the SV sensors closer to the center made mandatory the approximation of the channels since they must be right in top and parallel to the SVs width. This reduction in proximity made the borders of the inlets and outlets of the channels to overlap and thus impossible to fabricate.
The first approach for changing the microfluidic channels of the previous configuration was to move the 1st slightly up in the y direction and the next slightly down and so on so they wouldn't overlap, but as the distance from the in/outlet border to the next channel border would be just 0.5 mm it was thought that the PDMS structure integrity would be fragilized and therefore a different approach was taken.
Thinking in the previous statement, the first condition established for the design of the new channels was that the channels in/outlet borders needed to be separated by at least 1 mm which means that the channels would not be just along the y axis and that some kind on angle needed to be implemented. The second condition was that the part of the channel parallel to the y axis should be as great as can be without having to have accentuated angles to meet the in/outlets.
To encounter these conditions firstly it was drawn the straight channels with 7 mm, then it was defined that in the exterior channels the angle from the in/outlet to the straight channel would be 45º from the y axis and finally that the exterior and the interior in/outlets should be 1 mm apart.

This made the exterior channels to be 2.557 mm long in the 45º part, 7 mm in the straight part and again 2.557 mm at 135º and the interior channels to be 2.187 mm long in the 18º part, 7 mm in the straight part and also 2.187 mm at 162º to get to the outlet.
To be sure that these modifications wouldn't change the velocity and consequently the frequency requirements establish by the flow rate another simulation in COMSOL was made using the parameters of the old channels (chapter 5) but altering the geometry for the new ones.

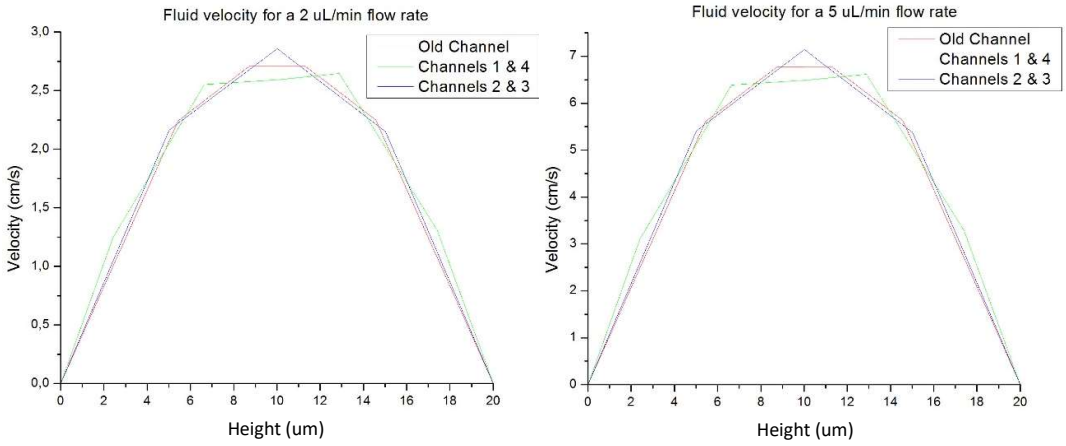

Figure 8.4 - Results of the simulation of the fluid velocity of the new channels against the old ones at the flow rates of 2 and 5 µL/min.

Since, as demonstrated before (chapter 5), the flow rates that can be used in the existing acquisition setup are the 2 and 5 µL/min, only these were simulated. As the results (figure 8.4) show the alterations in the channel's geometry don't generate significant changes in the fluid's velocity in either flow rate.
All these changes in the chip design and in the microfluidics made obligatory to increase size of the chip and the PDMS structure. In the y axis, the growth was due to the size of the new microfluidic channels which made both the chip and the PDMS structure to be 24 mm long. By having the same size, when the time comes for the alignment between the chip and the PDMS structure it will be easy since this direction can be locked in the micro alignment system (figure) and it will be only needed to slide the PDMS in the x axis to align the channels with the SVs. As for the x axis, the widening was done for the placement of the cavity for the positioning of the PM above the PDMS which obligated the PDMS to grow to 22 mm and the chip to 26 mm to avoid the covering of the SV pads by the PDMS.

New chip cytometer characterization

The new chip cytometer was fabricated by following the steps of the "run sheet for magnetic counter fabrication process" presented in Annex I. After the fabrication of a sample in which 4 chips were fitted, these 4 were characterized in the electrical characterization setup.

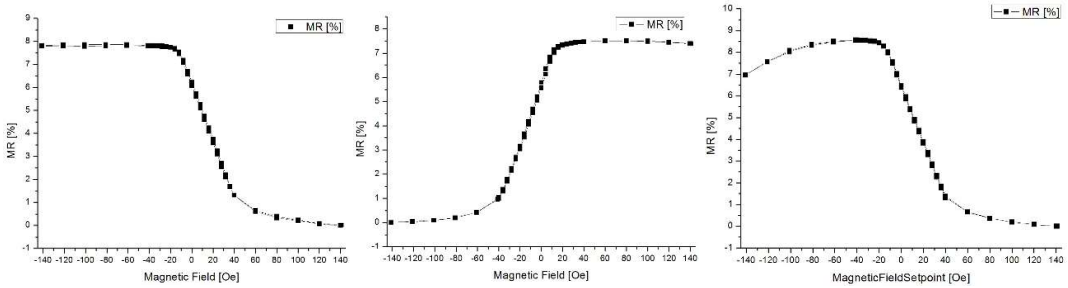

Figure 8.5 – The 3 different types of curves resulting from the characterization of all samples. The normal and expected transfer curve (left), the inverted curve presented in some sensors in all samples (middle) and one in which the saturation state isn't in the lowest field presented in the 4th sample (right).

As its possible to see in figure 8.6 and in annex III none of the SV 16 sensors is operational, this is due to a mistake in the AutoCad design where the connection between the SV and the aluminum current lines was drawn as a line instead of a polyline. Since the DWL 2.0 can't read lines the pattern wasn't transferred to the PR and when the lift-off was done the SV 16 was not connected.

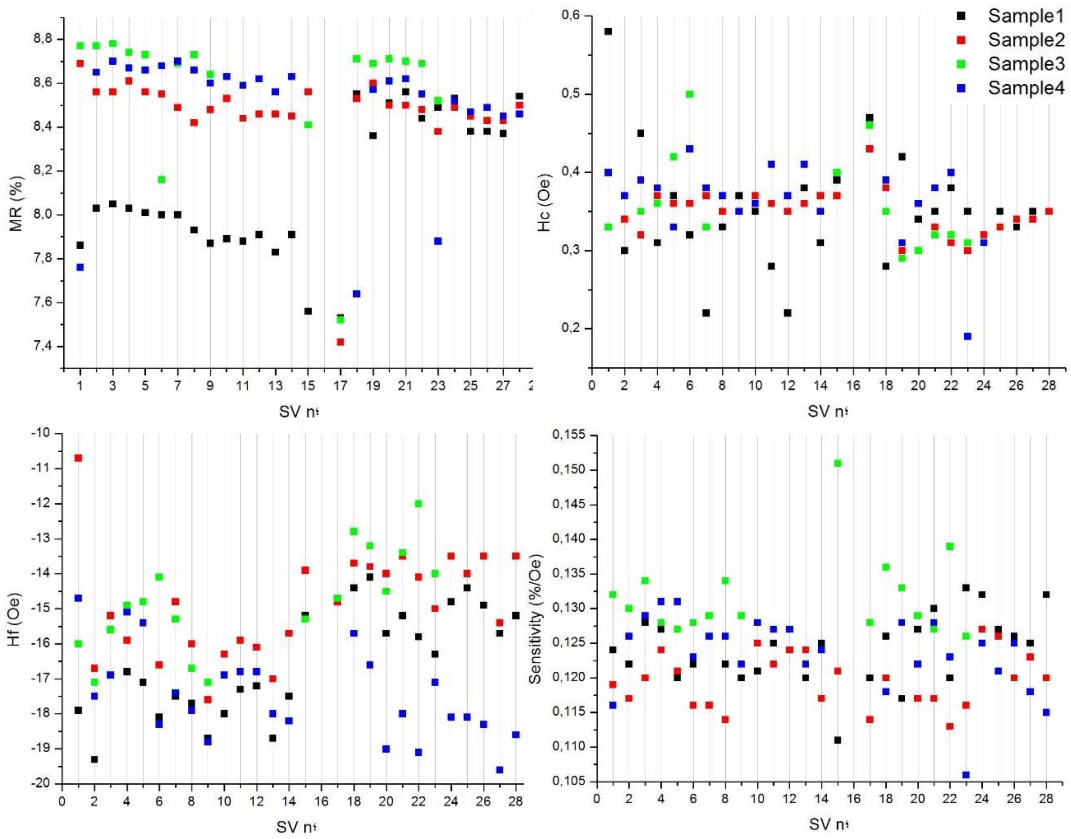

Figure 8.6 – Graph of the new chip SV sensors MR, coercive field, offset field and sensitivity.

Also, but this time by a machine error, the DWL 2.0 drew a line along the 3rd sample and another on half of the 4th sample. These lines passed over the aluminum current lines which means that after the lift-off the current lines were cut making the bottom half of the 3rd sample (SV 10 to 14 and 24 to 28) and some of the 4th (SV 15 to 17) inoperative.
As for the rest of the samples and sensors the normal transfer curve is the one shown in figure 8.5 (left).

Table 8.1 - Descriptive statistics of the new chip SV sensors MR, minimum resistance, maximum resistance, coercive field, offset field and sensitivity.

Characteristics	Sample 1		Sample 2		Sample 3		Sample 4	
	Mean	SD	Mean	SD	Mean	SD	Mean	SD
MR (%)	8.12	0.31	8.46	0.22	8.58	0.32	8.49	0.29
R min (Ω)	611.59	35.73	590.07	20.26	600.23	19.84	641.40	14.32
R max (Ω)	661.07	37.19	640.03	21.84	651.82	21.91	695.88	15.27
Hc (Oe)	0.35	0.07	0.35	0.02	0.36	0.06	0.73	1.15
Hf (Oe)	-16.48	1.51	-14.91	1.48	-14.79	1.47	-17.48	1.27
Sensitivity (%/ Oe)	0.124	0.005	0.120	0.004	0.132	0.006	0.124	0.006

The transfer curve shown in figure 8.5 (middle) has the maximum resistance in the high field situation in contrary to the normal one and only happens on the SV 17 in all samples, on the SV 15 and SV 6 in sample 3 and on the SV 6 of sample 4.
In figure 8.5 (right) is presented a curve that for the lower magnetic fields should be saturated which is not the case and happens in all sensors of sample 4. This problem may be originated by a bad alignment in the annealing process which may have caused a deviance in the pinned layer. Also in this sample, the last 5 sensors (SV 24 to 28) have a coercive field (Hc) higher than 1 Oe which may originate from the same problem. Repeating the annealing process may correct this problem.
Table 8.1 presents the mean values and standard deviations of the sensor's main characteristics and shows that with this stack the SVs present a better MR value than with the stack used in the previous chips which means a greater variation in resistance and consequently a greater amplitude of the signal.
As for the Hf, the results are comparable with the old chips but unfortunately the sensitivity values drop to half of the old chips which will reduce the influence of the high MR values.
Since this was the first contact with microfabrication processes, some of the machines were having problems and redundant processes were used, the repetitions of the fabrication process should be done in order to be sure that these are the real characteristics of a precise and well fabricated SV with this stack.

9 - Conclusion

The development of a flow cytometer based on magnetoresistive sensors to be used as a POC equipment can only be done as modular machine that needs to integrate 3 LOC's (sample preparation, separation and counting) and an electronics board to control them and process the outputs. To create these modules, one needs to combine different areas of knowledge like materials engineering, magnetics, microfluidics, MEMS, electronics and programing.

This very demanding project deserves all the attention it can get since the advantages given by its accomplishment can improve the swiftness of the diagnosis and consequent treatment of diseases by being portable and permitting rapid *in situ* analysis, its price can reach a greater part of the world's population and have a smaller environmental impact since it uses less energy and less potential pollutant reagents.

The continuous evolution of semiconductors and microfluidics technology will cause an increasing integration of LOC devices in the next generation of laboratory medical equipment.

A LOC device is a set of integrated microsystems with different functionalities and just by being small they get a set of advantages as:

- Portability, which allow them to be POC devices;
- Short diffusing times, reducing analysis times improving POC;
- Use small volumes, traducing in less reagents which means less waste and lower prices and,
- Allow for lower currents needing less storage energy becoming a safer platform.

Also, these microsystems can be mass fabricated which will again reduce the price, but most importantly in a POC device it needs a well-designed software for a user-friendly interface so that the results can be understood by anyone.

Several novel manipulation, separation and detection mechanisms based on magnetic methods are continuously emerging but much more research must be performed in order to put in the market a fully magnetic POC flow cytometer with all these characteristics where everyone can use it in a simple way. An equipment with these features will probably replace the current optical and fluorescence detection technologies maintaining the high sensitivity and fast readout time.

This work describes the optimization of LOC counting module for the development of a magnetic flow cytometer. After a separation module, the cells or MPs will be distributed in different parallel microfluidic channels which are integrated with corresponding SV sensors columns. But for these measurements to be made an external magnetic field imposed by an PM must be well positioned in order not to influence the SV response.

To understand how the MPs affect the SV response, it was simulated the response of 3 different MPs (300 nm, 420 nm and 2800 nm) that would pass in the different microfluidic channels and how their signal would change in respect to their position. Simulations indicated that the closest to the SV sensors the higher the amplitude of the signal's peaks and that it decreases in an exponential way as we get away from the sensor. So, by measuring the amplitude of the signal we can infer the position of the MP inside the channel.

As their velocity will also change the signal's characteristics, the simulation of the microfluidic channels was made. The velocity establishment in the channels is made by the inflow setting in the syringe pump and as such the simulation was made for different inflow rates. As was expected the results were a parabolic velocity profile with the maximum velocity in the middle of the channel's height and 0 at the extremities. But, in this work the velocity is limited by the acquisition board since it is limited to a 50 kHz sampling rate which led to conclude that with this setup the maximum velocity is 10 cm/s which corresponds to a maximum inflow rate of 7.4 μL/min.

After characterizing the signal's change in relation to the LOC geometries (channels and SVs) and to the velocity profile assuming a constant magnetization, one needed to assure that such magnetization was applied but without affecting the SV's response which was the main concern in this thesis.
Several simulations of the magnetic field created by different neodymium PM were done to understand which would have a perpendicular field strong enough to fully magnetize the MP and the largest area where the transversal and longitudinal fields would be smaller than 10 Oe, the area where the sensors could be placed without being affected. The largest this area, the more channels can be created.
These simulations led to conclude that the reduction of the PM's thickness would greatly enlarge this area while reducing the perpendicular field in a softer way and that using a 20 mm x 10 mm x 1 mm PM the closest as possible to the sensors we would get the best results within the available PMs.
Knowing the PM to use, it was tried to integrate the PM with the SV chip in diverse ways which led to realize that a precise positioning and alignment of the PM in relation to the SVs is of the outmost importance. To do this, firstly the chip was aligned in a PCB pocket (to reduce distance from the PM) and secondly it was fabricated a PMMA support, also aligned with the PCB, which with the assistance of a 0.5 mm pitch screw will align the desirable area of the PM exactly below the SV matrix.
Whereas in the beginning only 2 or 3 SVs had correct transfer curves, with this new setup it is assured the magnetization of the MPs while having all the SV sensors with centered and symmetrical transfer curves.
Still some alterations need to be done since as the SVs get away from the center of the PM the longitudinal fields will decrease their sensitivity and the transverse fields will shift the transfer curves.
Finally, to try to correct this a new chip was designed and fabricated where the SV columns were approximated towards the center of the chip which in theory will assuredly increase the sensors sensitivity and allow the addition of more parallel channels.
But, after all the knowledge apprehended in the realization of this thesis maybe one could have solved these problems in different ways.
Not discrediting the information presented here, since as it was demonstrated the comprehension of the effect of the PM components and its positioning should be taken in account in future research, as well as the microfluidic relation to the electronic setup.
But, the use of a larger PM with the same thickness would also enlarge the desirable area and this way augment the number of parallel channels that could be integrated. In a different manner, if it is decided to use a 2 PM setup (one in top of the other) the alignment system should slide both the PMs at same time, maintaining the alignment between both, and the SVs should be at the same distance from the top and bottom one.
Relatively to the SV positioning in the chip, as we can see in figure 5.4, for a channel with 20 µm height the width of the signal is less than 50 µm which means that in each column the sensors could be more closely together which would reduce the shift in the transfer curve.
Since the values retrieved from the new chip characterization weren't the expected and some errors occurred during its fabrication, the fabrication of the new chip should be repeated in hopes of getting SVs with lower Hf and higher sensitivity.
The preoccupation of having all the SV sensors in a column centered should not be that great since there is no need for 6 redundant sensors and even if the velocity is to be measured only 2 sensors are needed. As such, one could add another sensor in a non-measurement area to serve as a reference sensor.
Using a Wheatstone bridge, a differential IC or a software correction the addition of a reference sensor would be of great value, since in the experimental measurements made, just the fact of having the syringe pump in the same table as the LOC would create noise coming from the pump's motor vibrations, any small shock against the table would also create a signal variations similar to the expected signal and obviously the unavoidable environmental background generated by the electromagnetic interference and Joule effect. All these noise sources could be minimized using a reference sensor.

One other subject that should be studied and evaluated is the introduction of hydrodynamic focusing since it will relate in a tradeoff manner with the complexity of output processing software. On one hand, it is possible to use a 3D hydrodynamic focusing, like the one used in Zhao and you [11] paper, which will increase the LOC complexity but make the MPs to flow in an established height and width inside the channel, what will obligate the particles to pass 1 by 1, producing uniform peaks (amplitude and frequency) and make each peak related to one MP. This way, the detection can be made simply by using an operational amplifier in a comparator design and a counter not needing more than a few lines of code. On the other hand, it can be done without hydrodynamic focusing which makes possible that the MPs be at different heights (different amplitudes), different speeds (different frequency) and can be in top or side by side of each other needing a software that evaluate the different amplitudes and several convolutions to be able of identifying if it is a single MP or a set of them or if it is away or closer to the sensor which may also be necessary to extrapolate values, meaning a complex software. In between these options, it is possible to do just vertical or horizontal focusing what would create the balance between the complexity of the setup and the complexity of the software.

Another microfluidic problem encountered is the agglomeration of MPs at the channel's inlet and sometimes the channels clogging which may originate from both the PM's magnetic gradient and the inlet geometry. An inlet with a greater entering angle or the making of a curve may reduce these effects. Also, higher flow rates may reduce the MPs agglomeration.

In terms of electronics and coding, it is possible to replace both the computer and the bulky ADC by a prototyping board (ex. Arduino, Raspberry Pi) which would have the same or better performance and would make the electronics part of the counting module portable and fully battery powered.

At this moment, since the proof-of-concept is already a reality, the next advances in the prototype should be considering a medical application since all the geometries and consequent variables need to be chosen according to the characteristics of the labeled target analyte.

References

[1] Clark Jr., L. C., Wolf, R., Granger, D., Taylor, Z. (1953). Continuous Recording of Blood Oxygen Tensions by Polarography. Journal of Applied Physiology, 6 (3), 189-93.

[2] Sharma, S., Zapatero-Rodríguez, J., Estrela, P., O'Kennedy, R. (2015). Point-of-Care Diagnostics in Low Resource Settings: Present Status and Future Role of Microfluidics. Biosensors, 5, 577-601.

[3] Chin, C. D., Chin, S. Y., Laksanasopin, T., Sia, S. K. (2013). Chapter 1 - Low-Cost Microdevices for Point-of-Care Testing. Point-of-Care Diagnostics on a Chip, 3-21. Springer. Berlin.

[4] Rahman, M. (2006). Introduction to Flow Cytometry. Accessed in: 3 of May of 2015, in: http://www.ufjf.br/imunologia/files/2010/03/Flow-Cytometry-introduction.pdf.

[5] Brown, M., Wittwer, C. (2000). Flow Cytometry: Principles and Clinical Applications in Hematology. Clinical Chemistry, 46:8(B), 1221–1229.

[6] Huh, D., Gu, W., Kamotani, Y., Grotberg, J. B., Takayama, S. (2005). Microfluidics for flow cytometric analysis of cells and particles. Physiological Measurement, 26, R73–R98.

[7] Gerdts, G., Luedke, G. (2006). FISH and chips: Marine bacterial communities analyzed by flow cytometry based on microfluidics. Journal of Microbiological Methods, 64, 232–240.

[8] Takao, M., Takeda, K. (2011). Enumeration, Characterization, and Collection of Intact Circulating Tumor Cells by Cross Contamination-Free Flow Cytometry. Cytometry Part A, 79A, 107-117.

[9] Kovarik, M. L., Gach, P. C., Ornoff, D. M., Wang, Y., Balowski, J., Farrag, L., Allbritton, N. L. (2012). Micro Total Analysis Systems for Cell Biology and Biochemical Assays. Analytical Chemistry, 84(2), 516–540.

[10] Boyle, D. S., Hawkins, K. R., Steele, M. S., Singhal, M., Cheng, X. (2012). Emerging technologies for point-of-care CD4 T-lymphocyte counting. Trends in Biotechnology, 30(1), 45-54.

[11] Zhao, J., You, Z. (2016). A Microflow Cytometer with a Rectangular Quasi-Flat-Top Laser Spot. Sensors, 16 (9), 1474.

[12] McKenna, B. K., Evans, J. G., Cheung, M. C., Ehrlich, D. J. (2011). A parallel microfluidic flow cytometer for high-content screening. Nature Methods, 8 (5), 401-3.

[13] Martini, J., Recht, M. I., Huck, M., Bern, M. W., Johnson, N. M., Kiesel, P. (2012). Time encoded multicolor fluorescence detection in a microfluidic flow cytometer. Lab on a Chip, 12, 5057-5062.

[14] Akinfieva, O., Nabiev, I., Sukhanova, A. (2013). New directions in quantum dot-based cytometry detection of cancer serum markers and tumor cells. Critical Reviews in Oncology/Hematology, 86, 1–14.

[15] Lin, S., Lin, C. (2016). Chip-Based Cytometry Illuminated by a Blade-Shape Continuous Light for Multispectral Detection. Applied Sciences, 6 (8), 229.

[16] Chen, J., Xue, C., Zhao, Y., Chen, D., Wu, M., Wang, J. (2015). Microfluidic Impedance Flow Cytometry Enabling High-Throughput Single-Cell Electrical Property Characterization. International Journal of Molecular Sciences, 16, 9804-9830.

[17] Kriz, C. B., Radevik, K., Kriz, D. (1996). Magnetic permeability measurements in bioanalysis and biosensors. Analytical Chemistry, 68(11),1966–1970.

[18] Baselt, D. R., Lee, G. U., Colton, R. J. (1996). Biosensor based on force microscope technology. Journal of Vacuum Science & Technology B, 14(2), 789–793.

[19] Baselt, D. R., Lee, G. U., Natesan, M., Metzger, S. W., Sheehan, P. E., Colton, R. J. (1998). A biosensor based on magnetoresistance technology. Biosensors and Bioelectronics, 13, 731–739.

[20] Llandro, J., Palfreyman, J. J., Ionescu, A. (2010). Magnetic biosensor technologies for medical applications: a review. Medical & Biological Engineering & Computing, 48, 977–998.

[21] Golden, J. P., Verbarg, J., Howell Jr., P. B., Shriver-Lake, L. C., Ligler, F. S. (2013). Automated processing integrated with a microflow cytometer for pathogen detection in clinical matrices. Biosensors and Bioelectronics, 40, 10–16.

[22] Maleki, T., Fricke, T., Quesenberry, J. T., Todd, P., Leary, J. F. (2012). Point-of-care, portable microfluidic blood analyzer system. Proc. SPIE 8251, Microfluidics, BioMEMS, and Medical Microsystems X, 82510C (February 9).

[23] Germano, J., Martins, V. C., Cardoso, F. A., Almeida, T. M., Sousa, L., Freitas, P. P., Piedade, M. S. (2009). A Portable and Autonomous Magnetic Detection Platform for Biosensing. Sensors, 9, 4119-4137.

[24] Loureiro, J., Ferreira, R., Cardoso, S., Freitas, P. P., Germano, J., Fermon, C., Arrias, G., Pannetier-Lecoeur, M., Rivadulla, F., Rivas, J. (2009). Toward a magnetoresistive chip cytometer: Integrated detection of magnetic beads flowing at cm/s velocities in microfluidic channels. Applied Physics Letters, 95, 034104.

[25] Loureiro, J., Andrade, P. Z., Cardoso, S., da Silva, C. L., Cabral, J. M., Freitas, P. P. (2011). Magnetoresistive chip cytometer. Lab on a Chip, 11, 2255.

[26] Fernandes, A. C., Duarte, C. M., Cardoso, F. A., Bexiga, R., Cardoso, S., Freitas, P. P. (2014). Lab-on-Chip Cytometry Based on Magnetoresistive Sensors for Bacteria Detection in Milk. Sensors, 14, 15496-15524.

[27] Chicharo, A., Cardoso, F., Cardoso, S., Freitas, P. J. P. (2015). Real-Time Monitoring of Magnetic Nanoparticles Diffusion in Lateral Flow Microporous Membrane Using Spin Valve Sensors. IEEE Transactions on Magnetics, 51 (1), 1-4.

[28] Loureiro, J., Ferreira, R., Cardoso, S., Germano, J., Snakenborg, D., Cabral, J. M. S., Freitas, P. P. (2008). Spintronic device for cell/magnetic particle sorting and counting. Twelfth International Conference on Miniaturized Systems for Chemistry and Life Sciences (October 12 - 16).

[29] Helou, M., Reisbeck, M., Tedde, S. F., Richter, L., Bär, L., Bosch, J. J., Stauber, R. H., Quandt, E., Hayden, O. (2013). Time-of-flight magnetic flow cytometry in whole blood with integrated sample preparation. Lab on a Chip, 13 (6), 1035-8.

[30] Melzer, M., Karnaushenko, D., Makarov, D., Baraban, L., Calvimontes, A., Mönch, I., Kaltofen, R., Meid, Y., Schmidtab, O. G. (2012). Elastic magnetic sensor with isotropic sensitivity for in-flow detection of magnetic objects. RSC Advances, 2, 2284-2288.

[31] Cambridge University. (2008). Ferromagnetic Materials. Accessed in: 3 of January of 2017. In: https://www.doitpoms.ac.uk/tlplib/ferromagnetic/index.php.

[32] Loureiro, J. F. Q. (2011). Lab on Chip microsystem for flow cytometric analysis, separation and counting of cells and particles. Doctoral Thesis. Instituto Superior Tecnico, Lisboa.

[33] Millen, R. L. (2005). Giant magnetoresistive sensors and magnetic labels for chip-scale detection of immunosorbent assays. Doctoral Thesis. Iowa State University, Ames, Iowa.

[34] Chícharo, J. A. N. (2012). Spintronic Lateral Flow Biochip Platform. Masters Thesis. Instituto Superior Tecnico, Lisboa.

[35] Ferreira, H. A. T. D. (2007). Magnetoresistive biochips: Detection of biomolecular recognition and On-chip transport of magnetically labeled biomolecules. Doctoral Thesis. Instituto Superior Tecnico, Lisboa.

[36] Baibich, M., Broto, J., Fert, A., van Dau, F. N., Petro, F., Eitenne, P., Creuzet, G., Friederich, A., Chazelas, J. (1988). Giant magnetoresistance of (001)Fe/(001)Cr magnetic superlattices. Physical Review Letters, 61 (21), 2472-2475.

[37] Binasch, G., Grunberg, P., Saurenbach, F., Zinn, W. (1989). Enhanced magnetoresistance in layered magnetic structures with antiferromagnetic interlayer exchange. Physical Review B, 39, 4828-4830.

[38] Dieny, B., Speriosu, V.S.. Metin, S., Parkin, S.S., Gurney, B.A., Bumgart, P., Wilhoit, D.R. (1991). Giant magnetoresistive in soft ferromagnetic multilayers. Physical Review B, 43, 1297.

[39] Cardoso, F. A. (2010). Design, optimization and integration of magnetoresistive biochips. Doctoral Thesis. Instituto Superior Tecnico, Lisboa.

[40] Atencia, J., Beebe, D. J. (2005). Controlled microfluidic interfaces. Nature, 437, 648-655.

[41] Munson, B.R., Young, D.F., Okisshi, T.H., & Huebsch, W.W. (2009). Fundamentals of fluid mechanics. John Wiley & Sons, Inc, Hoboken, New Jersey.

[42] Bruus, H. (2004). Theoretical microfluidics. Lecture notes. Department of Micro and Nanotechnology, Technical University of Denmark.

[43] Ruffert, C. (2016). Magnetic Bead—Magic Bullet. Micromachines, 7, 21.

[44] Wang, Y., Gao, Y., Wyss, H., Anderson, P., den Toonder, J. (2013). Out of the cleanroom, self-assembled magnetic artificial cilia. Lab on a Chip, 13, 3360-3366.

[45] INESC-MN. Facilities. Accessed in: 10 of February of 2017. In: https://sites.google.com/site/inescmn/home/facilities.

[46] INESC-MN. Single Level Processing. Accessed in: 12 of February of 2017. In: https://sites.google.com/site/inescmn/home/products-services/single-level-processing.

[47] Wisborg, E. B. Plasma-Enhanced Chemical Vapor Deposition (PECVD). Accessed in: 12 of February of 2017. In: http://folk.uio.no/yurig/Nanotechnology/Student_presentations/2014/Emil%20Wisborg%20-%20PECVD.pdf.

[48] Micro chem. SU-8 2000 Permanent Epoxy Negative Photoresist Datasheet. Accessed in: 31 of March of 2017. In: http://www.microchem.com/pdf/SU-82000DataSheet2025thru2075Ver4.pdf.

[49] Speliotis, D. Getting the Most From Your Vibrating Sample Magnetometer. Digital Measurement Systems Division of ADE Technologies, Inc.

[50] Dektak 3030 surface profiling measuring system. Accessed in: 13 of April of 2017. In: http://mmrc.caltech.edu/Profilometer/Dektak3030.pdf.

[51] Ademtech. Bio-Adembeads Streptavidin 0313. Accessed in: 17 of April of 2017. In: http://www.ademtech.com/images/bio-adembeads%20streptavidin%200313%20v%201.5.pdf.

[52] Invitrogen. Dynabeads® M-280 Streptavidin. Accessed in: 17 of April of 2017. In: https://tools.thermofisher.com/content/sfs/manuals/MAN0014017_Dynabeads_M280_Streptavidin_UG.pdf.

[53] Li, G., Wang, S. X. (2004). Model and Experiment of Detecting Multiple Magnetic Nanoparticles as Biomolecular Labels by Spin Valve Sensors. IEEE Transactions on Magnetics, 40 (4), 3000-2.

[54] Pyrhönen, J., Jokinen, T., Hrabovcová, V. (2008). Design of rotating electrical machines. Pag. 208. John Wiley & Sons, Inc, Hoboken, New Jersey.

[55] Supermagnete. Data sheet article Q-20-20-03-N. Accessed in: 20 of April of 2017. In: https://www.supermagnete.pt/data_sheet_Q-20-20-03-N.pdf.

[56] Duarte, C. M. P. C. (2016). Portable “lab-on-chip” platform for bovine mastitis diagnosis in raw milk. Doctoral Thesis. University of Lisbon, Lisboa.

[57] Soares, A. R. S. (2015). Portable lab-on-chip platform for bovine mastitis diagnosis in raw milk. Master Thesis. University of Lisbon, Lisboa.

[58] Costa, T. M. L. M. (2014). Integrated circuits for interfacing magnetoresistive sensors. Doctoral Thesis. Instituto Superior Tecnico, Lisboa.

[59] Duarte, C., Costa, T., Carneiro, C., Soares, R., Jitariu, A., Cardoso, S., Piedade, M., Bexiga, R., Freitas, P. (2016). Semi-Quantitative Method for Streptococci Magnetic Detection in Raw Milk. Biosensors, 6 (2), 19.

[60] Data translation. (2009). DT9836 Series user's manual. Accessed in: 10 of May of 2017. In: http://www.indextm.co.kr/upload/catalogue_file/ac56b58bde28b6dce98bc774bff83a69.pdf.

[61] Ferreira, H.A., Graham, D.L., Parracho, P., Soares, V., Freitas, P.P. (2004). Flow velocity measurement in microchannels using magnetoresistive chips. IEEE Transactions on Magnetics, 40 (4), 2652-2654.

Annexes

Annex I

Run Sheet for Magnetic Counter fabrication process

RUN:

Process Start : **Process Finish :**

SV#_____ = MR= ___ % Hf= ___ Oe

STEP 1	1st Exposure – Spin valve Definition	Date:

Substrate: Si substrate with 1000 Å of SiO2 and passivated SV

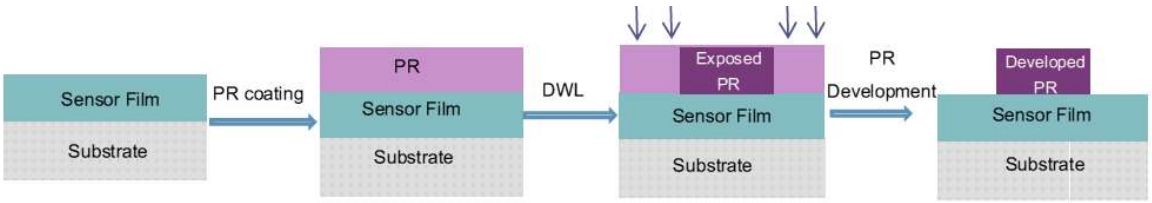

1) Coating PR: Vapor Prime 30 min (Recipe - 0) - Organic compound (Hexamethyldisilane, C6H18Si2)
This step promotes the PR coating adhesion.

Step description	Conditions
Wafer dehydration	Vacuum, 10 Torr, 2 min. N2 inlet, 760 Torr, 3 min. Heating to 130°C
Priming	Vacuum, 1 Torr, 3 min. HMDS, 6 Torr, 5 min.
Purge prime exhaust	Vacuum, 4 Torr, 1 min. N2 inlet, 500 Torr, 2 min. Vacuum, 4 Torr, 2 min.
Return to atmosphere	N2 inlet, 3 min.

2) Coat 1.5 µm PR (Recipe 6/2) - Positive photoresist (PFR7790G27cP - JSR Electronics)

Coating Parameters	
First Step	Dispense photoresist on the sample and spinning at 800 rpm for 5 sec.
Second step	Spin at 2500 rpm for 30 s to obtain ~1.45µm thickness.
Third step	Soft bake at 85°C for 60 seconds.

3) Machine: DWL 2.0

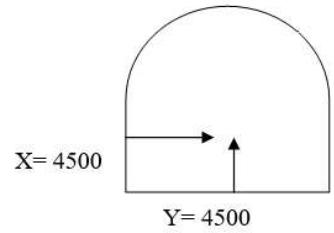

Mask: inesc_citometro_2.0.dwg Map:

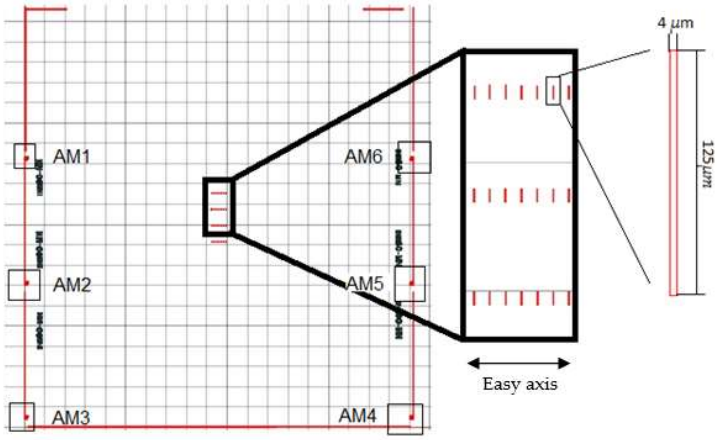

Alignment mark position:

AM1	X= 162.06 Y= 16483.42
AM2	X= 169.06 Y= 8833.48
AM3	X= 162.06 Y= 570.42
AM4	X= 23938.06 Y= 570.42
AM5	X= 23950.06 Y= 8833.48
AM6	X= 23946.06 Y= 16483.42

Energy: 55

Power: 100 mW

Focus: -20

Alignment mark points

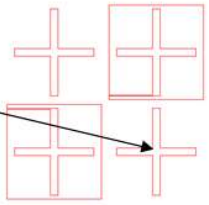

4) Develop : Recipe 6/2

Developer: TMA238WA

Development parameters:
Bake at 110°C for 60s
Cool for 30s
Developer for 60s

5) Inspection:

STEP	Comments
1	
2	
3	
4	

STEP 2	**Ion Milling** – Spin valve etching	Date:

Machine: Nordiko 3600 Ion beam deposition and milling system

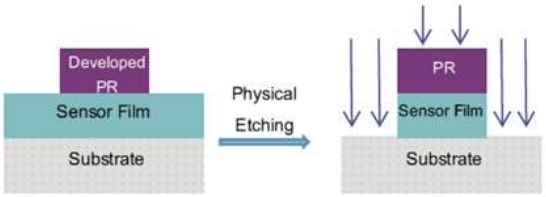

Total thickness to etch: 345 Å
Etch rate: ~ 1 Å/s **Required time:** 400 s

Standard Etching Recipe (junction_etch) : Junction_etch

Assist Gun	Power (W)	V+ (V)	I+ (mA)	V- (V)	I- (mA)	Ar Flux (sccm)	Pan (deg)	Rotation (rpm)
Set Values	150	735	105	-350	-	10	60	30
Read Values								

Inspection:

Comments

STEP 3	**Resist strip**	Date:

Equipment: Wet bench

1) **Microstrip® at 65ºC + ultrasounds**

Started:
Stoped:
Total Time in hot µ-strip :
Ultrasonic Time :

2) **Rinse with IPA + DI water + dry**

Inspection:

Comments

STEP 4	**2nd Exposure** – Contact	Date:

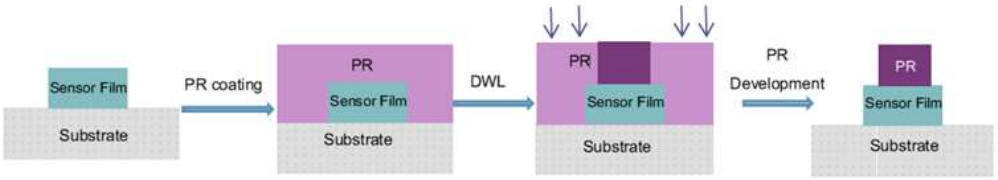

1) Coating PR: Vapor Prime 30 min (Recipe - 0)

Step description	Conditions
Wafer dehydration	Vacuum, 10 Torr, 2 min. N2 inlet, 760 Torr, 3 min. Heating to 130°C
Priming	Vacuum, 1 Torr, 3 min. HMDS, 6 Torr, 5 min.
Purge prime exhaust	Vacuum, 4 Torr, 1 min. N2 inlet, 500 Torr, 2 min. Vacuum, 4 Torr, 2 min.
Return to atmosphere	N2 inlet, 3 min.

2) Coat 1.5 μm PR (Recipe 6/2)

Coating Parameters	
First Step	Dispense photoresist on the sample and spinning at 800 rpm for 5 sec.
Second step	Spin at 2500 rpm for 30 sec. to obtain ~1.45μm thickness.
Third step	Soft bake at 85°C for 60 seconds.

3) Pre-development Developer: TMA238WA

Pre-development parameters:
No bake
Developer for 20s

4) Machine: DWL 2.0

Mask: inesc_citometro_2.0.dwg Map:

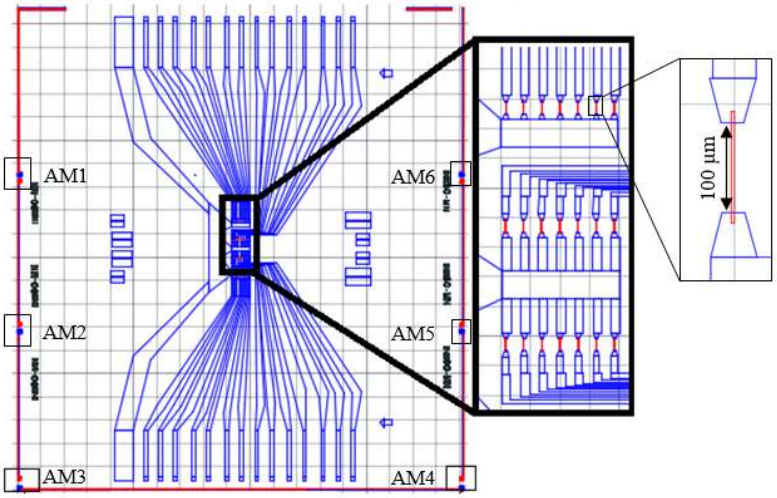

Alignment mark position:

AM1	X= 162.06 Y= 16483.420
AM2	X= 169.06 Y= 8833.48
AM3	X= 162.06 Y= 570.42
AM4	X= 23938.06 Y= 570.42
AM5	X= 23950.06 Y= 8833.48
AM6	X= 23946.06 Y= 16483.42

Energy: 55 + 20 %

Power: 100 mW

Focus: -20

Alignment mark points

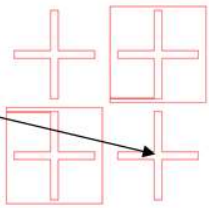

5) Develop : Recipe 6/2 Developer: TMA238WA

Development parameters:
Bake at 110°C for 60s
Cool for 30s
Developer for 60s

6) Inspection:

STEP	Comments
1	
2	
3	
4	
5	

STEP 5	**Contacts deposition**	Date:

Machine: Nordiko 7000
Expected thickness: 3000 Å (Al) + 150 Å (TiWN2)

Module 2– f.9 (1′ soft sputter etch)					
	Power1 (W)	Power2 (W)	Gas flux (sccm) Ar	Pressure (mTorr)	
Set Values	60	40	50	3	
Read Values					

Module 4 – f.1 (3000 Å Al, 1′20″)					
	Power (kW)	Voltage	Current	Gas flux (sccm) Ar	Pressure (mTorr)
Set Values	2			50	3
Read Values					

	Module 3 – f.19 (150 Å TiWN2, 27″)					
	Power (kW)	Voltage	Current	Gas flux (sccm) Ar	Gas flux (sccm) N_2	Pressure (mTorr)
Set Values	0.5			50	10	3
Read Values						

Inspection:

Comments

STEP 6	**Aluminum Lift-Off**	Date:

Equipment: Wet bench

1) **Microstrip® at 65ºC + ultrasounds**

Started:
Stoped:
Total Time in hot µ-strip :
Ultrasonic Time :

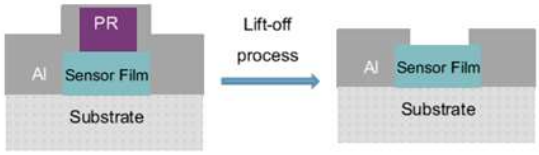

2) **Rinse with IPA + DI water + dry**

3) **Inspection:**

Comments

STEP 7	**Passivation layer - 3000Å Si_3N_4**	Date:

Machine: Electrotech Delta Chemical Vapor Deposition System
Expected thickness: 3000 Å
Time: 1min 14 sec
Holder: 300ºC
Showerhead: 350ºC

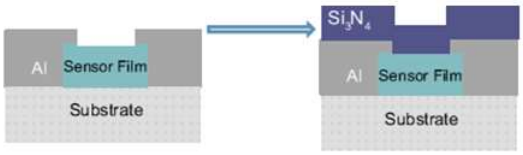

	Deposition Time	**SiN thickness (A)**	**NH_3 gas flux (sccm)**	**SiH_4 gas flux (sccm)**	**N_2 gas flux (sccm)**	**Pressure (mT)**	**Power Source RF (W)**
Set Values	1min 14 sec	3000	500	300	3500	850	500
Read Values							

Inspection:

Comments

STEP 8	**3rd Exposure** – passivation layer	Date:

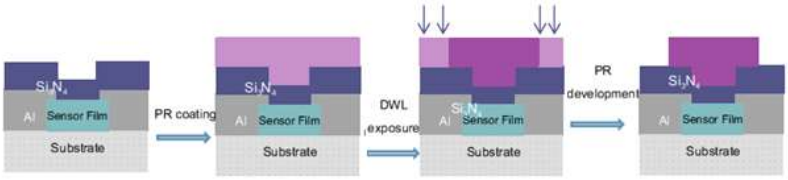

1) Coating PR: Vapor Prime 30 min (Recipe - 0)

Step description	Conditions
Wafer dehydration	Vacuum, 10 Torr, 2 min. N2 inlet, 760 Torr, 3 min. Heating to 130°C
Priming	Vacuum, 1 Torr, 3 min. HMDS, 6 Torr, 5 min.
Purge prime exhaust	Vacuum, 4 Torr, 1 min. N2 inlet, 500 Torr, 2 min. Vacuum, 4 Torr, 2 min.
Return to atmosphere	N2 inlet, 3 min.

2) Coat 1.5 μm PR (Recipe 6/2)

Coating Parameters	
First Step	Dispense photoresist on the sample and spinning at 800 rpm for 5 sec.
Second step	Spin at 2500 rpm for 30 sec. to obtain ~1.45μm thickness.
Third step	Soft bake at 85°C for 60 seconds.

3) Machine: DWL 2.0

Mask: inesc_citometro_2.0.dwg Map:

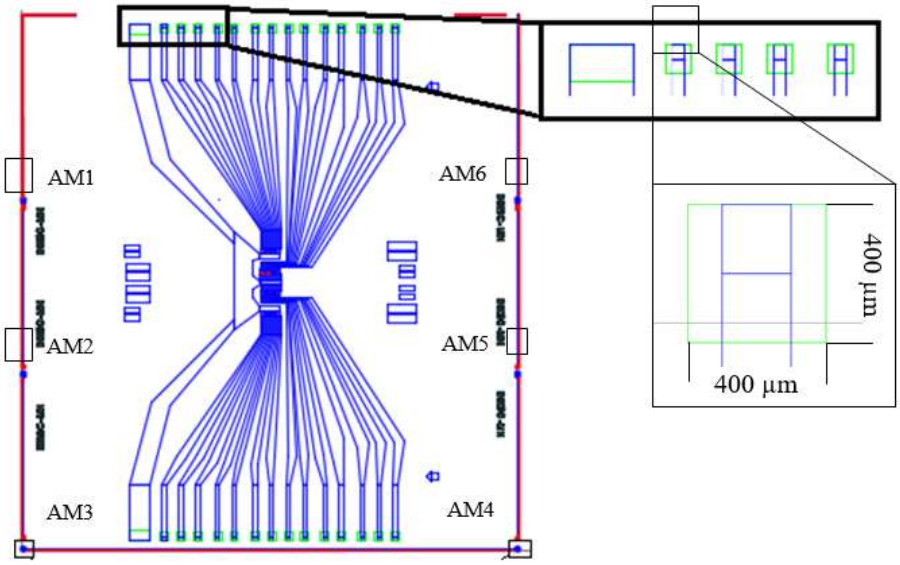

Alignment mark position:

AM1	X= 162	
	Y= 16831	
AM2	X= 165	
	Y= 8443	
AM3	X= 162	
	Y= 54	
AM4	X= 23946	
	Y= 54	
AM5	X= 23946	
	Y= 8443	
AM6	X= 23946	
	Y= 16831	

Alignment mark points

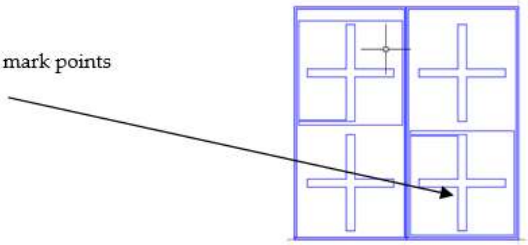

4) Develop : Recipe 6/2 Developer: TMA238WA

Development parameters:
Bake at 110°C for 60s
Cool for 30s
Developer for 60s

Inspection:

Comments
Confirm that photoresist is everywhere except over the vias

STEP 9	**Reactive ion etching** – pads openning	Date:

Equipment: LAM Rainbow 4400
Process recipe: 6
Expected thickness: 3000 Å
Thickness to etch: 3000 Å
Etch rate: ~ Å/s
Second step: Time – 5 x 230s

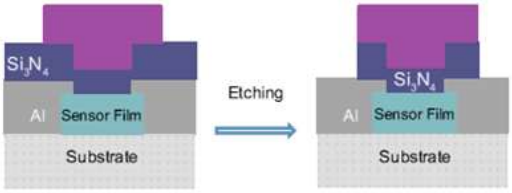

Etching conditions:

	Pressure (Torr)	Etch time (s)	Power (RF)	Ar Flux (sccm)	CF_4 Flux (sccm)	O_2 (sccm)
Expected	140 mTorr	-300 s *-over-etch*: 300s	100 W	200	100	0
Observed		- -cooling: *-over-etch*:	s s s			

Inspection:

Comments
Measure resitance before resist cleaning

Next step: annealing
A) if sample needs annealing -> maintain resist –> dice –> clean –>
B) if sample needs no annealing -> resist strip –> dice –> clean

STEP 10	**Dicing**	Date:

Machine: **DISCO DAD 321**

Die size: X = 23994 + 0 (separation) ; Y = 25856 + 0 (separation)

STEP 11	**Resist strip**	Date:

Equipment: Wet bench

1) **Microstrip® at 65°C + ultrasounds**

Started:
Stoped:
Total Time in hot µ-strip :
Ultrasonic Time :

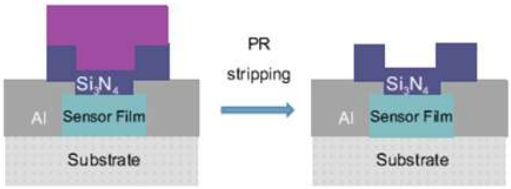

2) **Rinse with IPA + DI water + dry**

3) **Inspection:**

Comments

STEP 12	**Annealing**	Date:

Equipment: 21100 Tube Furnace (BL Barnstead Thermolyne) and a 1T magnet.

Annealing conditions:

1) Heating the sample till 250°C then leave it 15min@ 250 °C.

2) Annealing for 1h @ 250°C, under a magnetic field of 1 kOe.

Annex II

Run Sheet: Glass Hard Mask

Responsable:

Sample ID:

Process start: Process end:

Step 1: Substrate cleaning and preparation

Date:	Operator:	Pre-treatment: No

Substrate: Glass sample of mm thickness (1x1 in)

Conditions: - Washing with Alconox for 30 min in ultrasounds, followed by rinsing with deionised water (particle and grease removal);
- Drying with compressed air.

Observations:.

Step 2: Al deposition

Date:	Operator:	Pre-treatment: No

Substrato: Glass sample of mm thickness

Equipment: Nordiko 7000

Expected thickness: 1500 Å **Deposited thickness:**

Deposition conditions:

	Mode	Power (W)	Ar Flux(sccm)	Pressure (mTorr)
Expected	Mod4 F1 *metalization* 40''	2000	50	3
Observed				

Observações:

Step 3: Exposure

Date:	Operator:	Pre-treatment: No

Substrate: Glass sample with Al layer

Equipment: DWL 2.0

Step 3.1: *Vapour prime* (30min, *Vapour Prime Oven*) – heating at 130 °C in vacuum with HDMS spraying (5min).

Step 3.2: *Coating* (SVG) of 1.5µm of positive photoresist (PFR7790G27cP - JSR Electronics)– rotation of PR at 2800 rpm, followed by soft-bake at 85 °C for 1 min.

Step 3.3: Exposure (DWL 2.0)

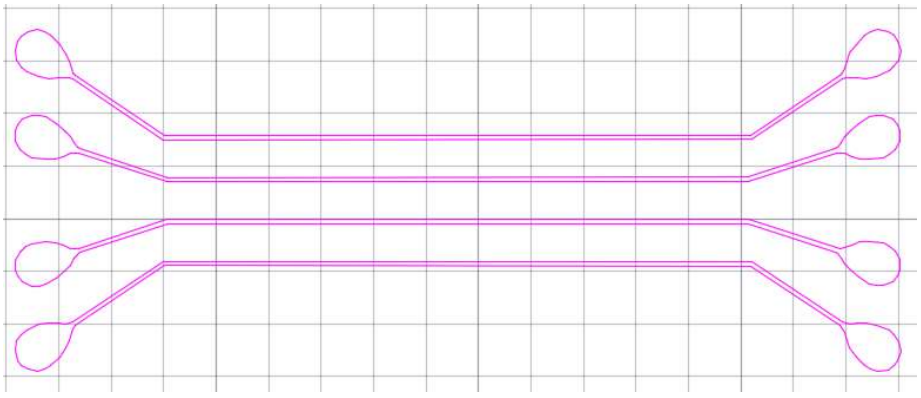

Exposure conditions:

Map	Mask	E	F	Time	$X_0;Y_0$ (nm)	Die dimensions (µm)
					0,0 (não tem cruz de alinhamento)	

Step 3.4: Development (SVG) – baking at 110 °C for 1min, followed by development during 1min.

Masks:

Step 3.5: Microscope verification of SV exposure.

Observations:

Step 4: *Wet etch*

Date:	Operator:	Pre-treatment: No

Substrate: Glass sample with Al layer and PR

Equipment: *Wet bench*

Step 4.1: *Etch*

Solvent	T (°C)	Time	Notes
Acetic acid 3,3%, Nitric acid 3,1%, Phosphoric acid 3% puro		min per sample	

Step 4.2: Substrate washing with deionised water.

Observations: Etch rate ~6Å/s

Step 5: *Resist stripping*

Date:	Operator:	Pre-treatment: No

Substrate: Glass sample with Al layer and PR

Equipment: *Wet bench*

Step 5.1: *Stripping*

Solvent	T (°C)	Time	Notes
Microstrip 3001	65		

Step 5.2: Substrate washing with IPA, followed by rinsing in deionised water and blow-dryed with compressed air gun.

Observations:

Annex III

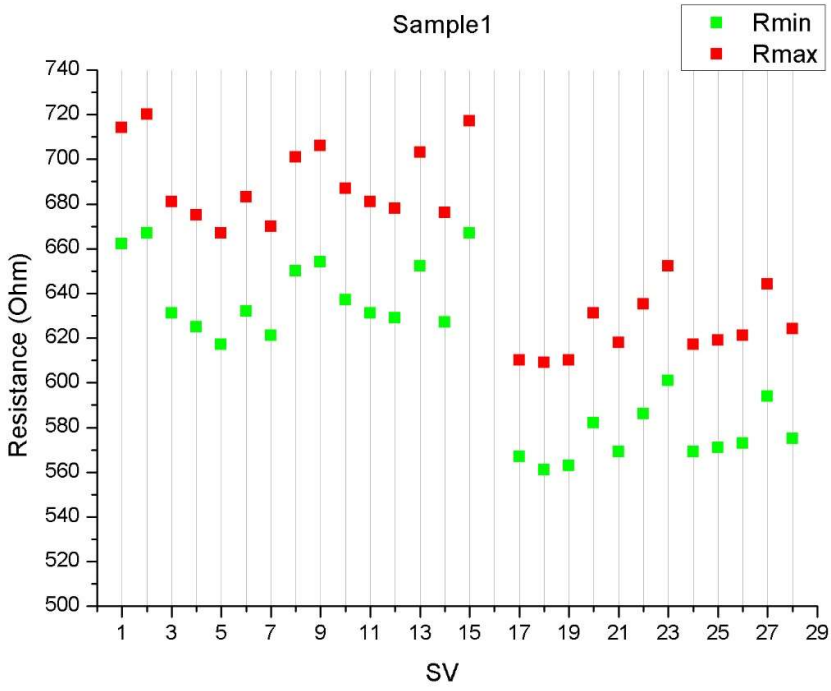
Sample1
Rmin
Rmax
Resistance (Ohm)
740
720
700
680
660
640
620
600
580
560
540
520
500
1
3
5
7
9
11
13
15
17
19
21
23
25
27
29
SV

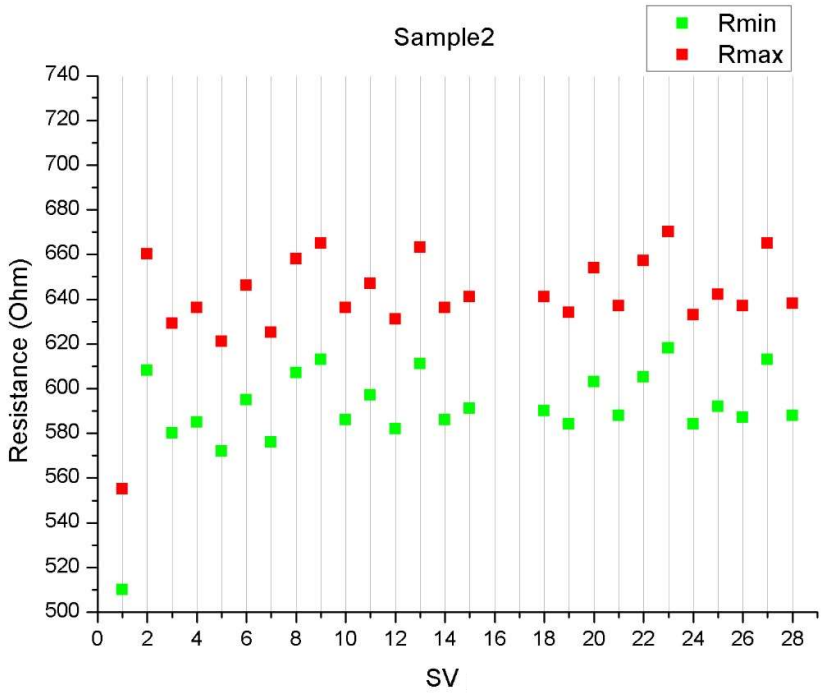
Sample2
Rmin
Rmax
Resistance (Ohm)
740
720
700
680
660
640
620
600
580
560
540
520
500
0
2
4
6
8
10
12
14
16
18
20
22
24
26
28
SV

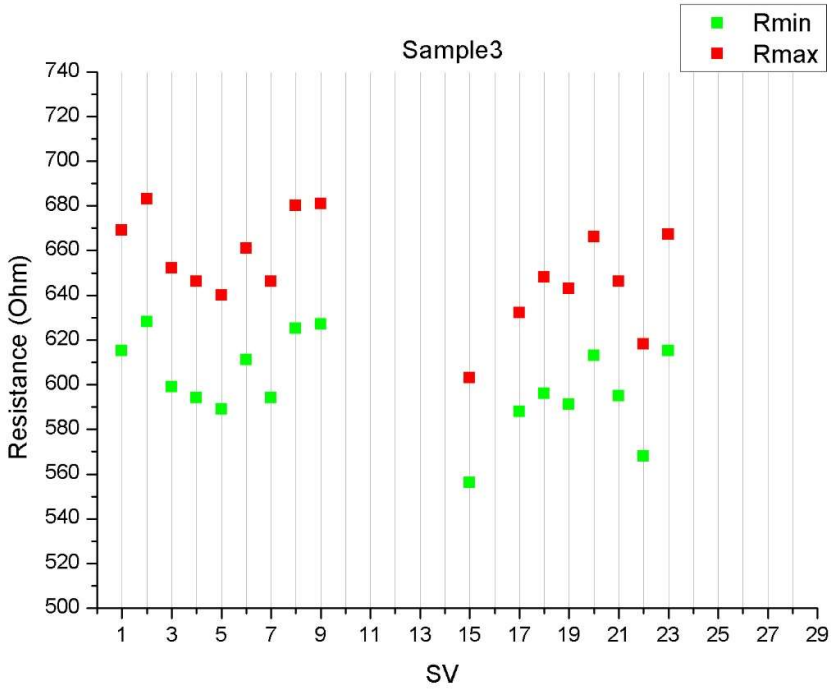
Sample3
Rmin
Rmax
Resistance (Ohm)
740
720
700
680
660
640
620
600
580
560
540
520
500
1
3
5
7
9
11
13
15
17
19
21
23
25
27
29
SV

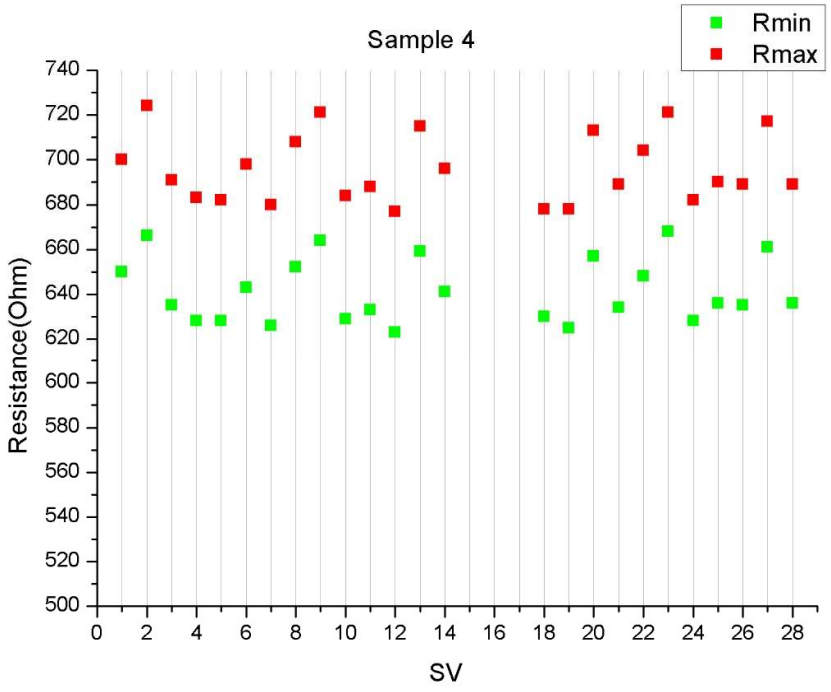
Sample 4
Rmin
Rmax
Resistance(Ohm)
740
720
700
680
660
640
620
600
580
560
540
520
500
0
2
4
6
8
10
12
14
16
18
20
22
24
26
28
SV